ISSN 1997-308X
eISSN 2412-8767

ИЗВЕСТИЯ ВУЗОВ
ПОРОШКОВАЯ МЕТАЛЛУРГИЯ И ФУНКЦИОНАЛЬНЫЕ ПОКРЫТИЯ

POWDER METALLURGY AND FUNCTIONAL COATINGS

2023
Том / Vol. 17 № / No. 4
powder.misis.ru

ISSN 1997-308X
eISSN 2412-8767

POWDER METALLURGY AND FUNCTIONAL COATINGS

Scientific and Technical Journal
Founded in 2007
Four issues per year

2023
Vol. 17 No. 4
Том 17 № 4

ИЗВЕСТИЯ ВУЗОВ
ПОРОШКОВАЯ МЕТАЛЛУРГИЯ И ФУНКЦИОНАЛЬНЫЕ ПОКРЫТИЯ

Научно-технический журнал
Основан в 2007 г.
Выходит 4 раза в год

POWDER METALLURGY AND FUNCTIONAL COATINGS

ISSN 1997-308X
eISSN 2412-8767

SCIENTIFIC AND TECHNICAL JOURNAL
FOUNDED IN 2007
FOUR ISSUES PER YEAR

http://powder.misis.ru

Founder: MISIS UNIVERSITY OF SCIENCE AND TECHNOLOGY

National University of Science
and Technology "MISIS"
Address: 4 bld. 1 Leninskiy Prosp., Moscow 119049, Russian Federation
http://www.misis.ru

Editor-in-Chief

Evgeny A. Levashov
Prof., Dr. Sci. (Eng.), Acad. of the RANS, NUST MISIS, Moscow, Russian Federation

Journal is included into the List of peer-reviewed scientific publications recommended by the Highest Attestation Commission of the Ministry of Education and Science of the Russian Federation for publishing the results of doctoral and candidate dissertations.
Abstracting/Indexing: Scopus, Russian Science Citation Index (RSCI), Ulrich's Periodicals Directory, VINITI Database (Abstract Journal).

Editorial Board

M. I. Alymov – Dr. Sci. (Eng.), Corresponding Member of the RAS, Merzhanov Institute of Structural Macrokinetics and Materials Sciences of the RAS, Chernogolovka, Russia
A. P. Amosov – Prof., Dr. Sci. (Phys.-Math.), Samara State Technical University, Samara, Russia
G. A. Bagliuk – Prof., Dr. Sci. (Eng.), Acad. of the NASU, IPMS NASU, Kiev, Ukraine
I. V. Blinkov – Prof., Dr. Sci. (Eng.), NUST MISIS, Moscow, Russia
M. V. Chukin – Prof., Dr. Sci. (Eng.), Magnitogorsk State Technical University, Magnitogorsk, Russia
H. Danninger – Prof., Dr. Sci., Vienna University of Technology, Vienna, Austria
B. Derin – Assoc. Prof., Dr. Sci. (Phil.), Istanbul Technical University, Maslak, Istanbul, Turkey
V. Yu. Dorofeyev – Prof., Dr. Sci. (Eng.), South-Russian State Polytechnical University (NPI), Novocherkassk, Russia
Yu. Estrin – Prof., Dr. Sci. (Nat.), Monash University, Clayton, Australia
A. Ph. Ilyushchanka – Prof., Dr. Sci. (Eng.), Acad. of the NAS of Belarus, State Research and Production Powder Metallurgy Association, Minsk, Belarus
Yu. R. Kolobov – Prof., Dr. Sci. (Phys.-Math.), Federal Research Center of Problems of Chemical Pfysics and Medicinal Chemistry of the RAS, Chernogolovka, Russia
V. S. Komlev – Prof., Dr. Sci. (Eng.), Corresponding Member of the RAS, Institute of Metallurgy of the RAS, Moscow, Russia
I. Konyashin – Prof., Dr. Sci. (Econ.), Element Six GmbH, Burghaun, Germany
Yu. M. Korolyov – Prof., Dr. Sci. (Eng.), Scientific and Technical Association "Powder Metallurgy", Moscow, Russia
D. Yu. Kovalev – Dr. Sci. (Phys.-Math.), Merzhanov Institute of Structural Macrokinetics and Materials Sciences of the RAS, Chernogolovka, Russia
S. A. Kulinich – Assoc. Prof., PhD (Chem.), Tokai University, Hiratsuka, Kanagawa, Japan
S. V. Kuzmin – Prof., Dr. Sci. (Eng.), Corresponding Member of the RAS, Volgograd State Technical University, Volgograd, Russia
V. P. Kuznetsov – Prof., Dr. Sci. (Eng.), Ural Federal University, Ekaterinburg, Russia
Yu. V. Levinsky – Prof., Dr. Sci. (Eng.) Merzhanov Institute of Structural Macrokinetics and Materials Sciences of the RAS, Chernogolovka, Russia
A. E. Ligachyov – Prof., Dr. Sci. (Phys.-Math.), Prokhorov General Physics Institute of the RAS, Moscow, Russia
V. Yu. Lopatin – Cand. Sci., NUST MISIS, Moscow, Russia
A. A. Lozovan – Prof., Dr. Sci (Eng.), Moscow Aviation Institute (NRU), Moscow, Russia
V. I. Lysak – Prof., Dr. Sci. (Eng.), Acad. of the RAS, Volgograd State Technical University, Volgograd, Russia
A. V. Makarov – Dr. Sci. (Eng.), Corresponding Member of the RAS, M.N. Mikheev Institute of Metal Physics of the Ural Branch of the RAS, Ural Federal University, Ekaterinburg, Russia
L. L. Mishnaevsky – Dr. Habil. (Eng.), Technical University of Denmark, Roskilde, Denmark
A. S. Mukasyan – Prof., Dr. Sci. (Phys.-Math.), University of Notre Dame, Notre Dame, USA
S. A. Oglezneva – Prof., Dr. Sci. (Eng.), Perm National Research Polytechnical University, Perm, Russia
R. Orrù – Prof., Dr. Sci. (Eng.), University of Cagliari, Cagliari, Italy
I. B. Panteleev – Prof., Dr. Sci. (Eng.), St. Petersburg State Technological Institute (Technical University), St. Petersburg, Russia
F. Peizhong – Prof., Dr. Sci., China University of Mining and Technology, Xuzhou, P.R. China
C. Pengwan – Prof., Dr. Sci., Beijing Institute of Technology, Beijing, P.R. China
M. I. Petrzhik – Dr. Sci. (Eng.), NUST MISIS, Moscow, Russia
Yu. S. Pogozhev – Assoc. Prof., Cand. Sci. (Eng.), NUST MISIS, Moscow, Russia
V. V. Polyakov – Prof., Dr. Sci. (Phys.-Math.), Altai State University, Barnaul, Russia
A. A. Popovich – Prof., Dr. Sci. (Eng.)., Corresp. Member of the RANS, St. Petersburg State Polytechnical University (National Research University), St. Petersburg, Russia
S. E. Porozova – Dr. Sci. (Eng.), Perm National Research Polytechnical University, Perm, Russia
A. A. Rempel – Prof., Dr. Sci. (Phys.-Math.), Acad. of the RAS, Institute of Metallurgy of the Ural Branch of the RAS, Ekaterinburg, Russia
F. Rustichelli – Prof., Dr. Sci. (Phys.), University of Marches, Ancona, Italy
S. D. Shlyapin – Prof., Dr. Sci. (Eng.), Moscow Aviation Institute (NRU), Moscow, Russia
D. V. Shtansky – Prof., Dr. Sci. (Phys.-Math.), NUST MISIS, Moscow, Russia
A. N. Timofeev – Dr. Sci. (Eng.), JSC "Komposite", Korolev, Russia
P. A. Vityaz' – Prof., Dr. Sci. (Eng.), Acad. of the NAS of Belarus, Minsk, Belarus
A. A. Zaitsev – Assoc. Prof., Cand. Sci. (Eng.), NUST MISIS, Moscow, Russia
Zh. YongTing – Prof., Dr. Sci., Harbin Institute of Technology, Harbin, P.R. China
F. Zhengyi – Prof., Dr. Sci., Wuhan University of Technology, Wuhan, P.R. China

Editorial Staff

Address: NUST MISIS,
4 bld. 1 Leninskiy Prosp., Moscow 119049, Russian Federation

Phone: +7 (495) 638-45-35. ***E-mail:*** izv.vuz@misis.ru

Certificate of registration **No. FS77-27955** (12.04.2007)
Re-registration **PI No. FS77-79230** (25.09.2020)

Leading Editor: A.A. Kudinova
Executive Editor: O.V. Sosnina
Layout Designer: V.V. Rasenets

Signed print 20.12.2023. Format 60×90 $^{1}/_{8}$
Offset paper No. 1. Digital printing. Quires 9.25
Order 18901. Free price
Printed in the printing house of the MISIS Publish House
4 bld. 1 Leninskiy Prosp., Moscow, 119049 Russian Federation
Phone/fax: +7 (499) 236-76-17

PM & FC © NUST MISIS, Moscow, 2023

Articles are available under Creative Commons Attribution Non-Commercial No Derivatives

ИЗВЕСТИЯ ВУЗОВ ПОРОШКОВАЯ МЕТАЛЛУРГИЯ И ФУНКЦИОНАЛЬНЫЕ ПОКРЫТИЯ

НАУЧНО-ТЕХНИЧЕСКИЙ ЖУРНАЛ
ОСНОВАН В 2007 Г.
ВЫХОДИТ 4 РАЗА В ГОД

http://powder.misis.ru

ISSN 1997-308X
eISSN 2412-8767

Учредитель: МИСИС УНИВЕРСИТЕТ НАУКИ И ТЕХНОЛОГИЙ

ФГАОУ ВО Национальный исследовательский технологический университет «МИСИС»
Адрес: 119049, Москва, Ленинский пр-т, 4, стр. 1
https://www.misis.ru

Главный редактор

Евгений Александрович Левашов
д.т.н., академик РАЕН, профессор, НИТУ МИСИС, г. Москва

Журнал включен в Перечень рецензируемых научных изданий, рекомендованных ВАК Минобрнауки РФ для публикации результатов диссертаций на соискание ученых степеней.
Журнал включен в базы данных: Scopus, Russian Science Citation Index (RSCI), Ulrich's Periodicals Directory, РИНЦ, БД/РЖ ВИНИТИ.

Редакционная коллегия

М. И. Алымов – д.т.н., чл.-корр. РАН, проф., ИСМАН, г. Черноголовка
А. П. Амосов – д.ф.-м.н., проф., СамГТУ, г. Самара
Г. А. Баглюк – д.т.н., акад. НАНУ, проф., ИПМ НАН Украины, г. Киев
И. В. Блинков – д.т.н., проф., НИТУ МИСИС, г. Москва
П. А. Витязь – д.т.н., акад. НАНБ, проф., НАН Беларуси, г. Минск
В. Ю. Дорофеев – д.т.н., проф., ЮРГПУ (НПИ), г. Новочеркасск
А. А. Зайцев – к.т.н., доц., НИТУ МИСИС, г. Москва
А. Ф. Ильющенко – д.т.н., акад. НАН Беларуси, проф., ГНПО ПМ НАН Беларуси, г. Минск
Д. Ю. Ковалев – д.ф.-м.н., ИСМАН, г. Черноголовка
Ю. Р. Колобов – д.ф.-м.н., проф., ФИЦ ПХФ и МХ РАН, г. Черноголовка
В. С. Комлев – д.т.н., чл.-корр. РАН, проф., ИМЕТ РАН, г. Москва
Ю. М. Королев – д.т.н., проф., НТА «Порошковая металлургия», г. Москва
В. П. Кузнецов – д.т.н., проф., УрФУ, г. Екатеринбург
С. В. Кузьмин – д.т.н., чл.-корр. РАН, проф., ВолгГТУ, г. Волгоград
Ю. В. Левинский – д.т.н., проф., ИСМАН, г. Черноголовка
А. Е. Лигачев – д.ф.-м.н., проф., ИОФ РАН, г. Москва
А. А. Лозован – д.т.н., проф., МАИ (НИУ), г. Москва
В. Ю. Лопатин – к.т.н., доц., НИТУ МИСИС, г. Москва
В. И. Лысак – д.т.н., акад. РАН, проф., ВолгГТУ, г. Волгоград
А. В. Макаров – д.т.н., чл.-корр. РАН, ИФМ УрО РАН, УрФУ, г. Екатеринбург
С. А. Оглезнева – д.т.н., проф., ПНИПУ, г. Пермь
И. Б. Пантелеев – д.т.н., проф., СПбГТИ (ТУ), г. Санкт-Петербург
М. И. Петржик – д.т.н., проф., НИТУ МИСИС, г. Москва
Ю. С. Погожев – к.т.н., доц., НИТУ МИСИС, г. Москва
В. В. Поляков – д.ф.-м.н., проф., АлтГУ, г. Барнаул
А. А. Попович – д.т.н., чл.-корр. РАЕН, проф., СПбГПУ, г. Санкт-Петербург
С. Е. Порозова – д.т.н., проф., ПНИПУ, г. Пермь
А. А. Ремпель – д.ф.-м.н., акад. РАН, проф., ИМЕТ УрО РАН, г. Екатеринбург
А. Н. Тимофеев – д.т.н., АО «Композит», г. Королев
М. В. Чукин – д.т.н., проф., МГТУ, г. Магнитогорск
С. Д. Шляпин – д.т.н., проф., МАИ (НИУ), г. Москва
Д. В. Штанский – д.ф.-м.н., проф., НИТУ МИСИС, г. Москва
C. Pengwan – Dr. Sci., Prof., Beijing Institute of Technology, Beijing, P.R. China
H. Danninger – Dr. Sci., Prof., Vienna University of Technology, Vienna, Austria
B. Derin – Dr. Sci. (Phil.), Assoc. Prof., Istanbul Technical University, Maslak, Istanbul, Turkey
Yu. Estrin – Dr. Sci. (Nat.), Prof., Monash University, Clayton, Australia
F. Peizhong – Dr. Sci., Prof., China University of Mining and Technology, Xuzhou, P.R. China
F. Zhengyi – Dr. Sci., Prof., Wuhan University of Technology, Wuhan, P.R. China
I. Konyashin – Dr. Sci. (Econ.), Prof., Element Six GmbH, Burghaun, Germany
S. A. Kulinich – PhD (Chem.), Associate Prof., Tokai University, Hiratsuka, Kanagawa, Japan
L. L. Mishnaevsky – Dr. Habil. (Eng.), Technical University of Denmark, Roskilde, Denmark
A. S. Mukasyan – Dr. Sci. (Phys.-Math.), Prof., University of Notre Dame, Notre Dame, USA
R. Orrù – Dr. Sci. (Eng.), Prof., University of Cagliari, Cagliari, Italy
F. Rustichelli – Dr. Sci. (Phys.), Prof., University of Marches, Ancona, Italy
Zh. YongTing – Dr. Sci., Prof., Harbin Institute of Technology, Harbin, P.R. China

Редакция журнала

Адрес: 119049, Москва,
Ленинский пр-т, 4, стр. 1. НИТУ МИСИС

Тел.: +7 (495) 638-45-35. *Эл. почта:* izv.vuz@misis.ru

Свидетельство о регистрации № **ФС77-27955** от 12.04.2007 г.
Перерегистрация 25.09.2020 г. **ПИ № ФС77-79230**

Ведущий редактор: А.А. Кудинова
Выпускающий редактор: О.В. Соснина
Дизайн и верстка: В.В. Расенець

Подписано в печать 20.12.2023. Формат 60×90 $^1/_8$
Бум. офсетная № 1. Печать цифровая. Усл. печ. л. 9,25
Заказ 18901. Цена свободная
Отпечатано в типографии Издательского Дома МИСИС
119049, г. Москва, Ленинский пр-т, стр. 1
Тел./факс: +7 (499) 236-76-17

ПМ и ФП ИЗВЕСТИЯ ВУЗОВ © НИТУ МИСИС, Москва, 2023

Статьи доступны под лицензией Creative Commons Attribution Non-Commercial No Derivatives

Contents

Production Processes and Properties of Powders

Cherezov N.P., Alymov M.I.
Investigation of physical, chemical, and technological properties of titanium powder obtained by thermal dehydrogenation in vacuum 5

Syrnev B.V., Pestova G.S., Semilutskaya O.V., Tuganbaev F.S.
Characteristics of granule solidification in gas atomization of molten beryllium 16

Refractory, Ceramic and Composite Materials

Vasiliev A.N., Sergeenko S.N.
Multicriteria optimization of mechanical processing for Pb–C composite charge material 25

Cheblakova E.G., Kleusov B.S., Sapozhnikov V.I., Gorina V.A., Malinina Yu.A., Gareev A.R.
Investigation of the properties of high-strength fibers by methods of physico-chemical analysis 34

Zaitsev A.A., Loginov P.A., Levashov E.A.
In situ study of mechanical properties and structural transformations during heating of WC–TaC–Co cemented carbides in a transmission electron microscope column 41

Nanostructured Materials and Functional Coatings

Burkov A.A., Kulik M.A.
Electrospark deposition of Fe–Cr–Cu coatings on St3 steel 51

Zorin I.V., Lysak V.I., Kharlamov V.O., Fastov S.A.
Transformation of the nickel aluminide alloy structure through the application of a heat-resistant coating using oscillation electrode surfacing 59

Содержание

Процессы получения и свойства порошков

Черезов Н.П., Алымов М.И.
Исследование физических, химических и технологических свойств порошка титана, полученного термическим дегидрированием в вакууме 5

Сырнев Б.В., Пестова Г.С., Семилуцкая О.В., Туганбаев Ф.С.
Особенности процесса затвердевания гранул при газоструйном распылении расплава бериллия 16

Тугоплавкие, керамические и композиционные материалы

Васильев А.Н., Сергеенко С.Н.
Многокритериальная оптимизация механической обработки шихты композиционного материала Pb–C 25

Чеблакова Е.Г., Клеусов Б.С., Сапожников В.И., Горина В.А., Малинина Ю.А., Гареев А.Р.
Исследования свойств высокопрочных волокон методами физико-химического анализа 34

Зайцев А.А., Логинов П.А., Левашов Е.А.
In situ исследование механических свойств и структурных превращений при нагреве твердых сплавов WC–TaC–Co в колонне просвечивающего электронного микроскопа 41

Наноструктурированные материалы и функциональные покрытия

Бурков А.А., Кулик М.А.
Электроискровое осаждение покрытий Fe–Cr–Cu на сталь Ст3 51

Зорин И.В., Лысак В.И., Харламов В.О., Фастов С.А.
Трансформация структуры сплава на основе алюминида никеля в процессе наплавки колеблющимся электродом термостойкого покрытия 59

Production Processes and Properties of Powders
Процессы получения и свойства порошков

UDC 621.762.242

https://doi.org/10.17073/1997-308X-2023-4-5-15

Research article
Научная статья

Investigation of physical, chemical, and technological properties of titanium powder obtained by thermal dehydrogenation in vacuum

N. P. Cherezov, M. I. Alymov

Merzhanov Institute of Structural Macrokinetics and Materials Science of the Russian Academy of Sciences
8 Akademican Osip'yan Str., Chernogolovka, Moscow Region 142432, Russia

cherezovnikita@gmail.com

Abstract. In recent times, there has been significant interest in powder metallurgy, driven primarily by the active development of additive manufacturing. Consequently, a pressing task is the development of methods for producing initial metal powders that are cost-effective while meeting high consumer standards. This research is a continuation of studies on titanium powders obtained through SHS hydrogenation and thermal dehydrogenation. The titanium hydride powders, previously obtained using SHS technology, were sieved, resulting in fractions that matched the granulometric composition of titanium powders of PTK, PTS, PTM, and PTOM grades. Subsequently, the titanium hydride powder samples underwent dehydrogenation through vacuum annealing in an electric resistance furnace. Throughout the dehydrogenation process, the kinetics of hydrogen release from the titanium powder were examined as a function of particle size. The macro- and microstructure, chemical composition, and technological properties of the dehydrogenated powders were thoroughly analyzed. It was determined that the titanium powder maintained its original polygonal fragmented shape after dehydrogenation. The average particle size decreased by 5–20 %, and “satellites” were observed on larger particles. Chemical analysis revealed that larger samples contained a higher level of residual hydrogen and gas impurities (Σ0.77 wt. %) compared to finer powders (Σ0.26 wt. %). Regarding the study of technological properties, the resulting powders exhibited the necessary characteristics for use in titanium powder metallurgy, with the exception of low flowability due to the particle shape and microstructural heterogeneity). In conclusion, this research has demonstrated the potential of the SHS hydrogenation and thermal dehydrogenation method in producing high-quality titanium powders.

Keywords: titanium, powder metallurgy, self-propagating high-temperature synthesis (SHS), dehydrogenation, morphology, chemical properties, technological properties

Acknowledgements: This work was carried out under the state assignment received by the Merzhanov Institute of Structural Macrokinetics and Materials Science.

For citation: Cherezov N.P., Alymov M.I. Investigation of physical, chemical, and technological properties of titanium powder obtained by thermal dehydrogenation in vacuum. *Powder Metallurgy and Functional Coatings*. 2023;17(4):5–15. https://doi.org/10.17073/1997-308X-2023-4-5-15

Исследование физических, химических и технологических свойств порошка титана, полученного термическим дегидрированием в вакууме

Н. П. Черезов, М. И. Алымов

Институт структурной макрокинетики и проблем материаловедения им. А.Г. Мержанова РАН
Россия, 142432, Московская обл., г. Черноголовка, ул. Академика Осипьяна, 8

cherezovnikita@gmail.com

Аннотация. В последнее время наблюдается большой интерес к порошковой металлургии – в частности, благодаря активному развитию аддитивного производства, в связи с чем актуальной задачей является разработка методов получения исходных порошков металлов, которые обладали бы низкой стоимостью, но соответствовали высоким требованиям потребителя. Настоящая работа является продолжением исследований титановых порошков, получаемых методом СВС-гидрирования и термического дегидрирования. Полученные ранее порошки гидрида титана по технологии СВС были просеяны на фракции, соответствующие гранулометрическому составу порошка титана марок ПТК, ПТС, ПТМ и ПТОМ. Далее порошковые образцы гидрида титана были дегидрированы с помощью вакуумного отжига в электрической печи сопротивления. В процессе дегидрирования была исследована кинетика выделения водорода из порошка титана в зависимости от размера частиц. Изучены макро- и микроструктура, химические, технологические свойства дегидрированных порошков. Установлено, что порошок титана после дегидрирования сохранил исходную полигональную осколочную форму. Средний размер частиц уменьшился на 5–20 %, на крупных частицах были обнаружены «сателлиты». Химическим анализом выявлено, что крупные образцы содержат большее количество остаточного водорода и газовых примесей (Σ 0,77 мас. %), чем тонкие порошки (около Σ 0,26 мас. %). Согласно исследованиям технологических свойств, получаемые порошки обладают необходимыми характеристиками для применения в порошковой металлургии титана (исключением является низкая текучесть порошков из-за формы частиц и микронеоднородности структуры). Таким образом, показана перспективность метода СВС-гидрирования и термического дегидрирования, который позволяет изготавливать качественные порошки титана.

Ключевые слова: титан, порошковая металлургия, самораспространяющийся высокотемпературный синтез (СВС), дегидрирование, морфология, химические свойства, технологические свойства

Благодарности: Работа выполнена в рамках государственного задания Института структурной макрокинетики и проблем материаловедения им. А.Г. Мержанова РАН.

Для цитирования: Черезов Н.П., Алымов М.И. Исследование физических, химических и технологических свойств порошка титана, полученного термическим дегидрированием в вакууме. *Известия вузов. Порошковая металлургия и функциональные покрытия*. 2023;17(4):5–15. https://doi.org/10.17073/1997-308X-2023-4-5-15

Introduction

Titanium exhibits remarkably high chemical reactivity, in particular, it is highly reactive with nitrogen, carbon, and, most notably, oxygen, leading to the formation of a robust outer oxide layer [1]. This reactivity intensifies at elevated temperatures, leading to interactions with foundry equipment and the formation of a brittle surface layer on titanium, which can detrimentally affect its mechanical properties [2; 3]. Consequently, the production of titanium in conventional metallurgical furnaces becomes challenging, necessitating the creation of an inert gas or vacuum environment.

Powder metallurgy methods for crafting titanium products offer several advantages over traditional casting techniques:

– products and materials can attain unique physical, chemical, mechanical, and technological properties that are unattainable through conventional methods, such as pseudo-alloys, items with specific porosities, enhanced wear resistance, and friction materials;

– the possibility of using waste materials from metallurgical and engineering production, including scale and shavings;

– reduced consumption of costly metals due to the high material utilization ratio;

– less labor-intensive processes compared to casting and machining [4].

Titanium powder metallurgy involves stages like powder production, pressing, shaping, sintering, and finishing. The high cost associated with producing titanium powders often serves as the primary barrier hindering the utilization of powder metallurgy techniques for creating materials and products from titanium [5].

One potential approach to obtaining cost-effective titanium powders involves the crushing of titanium sponge [6; 7]. The resultant powder typically exhibits lower purity (96–97 wt. % Ti) and larger particle sizes (>630 μm). Challenges in the mechanical grinding process, using crushing methods, stem from the high ductility of pure titanium.

Electrolytic production of titanium is carried out at temperatures considerably below the titanium's melting point, resulting in a cathode deposit comprised of crystalline dendritic intergrowths. These intergrowths disintegrate into individual particles during the cleaning process after removal from the electrolyte. This method of obtaining titanium from its dioxide eliminates several complex steps found in alternative methods, such as the production of titanium chlorides and the generation of a reducing agent. Consequently, the development of this method was of great interest. However, in all cases of electrolysis using an insoluble anode, the resulting titanium powder contains a notable amount of impurities, which is why these technologies have not gained widespread industrial adoption [8].

Titanium powders can also be produced by hydrogenating sponge or waste titanium to form titanium hydride, which possesses inherent brittleness. This titanium hydride can be easily mechanically crushed and sieved to yield fine powders, subsequently subjected to dehydrogenation (removing hydrogen in a vacuum) in a furnace to produce pure titanium powder [9; 10]. These powders exhibit an irregular and fragmented morphology, and their impurity content can be quite low provided that the impurity content of the initial feedstock is minimal. The key advantage of this method is its relatively low cost. The expenses associated with hydrogenation and dehydrogenation only marginally increase the cost of the starting material, and the resulting powder exhibits high purity when the impurity content of the raw material is controlled. The oxygen content is significantly influenced by the starting material, processing procedures, and the specific surface area of the powder [5].

High-purity titanium powders are typically manufactured using atomization methods, which involve melting the titanium material and atomizing the molten metal in an inert atmosphere through various techniques [11–14]. The atomization process yields spherical titanium powders, ideally suited for additive manufacturing. However, the disadvantages of these powders include a broad particle size distribution, ranging from a few micrometers to hundreds of micrometers, as well as their notably higher cost when compared to powders produced by other methods.

A thermochemical process used extensively in Russia for producing titanium powder involves the direct reduction of titanium oxide with calcium hydride. As the temperature gradually increases, calcium hydride dissociates into hydrogen gas and calcium. The liberated calcium subsequently reacts with titanium dioxide to form titanium metal and calcium oxide. Hydrogen gas released during the dissociation of calcium hydride partially interacts with the reduced titanium, leading to the formation of titanium hydride [14–16]. The resulting titanium powder, obtained through the reduction of titanium dioxide with calcium hydride, boasts a well-developed porous structure, low impurity content, and fine particle size.

The development of new production methods for titanium powder, such as the Armstrong, CSIRO, and MER processes, aims to reduce the cost of titanium powder. However, as of now, these methods have not found commercial applications [17].

Among the considered methods, hydrogenation-dehydrogenation technology is regarded as the most promising, as it allows for the production of low-impurity and cost-effective titanium powder [18; 19]. This technology is environmentally friendly and generates minimal waste. Moreover, it can utilize titanium waste materials like chips, sawdust, and small scraps as feedstock, making it resource-efficient [20; 21].

The efficiency of the hydrogenation-dehydrogenation technology can be further enhanced by employing the self-propagating high-temperature synthesis (SHS) method. SHS is unique in that the hydrogenation process occurs without the need for external energy input, relying solely on the heat generated by the exothermic reaction $\mathrm{Ti} + \mathrm{H}_2 \rightarrow \mathrm{TiH}_2 + Q$ (39 kcal/mol) [22]. Subsequently, the synthesized titanium hydride undergoes the same processes as in the standard technology: grinding, sieving, and dehydrogenation.

The technological characteristics, such as bulk density and compressibility, of the initial powders are crucial for items produced through titanium powder metallurgy methods. These powders must possess specific properties and characteristics. The study of powder particle properties and structure for manufacturing products via solid-phase sintering is a pressing task in the development of titanium powder metallurgy technologies. It is essential for the quality parameters of powders to remain stable and consistent during storage [23–25].

The aim of this study was to conduct a thorough examination of titanium powders produced through the thermal dehydrogenation of titanium hydride in a vacuum. The research focused on investigating the impact of the powder's particle size distribution on dehydrogenation parameters, structural characteristics, chemical properties, and technological indicators. The particle size distribution of the powders selected for this study was chosen with consideration for potential practical applications and aligned with the specifications of the PTK, PTS, PTM, and PTOM grades.

Experimental

Titanium hydride powders with varying particle size distributions were employed as initial materials. Each hydride sample matched the particle size distribution specifications of titanium powders corresponding to the PTK, PTS, PTM, and PTOM grades. All the titanium hydride powders were produced using the SHS hydrogenation technology described in [26].

The thermal decomposition (dehydrogenation) of the titanium hydride powders was conducted using a specialized dehydrogenation apparatus, the schematic of which is depicted in Figure 1.

The apparatus comprises a sealed cylindrical container constructed from stainless steel (dehydrator), which is situated inside the PTGR-1.0-140 electric furnace. Heating is regulated using a digital thermal controller, with a measurement error of ±5 °C. On both sides of the container, pipelines are connected for the supply of argon and connection to the vacuum pump.

For the dehydrogenation process, a 0.02 kg sample of titanium hydride powder was placed on a molybdenum substrate (boat). This boat was then positioned within the dehydrator on a designated stand. To create a vacuum, a 2NVR-5DM oil vane-rotor two-stage vacuum pump was utilized, capable of achieving a residual pressure of 2.6 Pa. To minimize the residual air content in the system, argon was introduced into the container at a pressure of 0.1 MPa, followed by evacuation. This procedure was carried out twice to ensure the lowest possible residual air content in the dehydrator.

The dehydrogenation process (Fig. 2) entailed several steps. It commenced with vacuum drying at 300 °C for 60 min. Subsequently, the heating temperature was

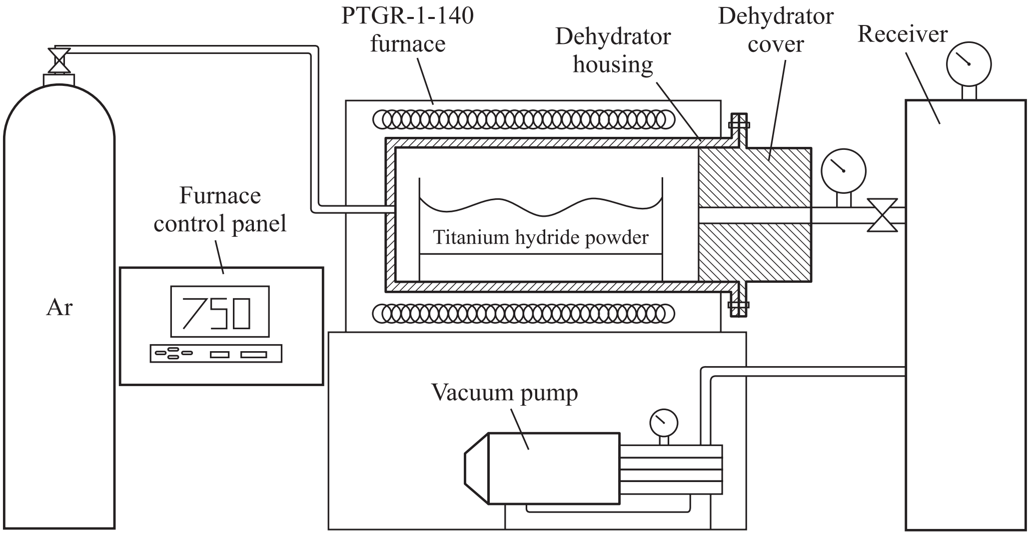

Fig. 1. Schematic view of facility for thermal dehydration

Рис. 1. Схематическое изображение установки для термического дегидрирования

raised to 750 °C and held constant for 40 min. Thermal decomposition of the titanium hydride involved heating the powder until the pressure in the system ceased to change. The initiation and cessation of hydrogen release were determined by monitoring the vacuum gauge's readings, indicating the start and end of pressure variations. The dehydrogenation parameters were chosen to prevent particle sintering. The cooling of the powders was carried out simultaneously with the furnace, and after complete cooling, the reactor was additionally purged with argon. The weight change of the dehydrogenated powder was calculated using equation:

$$\Delta m = \frac{m_h - m_d}{m_d} \cdot 100\ \%, \qquad (1)$$

where m_h is the weight of initial titanium hydride powder, and m_d is the weight of the powder after dehydrogenation. The measurement error for this calculation was ±0.1 g.

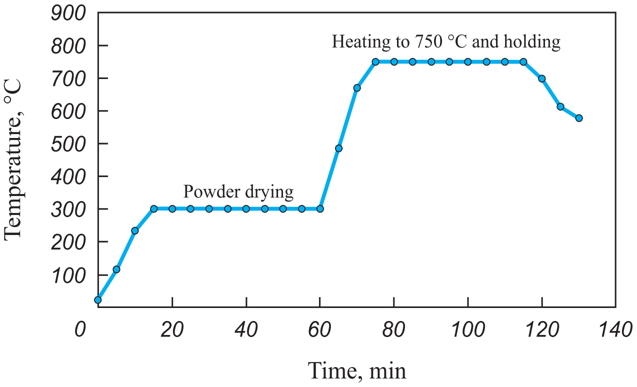

Fig. 2. Dehydration regime of powdered titanium samples

Рис. 2. Режим дегидрирования порошковых образцов титана

The particle size of the obtained powders was determined using a "MicroSizer 201" laser particle analyzer (LLC "VA Insalt", St. Petersburg, Russia). The measurement error did not exceed 1.2 %.

The particle morphology of the obtained titanium powder was examined using a "Zeiss Ultra plus" autoemission ultrahigh resolution scanning electron microscope (Carl Zeiss, Germany), which is based on "Ultra 55". This microscope offers a magnification range of 12–10^6, an accelerating voltage of 0.02 V to 30 kV, and a probe current of 4–20 nA.

The chemical composition of the materials under investigation was determined using analytical chemistry methods: oxygen and nitrogen were analyzed through reductive melting in a graphite crucible in a helium current, carbon content was determined via oxidative melting in a ceramic crucible, and hydrogen content was determined according to State Standard GOST 24956–81. Oxygen and carbon were detected by measuring the amount of CO_2 released through infrared absorption, while nitrogen was determined through thermal conductivity. The iron content in titanium was assessed using photocolorimetry. The instruments employed for these measurements include the TS-600 oxygen and nitrogen analyzer (Leco, USA), the RHEN-602 hydrogen analyzer (Leco, USA), the CS-600 carbon analyzer (Leco, USA), and the KFK-3-01 photometer (JSC "ZOMZ", Zagorsk, Russia) for iron content determination.

The bulk density of the obtained powders was determined in accordance to State Standard GOST 19440–94, while their compressibility (compactibility) was assessed following State Standard GOST 25280–90. Pycnometric density was determined based on State Standard GOST 2211–2020, considering the weight of the analytical sample and its true volume, measured with a pycnometer using toluene as a saturating liquid.

The specific surface area was measured using low-temperature nitrogen adsorption with a "Sorbi-M" device designed for determining the specific surface of porous materials (ZAO "META", Novosibirsk, Russia). Powder flowability was evaluated using a calibrated funnel (Hall device) in accordance with State Standard GOST 20899-98.

Result and discussions

Four distinct powder samples of dehydrogenated titanium, denoted as DH-PTK, DH-PTS, DH-PTM, and DH-PTOM, were obtained.

The initial titanium hydride powders contained 4.2 wt. % of hydrogen and primarily varied in their particle size distribution. When heated within the range of 300–400 °C, the process of titanium hydride decomposition initiates, leading to the release of hydrogen. However, even at higher temperatures, typically around 1000–1100 °C, dehydrogenation in this case doesn't reach completion. To lower the temperature required for dehydrogenation, vacuum treatment is employed. Achieving the permissible hydrogen content for technical-grade titanium (<0.10 %) attained under vacuum conditions at $t = 700 \div 800$ °C. During the initial stages of dehydrogenation, when the hydrogen content in titanium is relatively high, the rate of hydrogen release is notably significant [27].

During dehydrogenation, it was observed that the particle size plays a role in influencing the kinetics of hydrogen release (Table 1). The PTOM sample, characterized by the smallest particle size, exhibits the commencement of hydrogen desorption at a low temperature, $t_{\text{in}} = 520$ °C. For the coarser PTS and PTM powders, hydrogen release initiates at 550 °C and 540 °C, respectively. It can be inferred that larger particles require more heat to initiate this process, as evident in the case of the PTK sample, where hydrogen release commences at $t_{\text{in}} = 555$ °C.

Moreover, for the powders under examination, the time interval from the initiation of hydrogen release to its completion also differs. As particle size decreases, this time interval tends to increase, possibly due to incomplete dehydrogenation of the coarser particles.

To evaluate the extent of dehydrogenation, the samples were weighed both before and after the dehydrogenation process. It's important to note that as the particle size of the samples decreases, the reduction in weight after dehydrogenation becomes more significant. As indicated in Table 1, it is evident that coarse particles are not completely dehydrogenated, which is reflected in the short duration of hydrogen release and the relatively low weight loss.

Table 1. **Kinetics of dehydration of powdered samples of titanium hydride**

Таблица 1. **Кинетика процесса дегидрирования порошковых образцов гидрида титана**

Sample	Average particle size, μm	Hydrogen release		Change in weight, %
		t_{in}, °C	τ, min	
DH-PTK	82	555	25	–3.1
DH-PTS	48	550	27	–3.6
DH-PTM	36	540	29	–4.7
DH-PTOM	33	520	30	–5.8

The histograms in Figure 3 reveal that following the thermal decomposition of titanium hydride, there is a slight reduction in the particle size within the overall mass. This phenomenon is similar to what was observed in a previous study [28], where it was demonstrated that the thermal decomposition of scandium hydride powder results in a marginal decrease in the average linear particle size (by ~4 %). As reported in other publications [29], during the hydrogenation of titanium, there is an expansion of the unit cell volume by approximately 2.5 times, leading to a "swelling" of the particles. Presumably, after the removal of hydrogen, the titanium particles tend to revert to their original structure under the influence of temperature, causing them to decrease in volume. This effect is more pronounced in the PTK and PTS powder samples, which consist of coarser particles when compared to PTM and PTOM. The average linear particle size after dehydrogenation for the PTK, PTS, PTM, and PTOM samples decreased by roughly 24, 13, 12 and 10 %, respectively. Additionally, after dehydrogenation, there was a reduction in the number of particles within the range of 0.5 to 10 μm. It is likely that, at the chosen temperature, such particles are sintered with the primary fraction particles.

The structure of particles has a significant impact on the properties of titanium powder, and it is influenced by the methods used for production and powder processing, as well as the chemical composition. Electron microscopy was employed to examine the dehydrogenated titanium powder, and the results indicated that the particle shape of the original titanium hydride was preserved. Figure 4 provides an overall view of the dehydrogenated titanium powders obtained. It is noteworthy that the chosen dehydrogenation temperature did not alter the shape of the powder particles, which retained their polygonal fragmented structure.

In the detailed images of Figure 5 at higher magnification, individual particles of the dehydrogenated titanium powder can be closely examined. A portion of the fine particles tends to sinter with the coarser particles,

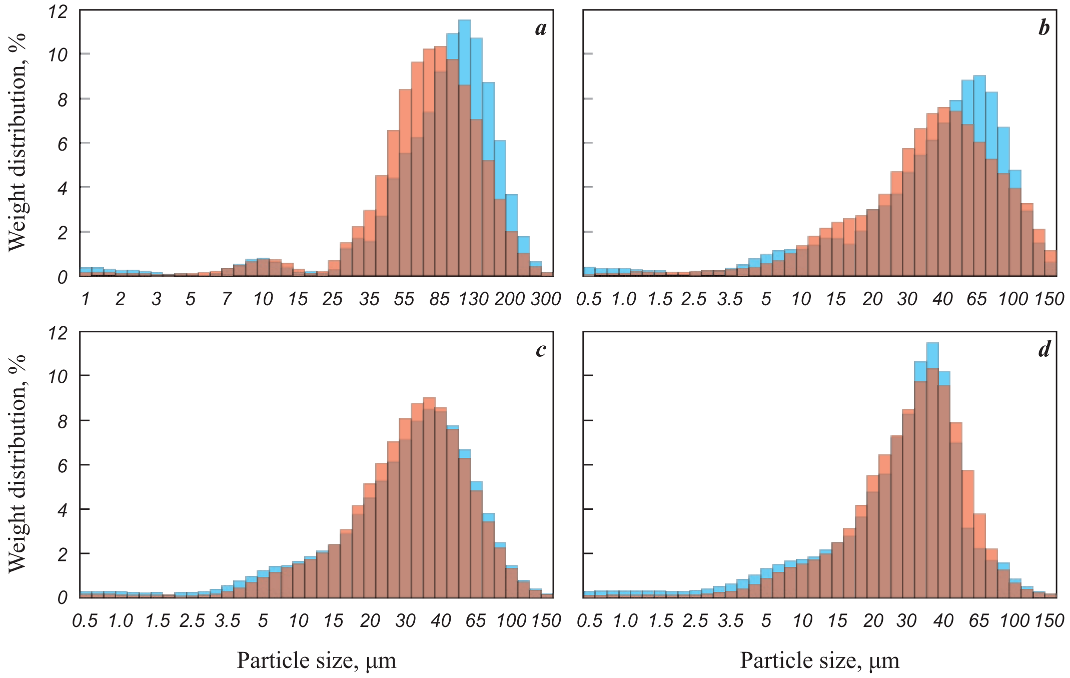

Fig. 3. Histograms of particle size distribution of powdered titanium before (🟦) and after (🟧) dehydration
a – PTK, ***b*** – PTS, ***c*** – PTM, ***d*** – PTOM

Рис. 3. Гистограммы распределения частиц порошков титана по размерам до (🟦) и после (🟧) дегидрирования
a – ПТК, ***b*** – ПТС, ***c*** – ПТМ, ***d*** – ПТОМ

giving rise to what are commonly referred to as "satellites." These satellite formations result in various types of micro-irregularities in the structure, which can potentially have adverse effects on the technological properties of the powders and the properties of the final powder products. The formation of satellites is influenced by the vacuum treatment and the specific temperature applied during dehydrogenation. As lowering the temperature and reducing the vacuum level are generally undesirable, it is recommended to pre-sieve the powder before dehydrogenation to eliminate fractions within the 0.5 to 10 μm range. It is worth noting that the surface of the titanium particles after dehydrogenation is characterized by the absence of pores and does not exhibit a developed surface structure.

The purity of titanium can be estimated through its hardness (*HB*), which tends to increase with higher impurity content. Among the impurities, oxygen and nitrogen, which form interstitial solid solutions with titanium, have a significant detrimental impact on the ductility of titanium and are considered harmful. The primary impurities also include carbon and iron. The influence of these main impurity elements on the hardness of titanium can be roughly expressed by the following empirical equation, MPa [27]:

$$\begin{gathered} HB = 1960\sqrt{\text{N, \%}} + 1580\sqrt{\text{O, \%}} + \\ + 450\sqrt{\text{C, \%}} + 200\sqrt{\text{Fe, \%}} + 57. \end{gathered} \tag{2}$$

As per Equation (2), nitrogen has the most substantial effect on the hardness of titanium, followed by oxygen, carbon, and iron. Nitrogen, which stabilizes the α phase of titanium, raises the temperature of the polymorphic transformation. Every 0.01 % increase in nitrogen content results in a 20 MPa increase in tensile strength and a 60 MPa increase in hardness. Oxygen also stabilizes the α phase, and a 0.1 % increase in oxygen content leads to a 12 MPa increase in tensile strength and a 40 MPa increase in hardness. Nitrogen and oxygen are interstitial atoms with high solubility in α titanium and are situated in octahedral voids, which enhances the rigidity of the interatomic bonds in titanium. Hydrogen is another highly detrimental impurity in titanium, as it significantly diminishes the ductility of the metal, particularly its impact toughness. Carbon has limited influence on the mentioned properties of titanium, as it only dissolves slightly in α titanium. The presence of iron impurities up to 0.5 % has a negligible impact on the mechanical properties of titanium.

The quality of products manufactured from titanium powders is directly linked to the purity of the initial powders. Thus, it is crucial to maintain the concentration of major impurities at a minimum level. Based on the results of chemical analysis (Table 2) of dehydrogenated titanium powders, it was observed that samples from the coarser fraction contain a higher level of residual hydrogen (0.2 wt. %) compared to the finer fraction (0.06 wt. %). This suggests that the selected

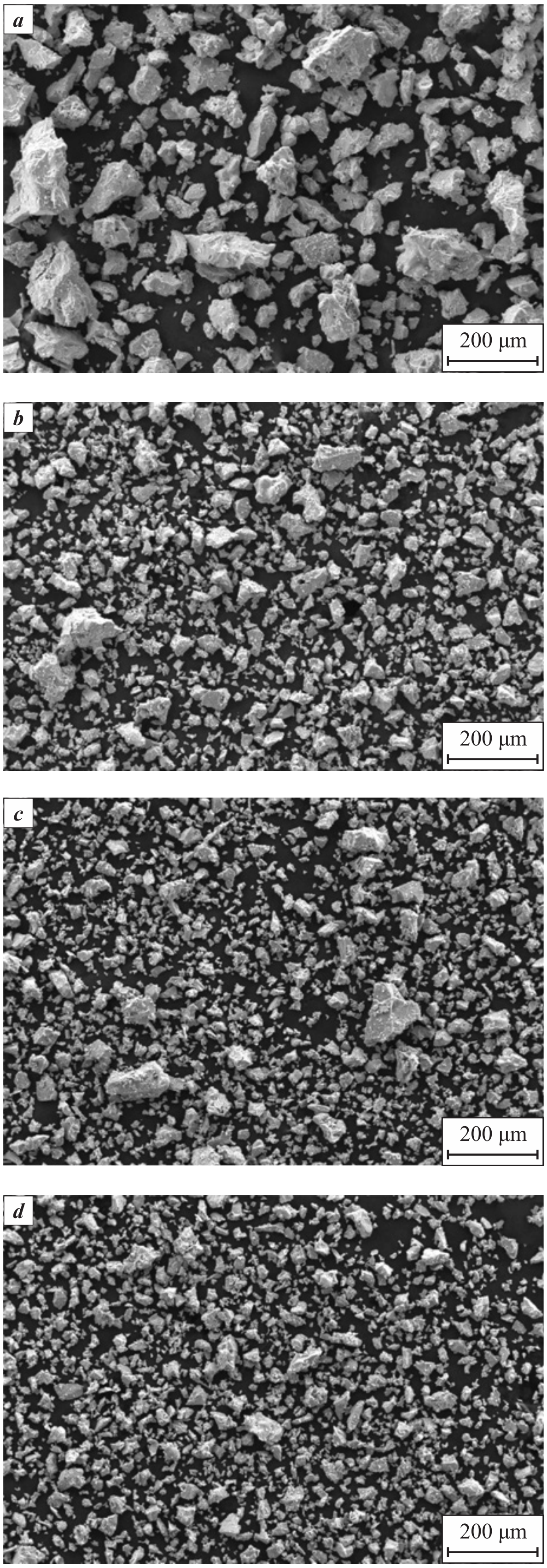

Fig. 4. General view of dehydrogenated titanium powders
a – PTK, ***b*** – PTS, ***c*** – PTM, ***d*** – PTOM

Рис. 4. Общий вид дегидрированных порошков титана
a – ПТК, ***b*** – ПТС, ***c*** – ПТМ, ***d*** – ПТОМ

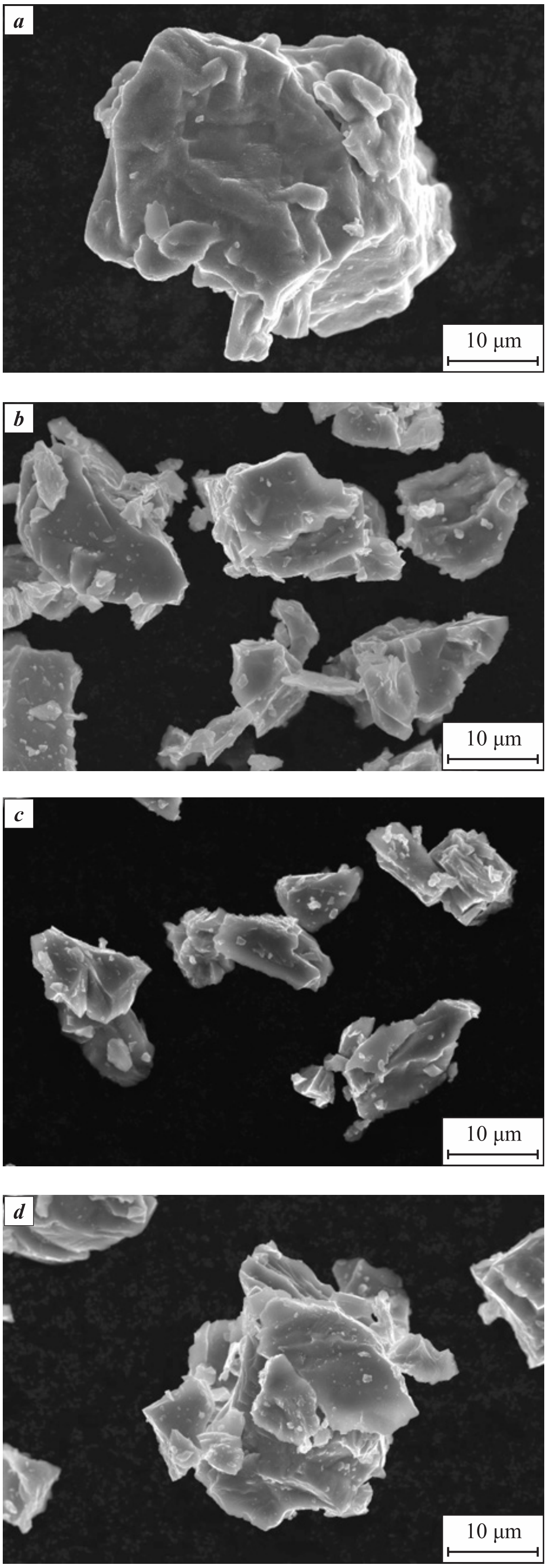

Fig. 5. Microstructure of dehydrogenated titanium powders
a – PTK, ***b*** – PTS, ***c*** – PTM, ***d*** – PTOM

Рис. 5. Микроструктура дегидрированных порошков титана
a – ПТК, ***b*** – ПТС, ***c*** – ПТМ, ***d*** – ПТОМ

dehydrogenation process is less effective for the PTK and PTS samples. Notably, during the dehydrogenation process, there is a reduction in gas impurities such as nitrogen and oxygen. This may be due to the vacuum facilitating active degassing of the powders [30]. Additionally, the hydrogen released during dehydrogenation can serve as a reducing agent, forming molecules with nitrogen and oxygen impurities, which are subsequently desorbed into the gas phase and eliminated [31; 32]. As a result, the PTM and PTOM powder samples exhibit the lowest levels of gas impurities (0.5–0.6 wt. %).

For practical applications, the technical characteristics of titanium powders are of great importance. The size and shape of particles are the primary factors that determine the technological properties of powders, including bulk density, flowability, and compressibility. The technological properties of dehydrogenated titanium powder are summarized in Table 3.

Bulk density represents a volumetric property of the powder, which is the ratio of its weight to its volume at free bulk density. The bulk density of dehydrogenated titanium powder increases in comparison to the hydride due to the higher density of pure titanium (4.5 g/cm^3). Additionally, there is a trend of decreasing bulk density with a reduction in the average particle size. Fine particles possess a higher specific surface area, which increases inter-particle friction, making it more challenging for them to move relative to each other, resulting in a lower bulk density.

Compactibility characterizes the change in powder density during compression and determines the ease and cost-effectiveness of the cold pressing process. Powder samples with larger particle sizes exhibit lower compactibility compared to titanium hydride, which, due to its brittleness, breaks down and fills voids. Pure titanium powder is more pliable, and therefore compacting the coarse fraction at a pressure of 200 MPa is challenging. The compactibility of dehydrogenated powder samples, in general, aligns with that of the initial titanium hydride powders.

The pycnometric (true) density of metal powders depends on their internal porosity, defects in the crystal lattice, oxide content, and usually differs from the theoretical density. Based on measurements of the pycnometric density of the dehydrogenated powder samples, it is evident that the PTK powder sample, with the highest impurity content (particularly hydrogen), has a lower density (4.43 g/cm^3). Generally, there is a dependency: the closer the pycnometric density is to the theoretical density, the lower the impurity content in the samples.

In evaluating the technological properties of powder materials, the specific surface area of their particles

Table 2. **Content of major impurities in the studied powder samples**

Таблица 2. **Содержание основных примесных элементов в исследуемых порошковых образцах**

Sample	Average particle size, μm	Content of elements, wt. %					
		C	N	O	Fe	H	Σ
Initial titanium hydride	–	0.09 ± 0.04	0.35 ± 0.03	0.26 ± 0.03	0.035 ± 0.01	4.20 ± 0.02	4.93
DH-PTK	82	0.13 ± 0.01	0.30 ± 0.02	0.27 ± 0.02	0.035 ± 0.01	0.20 ± 0.02	0.93
DH-PTS	48	0.14 ± 0.01	0.29 ± 0.02	0.25 ± 0.02	0.050 ± 0.01	0.13 ± 0.01	0.86
DH-PTM	36	0.13 ± 0.01	0.15 ± 0.01	0.20 ± 0.02	0.070 ± 0.01	0.08 ± 0.01	0.63
DH-PTOM	33	0.16 ± 0.01	0.02 ± 0.01	0.18 ± 0.01	0.080 ± 0.01	0.06 ± 0.01	0.50

Table 3. **Technological properties of the studied powdered samples**

Таблица 3. **Технологические свойства исследуемых порошковых образцов**

Sample	Average particle size, μm	Bulk density, g/cm^3	Compactibility, g/cm^3, under a pressure of 200 MPa	Pycnometric density, g/cm^3	Specific surface area, m^2/g	Flowabilit, s
PTK hydride	108	1.38 ± 0.04	2.83 ± 0.04	3.79 ± 0,01	0.6 ± 0.01	21.25
DH-PTK	82	1.74 ± 0.03	2.66 ± 0.01	4.43 ± 0,01	0.7 ± 0.01	16.60
PTS hydride	55	1.31 ± 0.03	2.85 ± 0.03	3.81 ± 0,01	0.6 ± 0.01	Does not flow
DH-PTS	48	1.56 ± 0.06	2.88 ± 0.01	4.48 ± 0,01	0.8 ± 0.01	Does not flow
PTM hydride	41	1.30 ± 0.02	2.86 ± 0.03	3.80 ± 0,01	0.6 ± 0.01	Does not flow
DH-PTM	36	1.46 ± 0.06	2.89 ± 0.03	4.50 ± 0,01	0.8 ± 0.01	Does not flow
PTOM hydride	37	1.16 ± 0.02	2.88 ± 0.03	3.72 ± 0,01	0.7 ± 0.01	Does not flow
DH-PTOM	33	1.39 ± 0.02	2.84 ± 0.02	4.50 ± 0.01	0.9 ± 0.01	Does not flow

is significant in several instances. Its value can provide insights into certain physical and chemical properties of powder materials, including the degree of dispersibility. As the average particle size of the powder samples decreases during dehydrogenation and the particle area increases due to satellites, the specific surface area of the dehydrogenated powders (0.7–0.9 m^2/g) is greater compared to that of the hydride (0.6–0.7 m^2/g).

Flowability denotes the ability of powders to flow out from the opening of a container under the influence of gravity. Flowability is influenced by factors such as powder density, particle size and shape, surface condition, humidity, and the nature of contact between particles. Good flowability is particularly important in cases of automatic pressing, where the productivity of the press is dependent on the rate of mold cavity filling. Poor fluidity can also lead to the production of items with non-uniform density. The resulting powders, due to the fragmented shape of the particles and structural defects, exhibit a low level of flowability, amounting to 16.6 s for the coarse fraction, while the fine fraction does not flow.

Conclusions

The presented study examines the impact of the particle size distribution of initial titanium hydride powders on their thermal decomposition process. It comprehensively investigates the physical, chemical, and technological properties of dehydrogenated titanium powders.

It has been determined that the chosen dehydrogenation process is better suited for the fine fraction with an average particle size of 35 μm, where complete dehydrogenation occurs without particle sintering. Larger particles (>60 μm) require higher dehydrogenation temperatures. During the thermal decomposition of titanium hydride, there is a significant reduction in the average linear size of powder particles, ranging from 5 to 20 % depending on the sample.

The dehydrogenation process does not alter the shape of the particles, which maintain their original polygonal fragmented structure. The study identifies the presence of “satellites” on large particles, which can introduce various forms of micro-irregularities in the structure, potentially affecting the technological properties of the powders and the properties of the final powder products. This factor should be taken into consideration during production, and powder separation should be carried out with care.

Chemical analysis results reveal that larger powder samples contain a higher amount of gas impurities (hydrogen, nitrogen, oxygen Σ 0.77 wt. %) compared to the fine fraction (Σ 0.26 wt. %). Presumably, this is due to the more complete dehydrogenation and degassing of the fine fraction under the selected regime.

The technological properties of dehydrogenated powders generally meet the requirements for their use in powder metallurgy. However, the presence of satellites and the fragmented shape of the particles significantly reduce the fluidity of the powders, which can lead to difficulties when using them in automated processes.

In conclusion, this comprehensive study of titanium powders obtained through SHS hydrogenation and thermal dehydrogenation demonstrates their potential for application in powder metallurgy.

References / Список литературы

1. Mal’shin V.M., Zavadovskaya V.N., Pampushko N.A. Metallurgy of titanium. Moscow: Metallurgiya, 1991. 208 p. (In Russ.).

Мальшин В.М., Завадовская В.Н., Пампушко Н.А. Металлургия титана. М.: Металлургия, 1991. 208 с.

2. Bolzoni L., Ruiz-Navas E.M., Gordo E. Powder metallurgy CP–Ti performances: Hydride–dehydride vs. sponge. *Materials & Design*. 2014;60:226–232. https://doi.org/10.1016/j.matdes.2014.04.005

3. Gramata V.A., Petrun’ko A.N., Galickii N.V., Olesov Yu.G., Sandler R.A. Titan. Moscow: Metallurgiya, 1983. 539 p. (In Russ.).

Грамата В.А., Петрунько А.Н., Галицкий Н.В., Олесов Ю.Г., Сандлер Р.А. Титан. М.: Металлургия, 1983. 539 с.

4. Panda A., Dobránsky J., Jančík M. Pandová I., Kačalová M. Advantages and effectiveness of the powder metallurgy in manufacturing technologies. *Metalurgiya*. 2018;57(4):353–356.

5. Fang Z.Z., Paramore J.D., Sun, P., Ravi Chandran K.S., Zhang Y., Xia Y., Cao F., Koopman M., Free M. Powder metallurgy of titanium – past, present, and future. *International Materials Reviews*. 2017;63(7):1–53. https://doi.org/10.1080/09506608.2017.1366003

6. Antsiferov V.N., Smetkin A.A., Yarmonov A.N., Peshcherenko S.N. Method for producing titanium powder: Patent 2178341 (RF). 2002. (In Russ.).

Анциферов В.Н., Сметкин А.А., Ярмонов А.Н., Пещеренко С.Н. Способ получения титанового порошка: Патент 2178341 (РФ). 2002.

7. Rymkevich D.A., Tankeev A.B., Bezdolja I.N., Teterin V.V., Permjakov A.A. Method of obtaining sponge titanium: Patent 2466198 (RF). 2015. (In Russ.).

Рымкевич Д.А., Танкеев А.Б., Бездоля И.Н., Тетерин В.В., Пермяков А.А. Способ получения губчатого титана: Патент 2466198 (РФ). 2015.

8. Withers J.C. 3 – Production of titanium powder by an electrolytic method and compaction of the powder. In book: *Titanium powder metallurgy*. 2015. P. 33–49. https://doi.org/10.1016/B978-0-12-800054-0.00003-4

9. Yanko T., Brener V., Ovchinnikov O. Production of spherical titanium alloy powders used in additive manufacturing from titanium scrap. In: *MATEC Web of Conferences* (The 14th World Conference on Titanium (Ti 2019), Nantes, France, 10–14 June 2019). 2020;321(07008). https://doi.org/10.1051/matecconf/202032107008

10. Goso X.C., Kale A. Production of titanium metal powder by the HDH process. *Journal of the Southern African Institute of Mining and Metallurgy*. 2011;111(3):203–210.

11. Heidloff A., Rieken J., Anderson I., Byrd D., Sears J., Glynn M., Ward R. Advanced gas atomization processing for Ti and Ti alloy powder manufacturing. *The Journal of the Minerals, Metals & Materials Society (JOM)*. 2010;62:35–41.
https://doi.org/10.1007/s11837-010-0075-x

12. Alishin M.I., Knjazev A.E. Production of metal powder compositions of high purity titanium alloys by induction gas atomization for additive technologies. *Trudy VIAM*. 2017;(11):35–43. (In Russ.).
https://dx.doi.org/ 10.18577/2307-6046-2017-0-11-5-5

Алишин М.И., Князев А.Е. Производство металлопорошковых композиций высокой чистоты титановых сплавов методом индукционной газовой атомизации для аддитивных технологий. *Труды ВИАМ*. 2017;(11):35–43.
https://dx.doi.org/ 10.18577/2307-6046-2017-0-11-5-5

13. Novikov A.N. A method for producing ultrafine powders of metal or metal alloys: Patent 2588931 (RF). 2016. (In Russ.).

Новиков А.Н. Способ получения ультрадисперсных порошков металла или металлических сплавов: Патент 2588931 (РФ). 2016.

14. Sun P., Fang Z.Z., Xia Y., Zhang Y., Zhou C. A novel method for production of spherical Ti–6Al–4V powder for additive manufacturing. *Powder Technology*. 2016;301: 331–335. https://doi.org/10.1016/j.powtec.2016.06.022

15. Kasimtsev A.V., Zhigunov V.V., Tabachkova N.Y. The composition, structure, and properties of calcium-hydride powder of titanium carbide. *Russian Journal of Non-Ferrous Metals*. 2009;50(3):276–280.
https://doi.org/10.3103/S1067821209030171

16. Xia Y., Fang Z.Z., Zhang T., Zhang Y., Sun P., Huang Z. Deoxygenation of titanium hydride with calcium hydride. In: *Proceedings of the 13th World Conference on Titanium Ti-2015* (Manchester Grand Hyatt, San Diego, California, USA, 16–20 August 2015). John Wiley & Sons, Inc., 2016. P. 135–137. https://doi.org/10.1002/9781119296126.ch20

17. Neikov O.D., Gopienko V.G. Production of titanium and titanium alloy powders. In: *Handbook of non-ferrous metal powders*. Elsevier Ltd., 2009. P. 549–570.
https://doi.org/10.1016/B978-0-08-100543-9.00018-X

18. Ivasishin O., Moxson V. 8 – Low-cost titanium hydride powder metallurgy. In: *Titanium powder metallurgy*. Elsevier Inc., 2015. P. 117–148.
https://doi.org/10.1016/B978-0-12-800054-0.00008-3

19. Abakumov G., Duz V., Ivasishin O., Moxson V., Savvakin D. High performance titanium powder metallurgy components produced from hydrogenated titanium powder by low cost blended elemental approach. In: *Proceedings of the 12th World Conference on Titanium Ti-2011* (Beijing, China, 19–24 June 2011). Beijing: Science Press, 2012. Vol. 2. P. 1639–1643.

20. Beshkarev V.T., Gasanov A.A., Yuzhakova E.A., Ivanov V.V., Kartsev V.E., Kotlyarov V.I., Kozlov R.Yu. Method for obtaining finely dispersed spherical titanium-containing powders: Patent 2631692 (RF). 2016. (In Russ.).

Бешкарев В.Т., Гасанов А.А., Южакова Е.А., Иванов В.В., Карцев В.Е., Котляров В.И., Козлов Р.Ю. Способ получения мелкодисперсных сферических титансодержащих порошков: Патент 2631692 (РФ). 2016.

21. Oh J.M., Roh K.M., Lee B.K., Suh C.Y., Kim W., Kwon H., Lim J.W. Preparation of low oxygen content alloy powder from Ti binary alloy scrap by hydrogenation–dehydrogenation and deoxidation process. *Journal of Alloys and Compounds*. 2014;593:61–66.
https://doi.org/10.1016/j.jallcom.2014.01.033

22. Doluhanjan S.K. SHS is a method for producing hydrogen storages. *Al'ternativnaya energetika i ekologiya*. 2005;(11):13–16. (In Russ.).

Долуханян С.К. СВС-метод получения аккумуляторов водорода. *Альтернативная энергетика и экология*. 2005;(11):13–16.

23. Pavlenko D.V. Influence of titanium powder parameters on the strength of sintered semi-finished products. *Novi materiali i tekhnologii v metalurgii ta mashinobuduvanni*. 2014;(2):87–92. (In Russ.).

Павленко Д.В. Влияние параметров порошков титана на прочность спеченных полуфабрикатов. *Нові матеріали і технології в металургії та машинобудуванні*. 2014;(2):87–92.

24. Knyazev A.E., Nerush S.V., Alishin M.I., Kuko I.S. Investigations of technological properties of metal powder compositions of titanium alloys VT6 and VT20 obtained by induction melting and gas atomization. *Trudy VIAM*. 2017;59(11):44–53. (In Russ.).
https://doi.org/10.18577/2307-6046-2017-0-11-6-6

Князев А.Е., Неруш С.В., Алишин М.И., Куко И.С. Исследования технологических свойств металлопорошковых композиций титановых сплавов ВТ6 и ВТ20, полученных методом индукционной плавки и газовой атомизации. *Труды ВИАМ*. 2017;59(11):44–53.
https://doi.org/10.18577/2307-6046-2017-0-11-6-6

25. Chen B., Shen J., Ye X., Umeda J., Kondoh K. Advanced mechanical properties of powder metallurgy commercially pure titanium with a high oxygen concentration. *Journal of Materials Research*. 2017;32(19):3769–3776.
https://doi.org/10.1557/jmr.2017.338

26. Cherezov N.P., Alymov M.I. Structure and properties of titanium hydride powder obtained from titanium sponge by SHS hydrogenation. *Powder Matallurgy and Functional Coatings*. 2022;16(4):15–24. (In Russ.).
https://dx.doi.org/10.17073/1997-308X-2022-4-15-24

Черезов Н.П., Алымов М.И. Структура и свойства порошка гидрида титана, полученного из титановой губки методом СВС-гидрирования. *Известия вузов. Порошковая металлургия и функциональные покрытия*. 2022;16(4):15–24.
https://dx.doi.org/10.17073/1997-308X-2022-4-15-24

27. Ustinov V.S., Olesov Yu.G., Antipin L.N., Drozdenko V.A. Titanium powder metallurgy. Moscow: Metallurgiya, 1973. 248 p. (In Russ.).

Устинов В.С., Олесов Ю.Г., Антипин Л.Н., Дрозденко В.А. Порошковая металлургия титана. М.: Металлургия, 1973. 248 с.

28. Tsarev M.V., Zabavin E.V., Mokrushin V.V., Berezhko P.G. Change in the particle size of powdered metals during their hydrogenation and dehydrogenation. In: *Interaction of hydrogen isotopes with structural materials. IHISM'11 JUNIOR*: The Seventh International School of young scientists and specialists named after A.A. Kurdyumov (Zvenigorod, 24–28 October 2011). Sarov: FGUP "RFYaTs–VNIIEF", 2012. P. 379–384. (In Russ.).

Царев М.В., Забавин Е.В., Мокрушин В.В., Бережко П.Г. Изменение размера частиц порошковых металлов в процессе их гидрирования и дегидрирования. В сб.: *Взаимодействие изотопов водорода с конструкционными материалами. IHISM'11 JUNIOR*: Сборник докладов Седьмой Международной школы молодых ученых и специалистов им. А.А. Курдюмова (Звенигород, 24–28 октября 2011 г.). Саров: ФГУП «РФЯЦ–ВНИИЭФ», 2012. С. 379–384.

29. Rudskih V.V., Volkova T.S., Levchenkova O.N., Zharkov A.Yu., Svetlakov S.V. Hydrogenation of titanium fractions at reduced hydrogen pressure. In: *Interaction of hydrogen isotopes with structural materials. IHISM'14*: The Fifth International Conference and the Ninth International School of young scientists and specialists named after A.A. Kurdyumov (Sarov, 7–11 June 2014). Sarov: FGUP "RFYaTs–VNIIEF", 2014. P. 265–276. (In Russ.).

Рудских В.В., Волкова Т.С., Левченкова О.Н., Жарков А.Ю., Светлаков С.В. Гидрирование дроби титана при пониженном давлении водорода. В сб.: *Взаимодействие изотопов водорода с конструкционными материалами. IHISM'14*: Сборник докладов Пятой Международной конференции и Девятой Международной школы молодых ученых и специалистов им. А.А. Курдюмова (Саров, 7–11 июля 2014 г.). Саров: ФГУП «РФЯЦ–ВНИИЭФ», 2014. С. 265–276.

30. Shapovalova O.M., Babenko E.P. The influence of the heating temperature on the process of gas saturation of titanium powders. *Novi materiali i tekhnologii v metalurgii ta mashinobuduvanni*. 2008;(2):93–98. (In Russ.).

Шаповалова О.М., Бабенко Е.П. Влияние температуры нагрева на процесс насыщения газами титановых порошков. *Нові матеріали і технології в металургії та машинобудуванні*. 2008;(2):93–98.

31. Liu H., Lixian L., Liu Y. Vacuum activation assisted hydrogenation-dehydrogenation for preparing high-quality zirconium powder. *Materials and Manufacturing Processes*. 2019;34(6):630–636.
https://dx.doi.org/ 10.1080/10426914.2019.1566610

32. Park Choi, Kang Jang-Won. Oxygen reduction behavior of HDH TiH_2 powder during dehydrogenation reaction. *Metals*. 2019;9(11):1154.
https://doi.org/10.3390/met9111154

Information about the Authors

Nikita P. Cherezov – Junior Researcher of the Laboratory of high-energy methods of synthesis of ultrahigh-temperature ceramic materials, Merzhanov Institute of Structural Macrokinetics and Materials Science of the Russian Academy of Sciences (ISMAN)
ORCID: 0000-0003-4942-5520
E-mail: cherezovnikita@gmail.com

Mikhail I. Alymov – Dr. Sci. (Eng.), Corresponding Member of the Russian Academy of Sciences, Director of ISMAN
ORCID: 0000-0001-6147-5753
E-mail: alymov.mi@gmail.com

Сведения об авторах

Никита Петрович Черезов – мл. науч. сотрудник лаборатории высокоэнергетических методов синтеза сверхвысокотемпературных керамических материалов Института структурной макрокинетики и проблем материаловедения им. А.Г. Мержанова РАН (ИСМАН)
ORCID: 0000-0003-4942-5520
E-mail: cherezovnikita@gmail.com

Михаил Иванович Алымов – д.т.н., чл.-корр. РАН, директор ИСМАН
ORCID: 0000-0001-6147-5753
E-mail: alymov.mi@gmail.com

Contribution of the Authors

N. P. Cherezov – formulated the main concept, the goal, and objectives of the study, prepared and conducted the experiments, analyzed the research results, wrote the manuscript, formulated the conclusions.
M. I. Alymov – provided scientific guidance, revised the manuscript, and contributed to the conclusions.

Вклад авторов

Н. П. Черезов – формирование основной концепции, постановка цели и задачи исследования, подготовка экспериментов и их проведение, анализ результатов исследований, написание текста статьи, формулировка выводов.
М. И. Алымов – научное руководство, корректировка текста и выводов статьи.

Received 05.12.2022
Revised 16.01.2023
Accepted 23.01.2023

Статья поступила 05.12.2022 г.
Доработана 16.01.2023 г.
Принята к публикации 23.01.2023 г.

Production Processes and Properties of Powders
Процессы получения и свойства порошков

UTC 621.762

https://doi.org/10.17073/1997-308X-2023-4-16-24

Research article
Научная статья

Characteristics of granule solidification in gas atomization of molten beryllium

B. V. Syrnev ✉, G. S. Pestova, O. V. Semilutskaya, F. S. Tuganbaev

Serikbaev East Kazakhstan Technical University (EKTU)
19 D. Serikbaev Str., Ust-Kamenogorsk 070004, Kazakhstan

✉ izusan@mail.ru

Abstract. Experimental and analytical studies on gas atomization of the molten beryllium and the production of beryllium granules are presented. The impact of various factors, including the choice of gas (nitrogen or helium), the cooling gas flow rate (ranging from 300 to 650 m/s), melt temperature, and droplet size (<500 μm), on the cooling rate and granule properties, is demonstrated. It has been determined that the solidification of beryllium granules can occur through two distinct mechanisms depending on the atomization process. These mechanisms include crystallization and amorphization (glass transition). When beryllium melt is atomized with nitrogen, granules with diameters less than 100 μm solidify via the amorphization mechanism (glass transition), while those with diameters exceeding 300 μm solidify through crystallization. In such cases, a portion of granules with sizes ranging from 100 to 300 μm undergoes a mixed mechanism solidification. In this process, the surface becomes amorphous, while the central part crystallizes, resulting in the formation of a "shell" on the surface, marking the transition from the glass transition mechanism to the crystallization mechanism. The thickness of this "shell" depends on the granule diameter, measuring 10–15 μm for 300 μm granules and 20–25 μm for 100 μm granules. The findings from this research align well with the hypothesis of a glass-crystalline mechanism of beryllium granule solidification, which leads to their separation at the interfacial boundary. Such solidification through a mixed mechanism results in the creation of a removable "crust" on the granule, which is typically more contaminated with impurities. Understanding this effect opens up possibilities for practical applications in the production of specialized materials from beryllium. The ability to separate the "crust" from the "core" provides the conditions for obtaining specialized sintered beryllium grades suitable for use in nuclear reactors and foil production, where a beryllium microstructure with "clean" boundaries is essential.

Keywords: beryllium, granules, gas atomization, cooling rate, crystallization, amorphization, temperature, heat transfer, thermal conductivity

For citation: Syrnev B.V., Pestova G.S., Semilutskaya O.V., Tuganbaev F.S. Characteristics of granule solidification in gas atomization of molten beryllium. *Powder Metallurgy and Functional Coatings*. 2023;17(4):16–24. https://doi.org/10.17073/1997-308X-2023-4-16-24

Особенности процесса затвердевания гранул при газоструйном распылении расплава бериллия

Б. В. Сырнев ✉, Г. С. Пестова, О. В. Семилуцкая, Ф. С. Туганбаев

Восточно-Казахстанский технический университет им. Д. Серикбаева
Казахстан, 070004, г. Усть-Каменогорск, ул. Д. Серикбаева, 19

✉ izusan@mail.ru

Аннотация. Представлены результаты экспериментально-аналитических исследований процесса газоструйного диспергирования расплава и получения бериллиевых гранул. Показано влияние природы (азот, гелий), скорости подачи охлаждающего газа (300–650 м/с), температуры расплава и размера образующихся капель (<500 мкм) на скорость охлаждения и свойства гранул. Установлено, что в зависимости от регламента распыления затвердевание бериллиевых гранул может происходить по двум механизмам: кристаллизация, аморфизация (стеклование). При распылении азотом расплава бериллия гранулы диаметром менее 100 мкм затвердевают по механизму стеклования (аморфизируются), а диаметром более 300 мкм – по механизму кристаллизации. При этом определенная фракция гранул (размером от 100 до 300 мкм) затвердевает по смешанному механизму – поверхность аморфизируется, а центральная часть кристаллизуется, в результате чего происходит отслаивание «скорлупы» по поверхности перехода от механизма стеклования к механизму кристаллизации. Толщина «скорлупы» зависит от диаметра гранулы и составляет 10–15 мкм (на гранулах 300 мкм) и 20–25 мкм (на гранулах 100 мкм). Полученные результаты исследований хорошо согласуются с гипотезой о стеклокристаллическом механизме затвердевания гранул бериллия, обуславливающем расслоение их по межфазной границе. Такое затвердевание, по смешанному механизму, приводит к образованию легко отслаиваемой «корочки» на грануле, которая наиболее загрязнена примесями. Понимание изученного эффекта создает перспективы для его практического применения при получении специальных материалов из бериллия. Возможность отделения «корочки» от «ядрышка» создает условия для получения особых сортов спеченного бериллия для использования в атомных реакторах и производстве фольги, где необходима микроструктура бериллия с «чистыми» границами.

Ключевые слова: бериллий, гранулы, газоструйное распыление, скорость охлаждения, кристаллизация, аморфизация, температура, теплообмен, теплопроводность

Для цитирования: Сырнев Б.В., Пестова Г.С., Семилуцкая О.В., Туганбаев Ф.С. Особенности процесса затвердевания гранул при газоструйном распылении расплава бериллия. *Известия вузов. Порошковая металлургия и функциональные покрытия*. 2023;17(4):16–24. https://doi.org/10.17073/1997-308X-2023-4-16-24

Introduction

The beryllium industry employs various methods to produce beryllium powders, with mechanical methods being the most widely used for reducing the particle size of technical beryllium ingots, electro-refined beryllium flakes, and distilled beryllium granules to less than 56 μm. However, it's important to note that mechanical grinding during this process generates heat and leads to surface oxidation of the powders. The surface oxidation results in the presence of beryllium oxide on the powder particles, and this oxide material is subsequently incorporated into the grain boundaries of the compacted beryllium. It serves as a dispersion-strengthening phase [1–6]. This particular phase plays a significant role in influencing the processes of structure formation and the development of both strength and plastic properties in sintered beryllium.

In [7–9], novel insights into the mechanism of degradation of an oxide film covering beryllium particles during the hot consolidation of powders were substantiated. It has been demonstrated that the initially amorphous beryllium oxide film undergoes crystallization at temperatures exceeding 700 °C. The crystallization mechanism, whether homogeneous or heterogeneous, depends on the presence of fusible impurities. This, in turn, dictates the nanostructure of the resulting discrete oxide particles and, consequently, influences the strengthening effect observed in sintered beryllium. These established quantitative patterns contribute to the scientific foundation for controlling the mechanical properties of sintered beryllium. This is especially crucial in ensuring the quality of "instrumental" beryllium grades [10–16].

Nonetheless, there are other significant applications of beryllium where the presence of beryllium oxide and other impurities on grain boundaries, and correspondingly on the particle surface of initial powders, is undesirable. These applications pertain to beryllium grades used in nuclear reactors, specifically as neutron reflectors, and in foil production. In the former case, impurities at the grain boundaries can adversely affect the relaxation of thermal stresses that occur during reactor operation, potentially leading to the development of cracks in critical components. In the latter case, the presence of oxide at the grain boundaries reduces the impermeability (vacuum density) of thin foils, which is unacceptable when employed in *X*-ray technology.

There is existing literature on the utilization of distilled coarse-grained beryllium for reactor-grade applications [3; 6; 17], and fine-grained beryllium produced through hydride technology for foil-grade purposes [18]. Nevertheless, the application of these technologies has limitations.

In the 1970s, significant advancements were made in beryllium granule metallurgy. Specialized equipment was developed for the atomization of molten beryllium, including rotary atomizers (VIAM, Russia), centrifugal atomizers (Leybold–Heareus, Germany), and gas atomizers "Sphere" (KhPTI, Ukraine). However, experimental studies revealed that despite decreased contamination, the granule surface still retained impurities due to interaction with the gas atmosphere.

In practical applications of gas atomization for spraying beryllium melt, it was observed that certain-sized granules developed a "shell" upon solidification. This "shell" comprised beryllium enriched with oxygen, nitrogen, and iron (Fig. 1).

Understanding the underlying causes and mechanisms responsible for the formation of the "shell" is crucial for its utilization in quality control of both granules and densely sintered beryllium materials. It was essential to investigate the hypothesis that the formation and subsequent detachment of the "shell" result from a significant alteration in volumetric contraction during the granule's solidification process. This transformation occurs due to the shift from the glass transition mechanism to the crystallization mechanism, accompanied by a reduction in the cooling rate as the solidification front progresses from

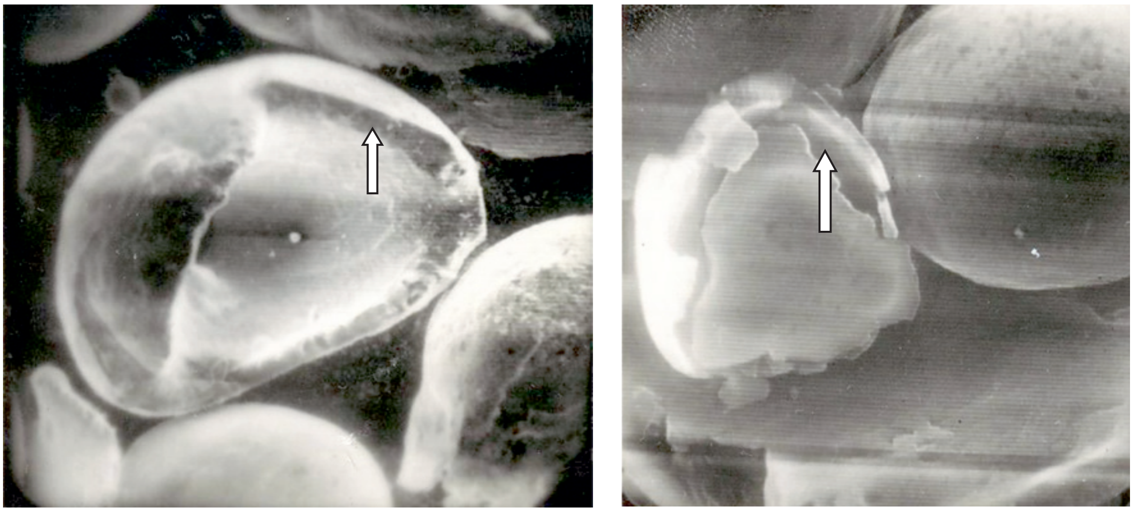

Fig. 1. Microimages of granules captured by a scanning electron microscope (×200)
The “shell” is highlighted by arrows

Рис. 1. Микрофотографии гранул, снятые на растровом электронном микроскопе (×200)
Стрелками показана «скорлупа»

the granule’s surface to its core. During the crystallization of the melt, the granule’s density increases from 1.69 to 1.85 g/cm^3, leading to an 8.6 % reduction in the granule’s volume 8.6 % [2]. In contrast, when solidification takes place through the glass transition (amorphization) mechanism, the reduction in the granule’s volume is significantly less (Fig. 2).

Published information regarding the feasibility of obtaining beryllium metallic glasses is limited. However, it is noteworthy that the glass transition of granules composed of pure metals can be facilitated when the metal is saturated with gases [19; 20]. This saturation can be achieved through gas atomization techniques, specifically employing gases such as nitrogen in the atomization of beryllium, at both subsonic (300 m/s) and supersonic (650 m/s) velocities. The research aimed to investigate the dynamic changes in cooling rates experienced by beryllium granules as the solidification front progresses from the granule’s surface towards its center. The primary objective was to determine the conditions necessary for implementing a combined “glass-crystalline” solidification mechanism for these granules.

The objective of this study was to investigate the gas jet spraying method for beryllium melt with the aim of identifying technological procedures for the production of granules. These granules would possess a structure that, during subsequent processing, facilitates the efficient removal of impurities from their surfaces.

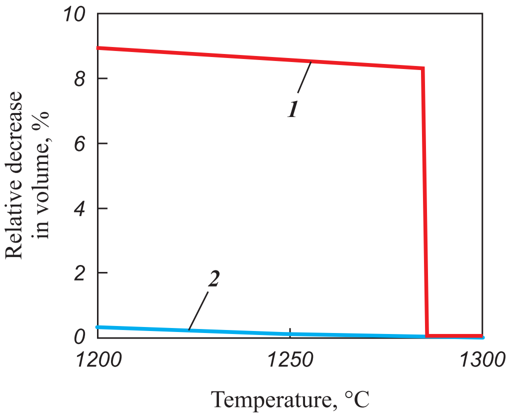

Fig. 2. Hypothetical curve of volumetric shrinkage during melt solidification by crystallization (*1*) and glass transition (amorphization) (*2*)

Рис. 2. Гипотетическая кривая объемной усадки при затвердевании расплава по механизмам кристаллизации (*1*) и стеклования (аморфизации) (*2*)

Experimental

Numerical studies into the solidification of beryllium melt droplets were conducted using two approaches: a graphical-analytical method employing universal dimensionless graphs [21], and an analytical method involving the solution of differential equations governing heat conduction [22]. In the first approach, the study addressed the problem of non-steady-state heat conduction during the incremental solidification of a cooled sphere due to uniform convective heat dissipation from its surface (Fig. 3).

The calculations did not account for variations in droplet volume during cooling, nor did they consider the influence of the already solidified droplet layer on the cooling process. The temperature of the gaseous medium was assumed to be 40 °C. At the initial time ($\tau = 0$), all points within the droplet with a radius R_g possessed the same melt temperature $T_m = 1350$ °C.

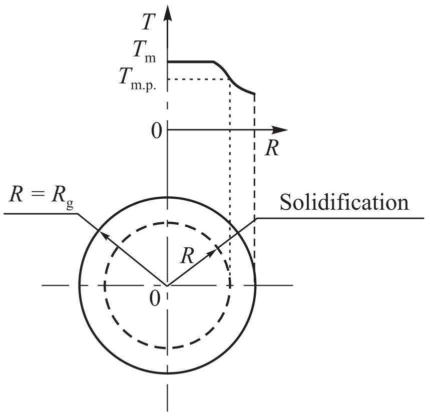

Fig. 3. Schematic representation of granule solidification
$T_{m.p.}$, T_{melt} – melting point and beryllium melt temperature, respectively; R_g – granule radius

Рис. 3. Схема затвердевания гранулы
$T_{пл}$, $T_р$ – температуры плавления и расплава бериллия соответственно; $R_ш$ – радиус гранулы

Under these specified conditions, the temperature at any point within the droplet becomes solely a function of time and radius. Numerical investigations were conducted for beryllium droplets with diameters ranging from 50 to 400 μm while being subjected to cooling by nitrogen, helium, and air at both subsonic (300 m/s) and supersonic (650 m/s) velocities.

The heat exchange mode between the droplet (or granule) and the coolant flow is determined by the Reynolds criterion (Re) (Fig. 4):

$$\mathrm{Re} = \frac{V_g d}{\nu_g},$$

where V_g represents the gas flow velocity, d stands for the droplet diameter, ν_g denotes the kinematic viscosity of the flowing medium.

In the context of heat exchange involving a spherical body and a gas flow, the Nusselt criterion (Nu) governs both laminar and turbulent regimes:

$$\mathrm{Nu} = 2 + 0.69\,\mathrm{Re}^{0,5}\,\mathrm{Pr}^{0,33} = \frac{\alpha d}{\lambda_g},$$

where Pr signifies the Prandtl criterion, equal to 0.67 for monatomic gases and 0.72 for diatomic gases; α represents the coefficient of heat transfer, W/(m^2·K); λ_g denotes the thermal conductivity coefficient of the energy-carrying gas, W/(m·K).

The Biot number (Bi) quantifies the relationship between the rate of heat transfer and the rate of heat conduction within the granule (Fig. 5):

$$\mathrm{Bi} = \frac{\alpha d}{\lambda_T},$$

where λ_T represents the thermal conductivity of the melt, W/(m·K).

The total heat released by the granule prior to solidification is determined as follows:

$$q_b = c_m (T_m - T_{m.p.}),$$

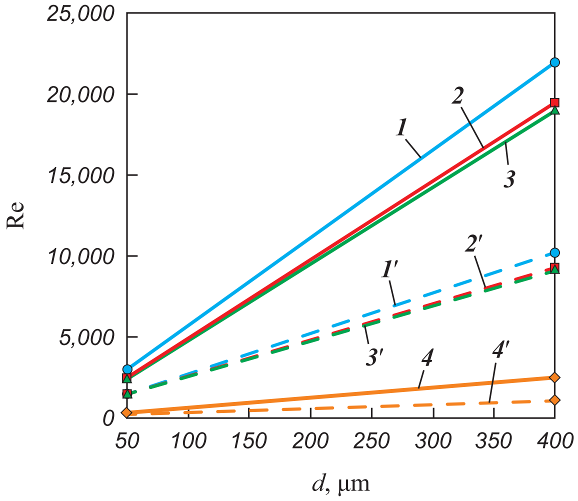

Fig. 4. Reynolds criterion for gas flow as a function of granule diameter, gas type, and gas flow rate
1, **1′** – argon; **2**, **2′** – air; **3**, **3′** – nitrogen; **4**, **4′** – helium
V_g = 650 m/s (**1**–**4**) and 300 m/s (**1′**–**4′**)

Рис. 4. Критерий Рейнольдса для газового потока в зависимости от диаметра гранул, вида газа и скорости дутья
1, **1′** – аргон; **2**, **2′** – воздух; **3**, **3′** – азот; **4**, **4′** – гелий
$V_г$ = 650 м/с (**1**–**4**) и 300 м/с (**1′**–**4′**)

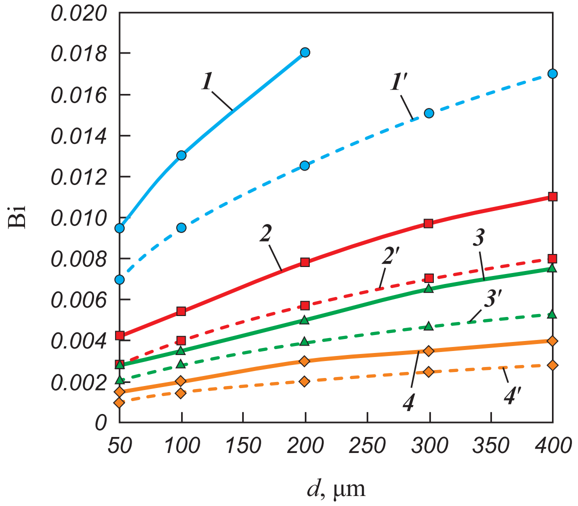

Fig. 5. Biot number for gas flow as a function of granule diameter, gas type, and gas flow rate
1, **1′** – helium; **2**, **2′** – nitrogen; **3**, **3′** – argon; **4**, **4′** – air
V_g = 650 m/s (**1**–**4**) and 300 m/s (**1′**–**4′**)

Рис. 5. Критерий Био для газового потока в зависимости от диаметра гранул, вида газа и скорости дутья
1, **1′** – гелий; **2**, **2′** – азот; **3**, **3′** – аргон; **4**, **4′** – воздух
$V_г$ = 650 м/с (**1**–**4**) и 300 м/с (**1′**–**4′**)

where c_m signifies the specific heat capacity, T_m denotes the melt temperature, $T_{m.p.}$ represents the melting point of beryllium (1285 °C).

Time and cooling rates for different cooling conditions were determined using dimensionless graphs [14], which represent numerical solutions of the following set of equations:

$$Y\frac{\partial\theta^*}{\partial\tau^*}=\frac{\partial^2\theta^*}{\partial r^{*2}}+2\frac{\partial\theta^*}{r^*\partial r^*}\ \ (\text{at } R^*<r^*<1),$$

$$-\frac{\partial\theta^*}{\partial r^*}=\frac{\theta^*}{\beta}\ \ (\text{at } r^*=1),$$

$$\frac{dR^*}{d\tau^*}=\frac{\partial\theta^*}{\partial r^*}\ \ (\text{at } r^*=R^*),$$

where $Y=\dfrac{c_T\left(T_{m.p.}-\theta\right)}{q_b}$ is the relative heat content of solid phase; c_T is the specific heat content of granule; θ is the granule temperature; $\theta^*=\dfrac{\theta-1}{T_{m.p.}-t}$ is the dimensionless temperature; t is the gas temperature; $\tau^*=\dfrac{\tau\lambda_T\left(T_{m.p.}-t\right)}{R_g^2\rho_T q_b}$ is the dimensionless time; $r^*=\dfrac{r}{R_g}$, $R^*=\dfrac{R}{R_g}$ are the relative radii, representing the current radius and solidification front; $\beta = 1/\text{Bi}$ is the coefficient (Fig. 6); r is the “current” radius varying from 0 to R_g.

The calculation of cooling time was conducted as follows:

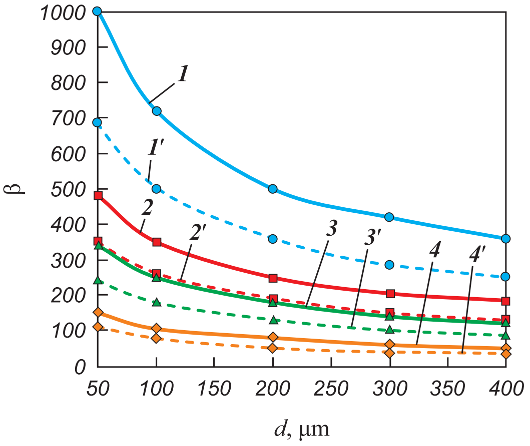

Fig. 6. $\beta = 1/\text{Bi}$ as a function of granule diameter, gas type, and gas flow rate
1, 1′ – air; ***2, 2′*** – argon; ***3, 3′*** – nitrogen; ***4, 4′*** – helium
V_g = 650 m/s (***1–4***) and 300 m/s (***1′–4′***)

Рис. 6. Коэффициент $\beta = 1/\text{Bi}$ для газового потока в зависимости от диаметра гранул, вида газа и скорости дутья
1, 1′ – воздух; ***2, 2′*** – аргон; ***3, 3′*** – азот; ***4, 4′*** – гелий
$V_г$ = 650 м/с (***1–4***) и 300 м/с (***1′–4′***)

$$\tau=\frac{\tau^*\rho_T q_b R_g^2}{\lambda_T\left(T_m-T_g\right)},$$

where τ^* is the relative time determined through the graphs [14]; ρ_T is the melt density; R_g is the granule radius; T_g is the temperature of the dispersing gas.

The calculation of cooling rate was performed as follows:

$$V_{cool}=\frac{T_m-T_{m.p.}}{\tau}.$$

The outcomes of the numerical research employing the graphical analytical method are depicted in Fig. 7.

In order to assess the accuracy of data obtained through the first method, numerical investigations were carried out using the second method. This involved solving the following differential equation:

$$\frac{\partial\theta}{\partial\tau}=\alpha\left(\frac{\partial^2\theta}{\partial r^2}+\frac{2\partial\theta}{r\partial r}\right).$$

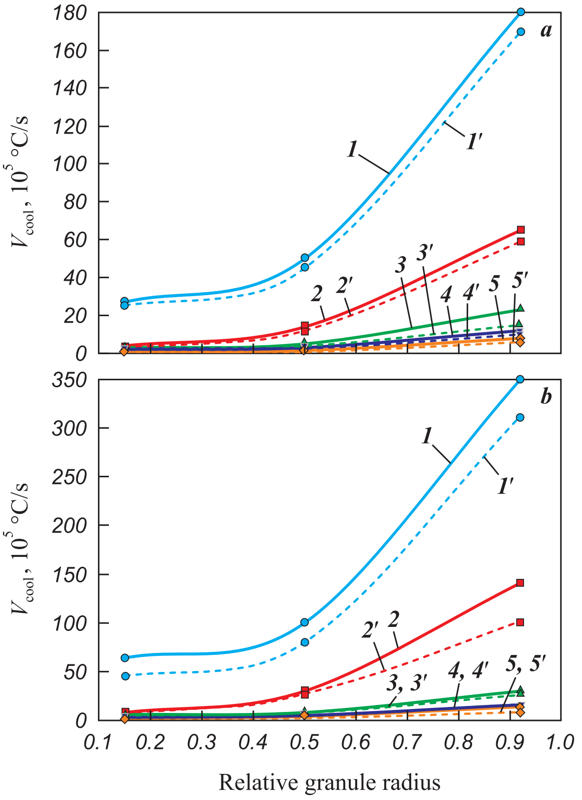

Fig. 7. Cooling rate of granules in nitrogen (***a***) and helium (***b***), determined through graphical analysis, as a function of granule size and gas flow rate
d, μm = 50 (***1, 1′***), 100 (***2, 2′***), 200 (***3, 3′***), 300 (***4, 4′***), 400 (***5, 5′***)
V_g, m/s = 650 (***1–5***), 300 (***1′–5′***)

Рис. 7. Скорость охлаждения гранул в азоте (***а***) и гелии (***b***), рассчитанная графоаналитическим методом, в зависимости от размера гранул и скорости газового потока
d, мкм = 50 (***1, 1′***), 100 (***2, 2′***), 200 (***3, 3′***), 300 (***4, 4′***), 400 (***5, 5′***)
$V_г$, м/с = 650 (***1–5***), 300 (***1′–5′***)

The boundary conditions were set as follows:

$$\left(\frac{\partial\theta}{\partial r}\right)_{r=R_g} = -\left(\frac{\alpha}{\lambda}\theta\right)_{r=R_g} \text{ – on the droplet surface;}$$

$$\left(\frac{\partial\theta}{\partial r}\right)_{r=0} = 0 \text{ – in the droplet center.}$$

The initial conditions (at $\tau = 0$): $\theta = T_m - T_{m.p.}$ for $0 < r < R_g$.

The solution to the differential equation was obtained in [5] in the form:

$$\theta = \frac{T_m - T_{m.p.}}{T_m - T_g} = 1 - \sum_{n=1}^{\infty} B_n \exp\left(-\mu_n^2 F_0\right),$$

where $n = 1, 2, 3\ldots$; F_0 is the Fourier number; B_n are the coefficients determined by:

$$B_n = \frac{6\mathrm{Bi}^2}{\mu_n^2\left(\mu_n^2 + \mathrm{Bi}^2 - \mathrm{Bi}\right)};$$

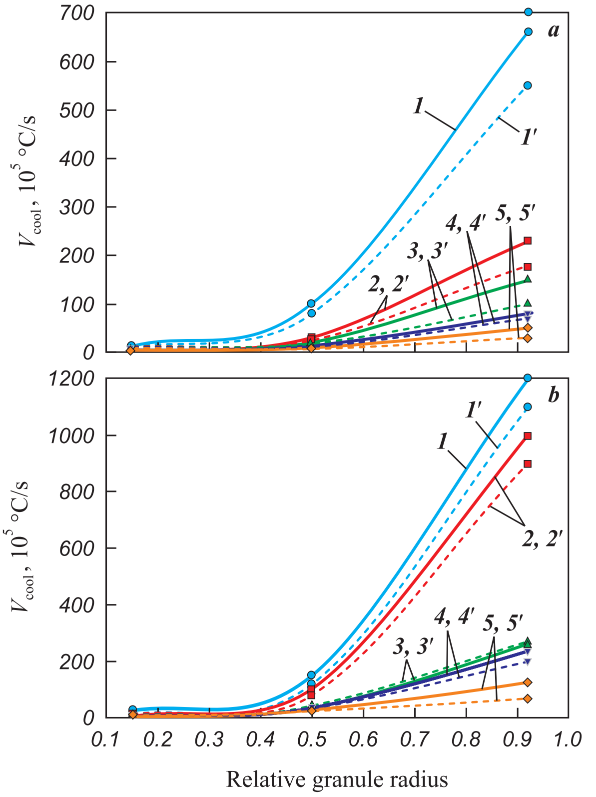

Fig. 8. Cooling rate of granules in nitrogen (***a***) and helium (***b***), analytically calculated as a function of granule size and gas flow rate
d, μm = 50 (***1***, ***1′***), 100 (***2***, ***2′***), 200 (***3***, ***3′***), 300 (***4***, ***4′***), 400 (***5***, ***5′***)
V_g, m/s = 650 (***1***–***5***), 300 (***1′***–***5′***)

Рис. 8. Скорость охлаждения гранул в азоте (***а***) и гелии (***b***), рассчитанная аналитическим методом, в зависимости от размера гранул и скорости газового потока
d, мкм = 50 (***1***, ***1′***), 100 (***2***, ***2′***), 200 (***3***, ***3′***), 300 (***4***, ***4′***), 400 (***5***, ***5′***)
$V_г$, м/с = 650 (***1***–***5***), 300 (***1′***–***5′***)

μ_n are the roots of the characteristic equation:

$$\mathrm{tg}\mu = -\frac{\mu}{\mathrm{Bi} - 1}.$$

The solidification time of melt droplet $\tau = \dfrac{F_0 c_m \rho_T r^2}{\lambda_T}$, where $r = (1 - R^*)R$.

The computed results for the rates of solidification of beryllium droplets using the analytical method are presented in Fig. 8.

Result and discussion

An analysis of the dependencies obtained through the two methods reveals that as the granule diameter increases from 50 to 400 μm, the solidification rate near the droplet's surface decreases from values on the order of 10^7 to 10^5 °C/s. Additionally, an increase in the thermal conductivity of the gas results in a 2–3 times increase in this rate (Figs. 7 and 8). It is worth noting that data regarding the cooling rates of droplets by nitrogen and helium, as determined by these two different methods, exhibit reasonably good agreement, despite some quantitative differences.

Experiments involving the atomization of beryllium granules with nitrogen have revealed that granules measuring 300 μm in size possess a removable "shell" of approximately 10 μm thickness ($R^* = 0.92$). Expanding on the previously mentioned hypothesis, plotting this experimental data on the graph (refer to Fig. 7, *a*) facilitates the determination of the cooling rate at which beryllium solidification through the glass transition mechanism takes place. This rate is approximately 10^6 °C/s when nitrogen exits the nozzle at velocities ranging from 300 to 650 m/s. These determined rates closely resemble those associated with the glass transition of certain metals [12; 13]. Further scrutiny of the graphical data (as observed in Fig. 7, *a*) permits the creation of a curve depicting the thickness of the "shell" enveloping the granules as a function of granule size and the flow rate of the dispersing energy-carrying gas (Fig. 9).

The acquired experimental and analytical results align well with the hypothesis of a "glass-crystalline" mechanism governing the solidification of beryllium granules, which results in their stratification along the interphase boundary. When beryllium melt is atomized with nitrogen, granules smaller than 100 μm solidify through the glass transition mechanism (amorphized), while those with diameters exceeding 300 μm solidify via the crystallization mechanism. Granules ranging in size from 100 to 300 μm undergo a mixed solidification mechanism, leading to the peeling of the "shell" on the surface during the transition from the glass transition mechanism

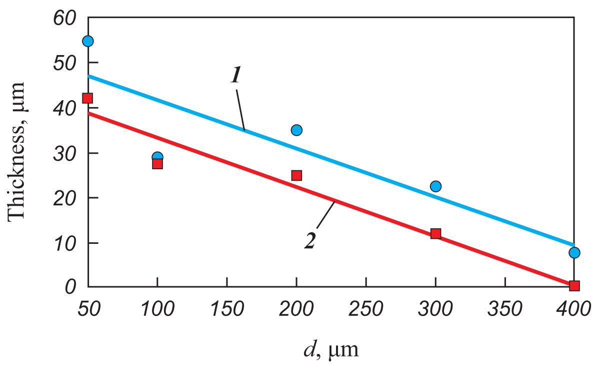

Fig. 9. The thickness of the surface shell in relation to the size of beryllium granules and the flow rate of nitrogen (energy-carrying gas) V_g = 650 m/s (*1*) and 300 m/s (*2*)

Рис. 9. Зависимость толщины поверхностной оболочки (скорлупы) от размера гранул бериллия и скорости подачи азота – газа-энергоносителя $V_г$ = 650 м/с (*1*) и 300 м/с (*2*)

to the crystallization mechanism. The thickness of this "shell" varies based on the granule diameter, measuring 10–15 µm (d = 300 µm) and 20–25 µm (d = 100 µm). During the cooling process of the fine fraction <100 µm and the "shell," the amorphous structure undergoes a transformation into a crystalline one. Understanding this studied effect may hold practical significance.

It is worth noting that the surface of beryllium granules, including the "shell," becomes enriched with nitrogen and oxygen during nitrogen atomization. This enrichment results in an increased impurity content at the boundaries of compacted beryllium derived from these granules. The presence of impurities at grain boundaries negatively affects several vital physical and mechanical properties, such as high-temperature plasticity, stress relaxation capacity, foil vacuum density, and others.

In order to produce a grade of beryllium with reduced impurity content along the grain boundaries and enhanced physical and mechanical properties, it is essential, during the classification phase, to separate a fraction of spherical powders with a "shell" ranging from +100 to 300 µm in size. Subsequently, this "shell" should be removed (peeled) without grinding, using established methods such as a shock-centrifugal mill under specific operating conditions. The resulting granules can then be utilized for the subsequent consolidation into workpieces intended for the production of reactor reflectors–moderators and rolling of foils.

Summarizing the outcomes from our prior works [7–9] and considering the distinct requirements for various beryllium grades (demanding high precision elastic limits for instrument grade, lower relaxation resistance, and vacuum tightness for reactor and foil grades), we propose a technological flowchart for

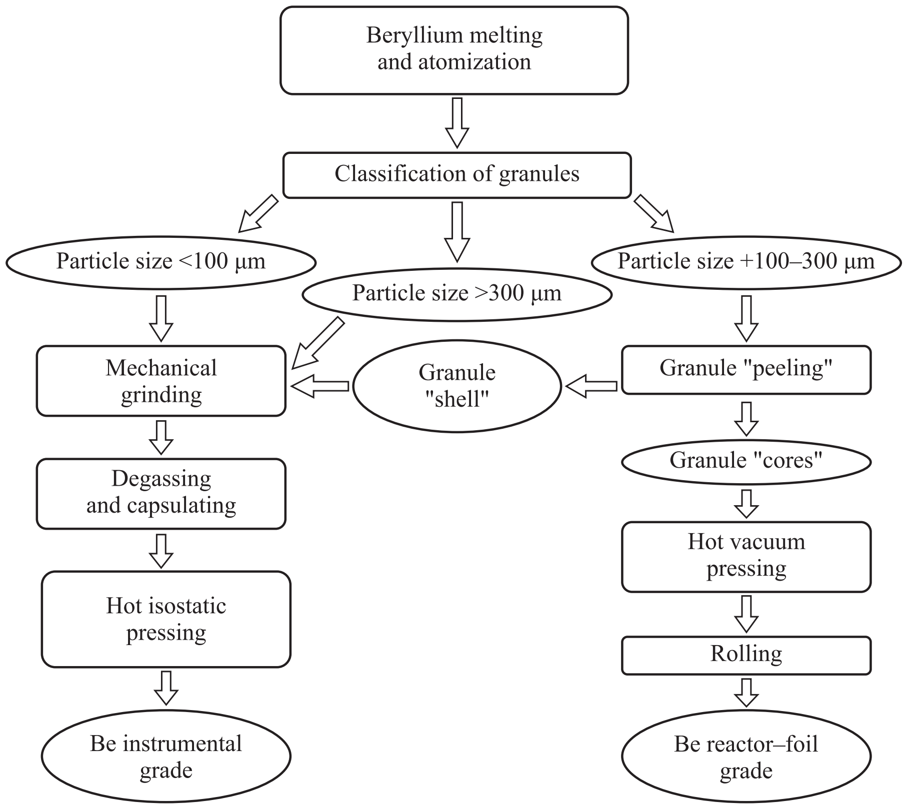

Fig. 10. Flowchart of production process for different structural grades of sintered beryllium

Рис. 10. Технологическая схема получения различных конструкционных сортов спеченного бериллия the production of sintered beryllium varieties tailored for diverse applications (Fig. 10). After the melt atomization, the granules are categorized into three fractions: those below 100 μm (amorphous), those exceeding 300 μm (crystalline), and those ranging from +100 to 300 μm (with a shell). Subsequently, the +100–300 μm fraction is subjected to a "peeling" process, resulting in the production of foil reactor grade material through hot pressing. The remaining fractions (–100 μm, +300 μm and "shell"), post-peeling, are directed toward the manufacturing of an instrument-grade product, which contains a higher concentration of beryllium oxide, serving as a reinforcing hardening phase.

Conclusions

1. The formation mechanism of the surface shell on granules during gas atomization of beryllium melt, resulting from the "amorphous-crystalline" solidification of the melt droplets, has been substantiated.

2. The thickness of the surface shell has been determined as a function of the dispersing gas supply rate and granule size.

3. A technological layout for granule processing at the production of beryllium for various applications has been proposed.

References / Список литературы

1. Webster D. The effect of low melting phases on the elevated temperature microstructural stability of hot pressed beryllium. *Metallurgical and Materials Transactions A*. 1975;6(4):803–808.

2. Papirov I.I., Tikhinskii G.F. Physical metal science of beryllium. Moscow: Atomizdat, 1968. 451p. (In Russ.).

Папиров И.И., Тихинский Г.Ф. Физическое металловедение бериллия. М.: Атомиздат, 1968. 451 с.

3. Davydov D.A., Kholopova O.V., Kolbasov B.N. Inflammation and oxidation characteristics of beryllium: ITER final report. TA. No. ITA-81-06 Be Dust Explosion, July 2005.

4. Davydov D.A., Kholopova O.V., Kolbasov B.N. Formation and degradation of oxide films on beryllium. *Voprosy atomnoi nauki i tekhniki. Ser.: Termoyadernyi sintez*. 2010;(2):39–48. (In Russ.).

Давыдов Д.А., Холопова О.В., Колбасов Б.Н. Образование и деградация оксидных пленок на бериллии. *Вопросы атомной науки и техники. Сер.: Термоядерный синтез*. 2010;(2):39–48.

5. Nikolaenko A.A., Tuzov Yu.V. The effect of grain boundary oxide inclusions on the mechanical properties of hot-pressed beryllium. *Voprosy atomnoi nauki i tekhniki. Ser. Termoyadernyi sintez*. 2012;(2):52—59. (In Russ.).

Николаенко А.А., Тузов Ю.В. Влияние зернограничных включений оксида на механические свойства горячепрессованного бериллия. *Вопросы атомной науки и техники. Сер. Термоядерный синтез*. 2012;(2):52–59.

6. Taylor N., Baker D., Cattaglia S. Key issues in the safety and licensing of ITER. In: *IAEA, 3rd TM ''First generation of fusion power plants: Design and technology''* (Vienna, Austria, 13–15 July 2009); 9th TM "Fusion power plant safety" (Vienna, Austria, 15–17 July 2009). CD-ROM proc., Thursday-2009-07-16.

7. Revutskiy A.V., Syrnev B.V., Lopatin V.Yu., Semilutskaya O.V., Segeda T.A. Study of reinforcing phase formation at the grain boundaries of sintered beryllium. *Russian Journal of Non-Ferrous Metals*. 2021;62(1):125–131. https://doi.org/10.3103/S1067821221010132

Ревуцкий А.В., Сырнев Б.В., Лопатин В.Ю., Семилуцкая О.В., Сегеда Т.А. Исследование формирования упрочняющей фазы на границах зерен спеченного бериллия. *Известия вузов. Порошковая металлургия и функциональные покрытия*. 2020;(3):25–33. https://doi.org/10.17073/1997-308X-2020-3-25-33

8. Revutskiy A.V., Syrnev B.V., Semilutskaya O.V. Study on hardening potential of isostatic pressed beryllium. *Key Engineering Materials*. 2020;842:199–204. https://doi.org/10.4028/www.scientific.net/KEM.842.199

9. Revutsky A.V., Syrnev B.V., Semilutskaya O.V. Study of beryllium hardening obtained by powder metallurgy. *Vestnik Karagandinskogo Universiteta. Ser. Fizika*. 2021;2(102):40–49. https://doi.org/10.31489/2021Ph2/40-49

10. Webster D., Crooks D.D. Creep mechanisms in beryllium. *Metallurgical and Materials Transactions*. 1976;(7A): 1307–1315.

11. Crawford R.F., Burns A.B. Strength efficiency and design data for beryllium structures ASD. *Technical Report 61.692 US AIR Force*. Ohio. 1962.

12. Cai Y., Wu S., Xu R., Yu J. Pressure-induced phase transition and its atomistic mechanism in BeO: A theoretical calculation. *Physical Review. Letters*. 2006;73(18):184104. https://doi.org/10.1103/PhysRevB.73.184104

13. Sebahaddin A., Murat D. Pressure-induced phase transition of BeO. *Solid State Communications*. 2009; 149(9-10):345–348.

14. Weisz M., Mollen J., Voron J. Possibility of the appearance of a liquid phase at 430 °C in commercial beryllium. *Journal of Nuclear Materials*. 1963;(10):56–59.

15. Turner G.I., Lane R.A. The effect of powder particle size on the mechanical properties of hot pressed P1 beryllium. In: *Beryllium*: Proc. Conf. (London, October, 1977). P. 1–15.

16. Webster D., Crooks D.D., Vidoz A.E. The effect of oxide dispersion on the recrystallization of beryllium. *Metallurgical and Materials Transactions*. 1974;4(12):2841–2847.

17. Tuzov Yu.V., Gorokhov V.A., Pakhomov Ya.D., Pronin V.N. Beryllium – material of nuclear and thermonuclear technology. *Voprosy atomnoi nauki i tekhniki. Ser. Termoyadernyi sintez*. 2009;(2):124–127. (In Russ.).

Тузов Ю.В., Горохов В.А., Пахомов Я.Д., Пронин В.Н. Бериллий – материал ядерной и термоядерной техники. *Вопросы атомной науки и техники. Сер. Термоядерный синтез*. 2009;(2):124–127.

18. Markushkin Yu.E., Gorlevskiy V.V., Zabrodin A.V., Tuzov Yu.V. Beryllium for X-ray technology – new possibilities of nanocrystalline material. *Voprosy atomnoi* *nauki i tekhniki. Ser. Materialovedenie i novye materialy*. 2012;(1):130–136. (In Russ.).

Маркушкин Ю.Е., Горлевский В.В., Забродин А.В., Тузов Ю.В. Бериллий для рентгеновской техники – новые возможности нанокристаллического материала. *Вопросы атомной науки и техники. Сер. Материаловедение и новые материалы*. 2012;(1):130–136.

19. Silaev A.F., Fishman V.D. Dispersion of liquid metals and alloys. Moscow: Khimiya, 1983. 144 p. (In Russ.).

Силаев А.Ф., Фишман В.Д. Диспергирование жидких металлов и сплавов. М.: Химия, 1983. 144 с.

20. Metal Glass. Eds. J.J. Gidman, H.J. Limi. Moscow: Metallurgiya, 1984. 264 p. (In Russ.).

Металлические стекла. Под ред. Дж.Дж. Гидмана и Х.Дж. Лими. М.: Металлургия, 1984. 264 с.

21. Kazakova E.A. Granulation and cooling of nitrogen-containing fertilizers. Moscow: Khimiya, 1980. 289 p. (In Russ.).

Казакова Е.А. Гранулирование и охлаждение азотсодержащих удобрений. М.: Химия, 1980. 289 с.

22. Лыков А.В. Теория теплопроводности. М.: Высшая школа, 1967. 600 с.
Lykov A.V. Theory of thermal conductivity. Moscow: Vysshaya shkola, 1967. 600 p. (In Russ.).

Лыков А.В. Теория теплопроводности. М.: Высшая школа, 1967. 600 с.

Information about the Authors

Boris V. Syrnev – Dr. Sci. (Eng.), Leading Researcher of the Scientific Center "Veritas" of the East Kazakhstan Technical University (EKTU)
ORCID: 0000-0002-3085-3341
E-mail: izusan@mail.ru

Galina S. Pestova – Cand. Sci. (Eng.), Leading Design Engineer of the Scientific Center "Veritas", EKTU
ORCID: 0000-0001-6482-5106
E-mail: g_pestova@inbox.ru

Oksana V. Semilutskaya – Senior Lecturer of the School "Metallurgy and mineral processing", EKTU
ORCID: 0000-0001-9494-9572
E-mail: 2009genius@mail.ru

Farit S. Tuganbaev – Leading Process Engineer of the Scientific Center "Veritas", EKTU
ORCID: 0000-0003-2241-555X
E-mail: 24aprel1946@mail.ru

Сведения об авторах

Борис Владимирович Сырнев – д.т.н., вед. науч. сотрудник научного центра «Веритас» Восточно-Казахстанского технического университета (ВКТУ)
ORCID: 0000-0002-3085-3341
E-mail: izusan@mail.ru

Галина Сергеевна Пестова – к.т.н., вед. инженер-конструктор научного центра «Веритас», ВКТУ
ORCID: 0000-0001-6482-5106
E-mail: g_pestova@inbox.ru

Оксана Валерьевна Семилуцкая – ст. преподаватель школы «Металлургия и обогащение полезных ископаемых», ВКТУ
ORCID: 0000-0001-9494-9572
E-mail: 2009genius@mail.ru

Фарит Сапаргалиевич Туганбаев – вед. инженер-технолог научного центра «Веритас», ВКТУ
ORCID: 0000-0003-2241-555X
E-mail: 24aprel1946@mail.ru

Contribution of the Authors

B. V. Syrnev – scientific supervision, goal formulation, participation in experiments, data analysis, development of the technological layout, manuscript writing.
G. S. Pestova – calculations, numerical studies, and discussion of results.
O. V. Semilutskaya – data analysis, discussion of results, manuscript writing (section), development of the technological layout.
F. S. Tuganbaev – organization and execution of experimental work, discussion of results.

Вклад авторов

Б. В. Сырнев – научное руководство, постановка задач, участие в экспериментах, обработка результатов, обоснование технологической схемы, оформление статьи.
Г. С. Пестова – расчеты, численные исследования, обсуждение результатов.
О. В. Семилуцкая – обработка результатов, обсуждение результатов, написание раздела статьи.
Ф. С. Туганбаев – организация и проведение экспериментальных работ, обсуждение результатов, обоснование технологической схемы.

Received 13.10.2022
Revised 12.06.2023
Accepted 15.06.2023

Статья поступила 13.10.2022 г.
Доработана 12.06.2023 г.
Принята к публикации 15.06.2023 г.

Refractory, Ceramic and Composite Materials
Тугоплавкие, керамические и композиционные материалы

UDC 621.762

https://doi.org/10.17073/1997-308X-2023-4-25-33

Research article
Научная статья

Multicriteria optimization of mechanical processing for Pb–C composite charge material

A. N. Vasiliev, **S. N. Sergeenko**

Platov South Russian State Polytechnic University (NPI)
132 Prosveshcheniya Str., Novocherkassk, Rostov Region 346428, Russia

sasha_vasilev55@mail.ru

Abstract. This study investigates a two-stage processing approach for a charge of Pb–C composite powder material composed of lead (PS1) and graphite (GISM) powders in a high-energy mill under ambient air conditions. The study aims to determine the influence of graphite content (C_g) and mechanical activation time (τ) on the particle size distribution of the charge. The results indicate that the particle size distribution can be effectively described using the Rosin–Rammler equation. Furthermore, a correlation between the equation's parameters and the quality of the resulting hot compacted materials, as well as an index derived from the generalized desirability function, has been identified. The study delves into the mechanism behind the formation of the Pb–C powder charge during mechanical activation, which involves the creation of loosely bound agglomerates of composite particles. These agglomerates can be easily disrupted during manual processing of the charge in a mortar. Notably, the research reveals that the extremum of the particle size distribution shifts towards smaller average sizes of the Pb–C composite particles that constitute the agglomerates. The size of these formed agglomerates is shown to depend on both the graphite content in the charge and the duration of mechanical processing. Using multicriteria optimization, the study identifies the optimal values for technological factors ($\tau = 1.8$ ks, $C_g = 0.15$ wt. %) for charge preparation in the two-stage mechanical processing mode. These optimal values result in an enhanced set of physical and mechanical properties for the Pb–C hot-compacted composite material, including shear strength ($\sigma_{\text{shear}} = 6.3$ MPa), hardness ($HRR = 109$), and electrical conductivity ($L = 1.812\ \Omega^{-1}$) of Pb–C. *X*-ray diffraction analysis conducted during the study reveals the formation of lead oxides during the mechanical activation of the Pb–C charge. Additionally, it indicates an increase in the half-width of the diffraction profile of lines (111) and (222), which subsequently decreases after the hot-compaction process. Comparative data involving the use of lead-based chip waste and lead powder-based composites are also presented in the study. These data suggest that a lower optimum graphite content is required for lead powder PS1 ($C_g = 0.15$ wt. %) compared to chip waste ($C_g = 0.5$ wt. %).

Keywords: mechanical activation, lead powder, graphite powder, composite material, electrode mesh, multicriteria optimization, mechanical processing

Acknowledgements: This work received support from the Innovation Promotion Fund under the project titled Development of production technology of Pb–C composite powdered material of electrode mesh of lead acid battery.

For citation: Vasiliev A.N., Sergeenko S.N. Multicriteria optimization of mechanical processing for Pb–C composite charge material. *Powder Metallurgy and Functional Coatings*. 2023;17(4):25–33. https://doi.org/10.17073/1997-308X-2023-4-25-33

Многокритериальная оптимизация механической обработки шихты композиционного материала Pb–C

А. Н. Васильев, **С. Н. Сергеенко**

Южно-Российский государственный политехнический университет им. М.И. Платова (НПИ)
Россия, 346428, Ростовская обл., г. Новочеркасск, ул. Просвещения, 132

sasha_vasilev55@mail.ru

Аннотация. Изучена двухэтапная обработка в высокоэнергетической мельнице в воздушной среде шихты композиционного порошкового материала Pb–C на основе порошков свинца (ПС1) и графита (ГИСМ). Установлено влияние содержания графита ($C_г$) и времени механоактивации (τ) на гранулометрический состав шихты. Показано, что распределение частиц по размерам может быть описано уравнением Розина–Раммлера. Выявлена взаимосвязь между значениями параметров этого уравнения и уровнем качества получаемых горячепрессованных материалов, а также величиной показателя, оцениваемого значениями обобщенной функции желательности. Рассмотрен механизм формирования порошковой шихты Pb–C в процессе механоактивации, связанный с образованием малосвязанных агломератов композиционных частиц, легко разрушающихся при ручной обработке шихты в ступке. Установлено, что экстремум функции распределения частиц по размерам смещается в область меньших значений средних размеров композиционных частиц Pb–C, составляющих агломераты. Выявлено, что размер образованных агломератов зависит от содержания графита в шихте и времени механической обработки. На основе многокритериальной оптимизации определены оптимальные значения технологических факторов ($\tau = 1{,}8$ кс, $C_г = 0{,}15$ мас. %) приготовления шихты, полученной в режиме двухэтапной механической обработки, обеспечивающие повышенный комплекс физико-механических свойств (прочность на срез $\sigma_{ср} = 6{,}3$ МПа, твердость $HRR = 109$, электропроводность $L = 1{,}812$ Ом$^{-1}$) горячепрессованного композиционного материала Pb–C. В результате рентгеноструктурного анализа выявлено формирование оксидов свинца в процессе механоактивации шихты Pb–C, а также увеличение полуширины дифракционного профиля линий (111) и (222) и последующее ее снижение после операции горячего прессования. Получены сравнительные данные применения стружковых отходов на основе свинца и композиционных материалов на основе порошка свинца, свидетельствующие о более низком оптимальном содержании графита в случае использования порошка свинца ПС1 ($C_г = 0{,}15$ мас. %), чем стружковых отходов ($C_г = 0{,}5$ мас. %).

Ключевые слова: механическая активация, порошок свинца, порошок графита, композиционный материал, сетка электрода, многокритериальная оптимизация, механическая обработка

Благодарности: Исследования проведены в рамках проекта «Разработка технологии получения композиционного порошкового материала Pb–C сетки электрода свинцово-кислотного аккумулятора», реализуемого при поддержке Фонда содействия инновациям.

Для цитирования: Васильев А.Н., Сергеенко С.Н. Многокритериальная оптимизация механической обработки шихты композиционного материала Pb–C. *Известия вузов. Порошковая металлургия и функциональные покрытия*. 2023;17(4):25–33.
https://doi.org/10.17073/1997-308X-2023-4-25-33

Introduction

When producing powder composite materials (CM) based on mechanically activated mixtures, sintering, and hot compaction technologies are employed. The mechanical properties of powder materials are dependent on the technological parameters of mechanical activation (MA) [1] of the charge in high-energy mills. Previous studies have established a relationship between the particle size distribution and the chemical composition of the charge, as well as the structure and properties of the powder material, and the results of cold compacting (CC) and hot compacting (HC) [2].

At Platov South-Russian State Polytechnic University (NPI), research has been conducted on the mechanical activation [1–3] of various powder mixtures in dry and liquid media (Fe–Al, Al–Si, Al–C, Fe–Mn, BrAZh, and D-16 shavings, as well as Pb shavings with the addition of graphite). During the MA of a powder charge, multi-stage processes of dispersion and agglomeration are observed, leading to the formation of composite particles with structural heredity. These processes affect the activation of compaction during sintering and the subsequent hot additional compaction of workpieces [1–4]. The kinetics of dispersion and agglomeration depend on the MA modes and the composition of the charge. The use of liquid media and the introduction of graphite prevent the formation of agglomerates due to the formation of an interparticle interface [3–7]. Preliminary studies [3] revealed that when graphite is introduced into the charge in excess of 0.5 wt. % and subsequent hot compaction of the material, cracks occur in the powder material.

For the production of electrodes for lead-acid batteries, lead-based CMs with the addition of graphite, as well as various carbon-containing additives (carbon nanotubes, fullerene black, graphene, activated carbon, etc.) are employed [8–20]. Pb–C composite material has also found applications in lithium-ion batteries [20]. The conducted studies have shown that the maximum amount of graphite in CM should not exceed 1 wt. % with an optimum content ranging from 0.2 to 0.5 wt. % [12; 14; 17; 18]. Graphite content above 1 wt. % leads to deterioration of the rheological properties of the active material paste. The introduction of graphite improves the electrical conductivity, mechanical properties, and chemical efficiency of the Pb–C composite material. Modifying the composition of CM with graphite, unlike other components, is characterized by a lower cost and increased safety [20].

The objective of this study is to perform multicriteria optimization of the graphite content in the charge and processing time, with the goal of achieving an improved set of physical and mechanical properties for hot-compacted Pb–C composite material.

Experimental

Lead powders PS1 (Specifications TU 48-6-123-91) (Fig. 1) and artificial special low-ash graphite (GISM, State Standard GOST 18191-78) were utilized as the initial materials. The two-stage technology for preparing the charge [1–4], carried out in a SAND-1 planetary ball mill (Armenia), involved mixing ($\tau = 1.2$ ks, $n = 150$ s^{-1}) followed by subsequent mechanical activation ($\tau = 0.6 \div 3.6$ ks, $n = 290$ s^{-1}). The design of experiments and the obtained results are presented in Table 1. The process layout for obtaining hot-compacted samples included preliminary cold compaction (500 MPa) of the charge, followed by heating in a furnace ($T = 473$ K, $\tau = 0.3$ ks) in an ambient air and dynamic hot compaction with extrusion elements ($W = 36.6$ MJ/m^3) [4].

The particle size distribution of the activated charges (in accordance with State Standard GOST 18318-94) was determined both before and after manual processing

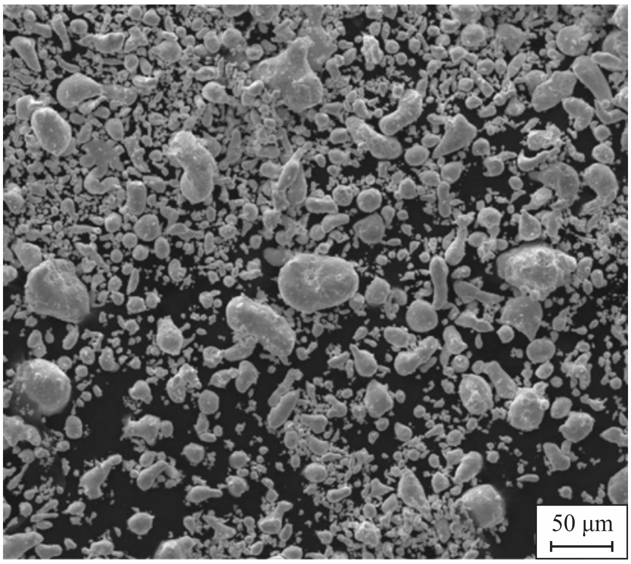

Fig. 1. SEM image of as delivered PS1 lead powder

Рис. 1. РЭМ-изображение порошка свинца ПС1 в состоянии поставки

Table 1. **Design of experiments and results**

Таблица 1. **План проведения и результаты эксперимента**

C_g, wt. %	τ, ks	d_0, µm	d_1, µm	AGI	α_0	β_0	α_1	β_1	r_0^2/r_1^2	Remark
0.15	0.6	64	41	1.56	0.184	0.54	0.394	0.442	0.826/0.935	*
0.85		88	47	1.87	0.162	0.52	0.194	0.576	0.817/0.877	*
0.15	3.0	127	94	1.35	0.615	0.99	0.013	1.038	0.941/0.939	
0.85		221	141	1.57	0.003	1.11	0.008	1.072	0.847/0.891	*
0	1.8	101	93	1.09	0.015	1.01	0.013	1.069	0.972/0.950	*
1.00		140	54	2.59	0.027	0.81	0.196	0.554	0.891/0.940	*
0.50	0	23	22	1.05	2.467	0.15	0.942	0.413	0.699/0.914	
	3.6	165	134	1.23	0.002	1.34	0.004	1.232	0.943/0.922	
	1.8	107	92	1.16	0.002	1.42	0.027	0.892	0.942/0.939	
0.15	1.8	141	111	1.27	0.001	1.59	0.013	1.002	0.839/0.935	
0.85		148	65	2.28	0.020	0.86	0.149	0.576	0.855/0.918	*
0.50	0.6	114	67	1.70	0.138	0.51	0.173	0.542	0.819/0.899	*
	3.0	122	102	1.20	0.012	1.00	0.010	1.096	0.927/0.924	*
0	0	20	–	–	0.154	0.88	–	–	0.730/–	

* Formation of cracks on external surface of a sample.

in a mortar. This analysis was conducted using a sieve analyzer, model 029 (OOO Litmashpribor, Usman). Additionally, the hardness *HRR* (according to State Standard GOST 24622-91) of the hot-compacted composite powder material was studied using a TR 2140 device (OOO ASMA-Pribor, Svetlovodsk, Ukraine). The shear strength (δ_{shear}) of the extruded element ($d_{\text{ee}} = 3.1$ mm) was determined using a UMM-5 universal machine (OOO "ASMA-Pribor", Svetlovodsk, Ukraine). All measurements of physical, mechanical, and operational properties were carried out in comparison with a lead-based cast sample, which had a hardness of $HRR = 60 \div 70$. Electrical conductivity measurements were conducted in accordance with State Standards GOST 24606.3-82 and 4668-75 ($U = 50$ mV, $I = 10$ mA) using equipment developed at YuRGPU (NPI) [21], with a load of 30 ± 1 N.

To describe the particle size distribution of charge, the Rosin-Rammler function reduced to linear form was employed [1; 22], allowing for the determination of parameters α and β as follows:

$$y = a + bx, \tag{1}$$

where $y = \ln(\ln B^{-1})$; $a = \ln\alpha$; $b = \beta$; $x = \ln X$; B represents the content of sieved Pb–C charge, wt. %; X stands for the particle size.

Additional grinding in a mortar was carried out to assess the degree of agglomeration of charge particles during the MA. This is characterized by the agglomeration index (AGI) [23], calculated as the ratio of the average particle sizes of the activated (d_0) and mortar-processed (d_1) charge:

$$\text{AGI} = d_0/d_1. \tag{2}$$

The morphology and spectral analysis of Pb–C charge particles were investigated using a "Quanta 200" scanning electron microscope (FEI Company, USA) at the Nanotechnologies Resource Sharing Center of Southern Russian State Pedagogical University (NPI). Additionally, thermogravimetric analysis in a helium atmosphere was conducted using an STA 449C synchronous thermal analyzer (NETZSCH, Germany).

Table 1 summarizes the following parameters: C_g represents the graphite content in the charge, wt. %; τ is the time of mechanical activation, ks; d_0 indicates the average particle size of the charge after activation, μm; d_1 signifies the average particle size of the blend after manual processing in a mortar, μm; α_0, β_0 and α_1, β_1 denote the parameters of the Rosin–Rammler equation for the charge, respectively, after mechanical activation and manual processing in a mortar; r_0^2, r_1^2 represent the determination coefficients of the Rosin–Rammler equation for the charge after mechanical activation and subsequent manual processing in a mortar, respectively.

As shown in Figure 2, a range of technological parameters has been identified that ensures the production of Pb–C composite powder material without visible cracks and with cracks on the edge surface of a sample.

Specifically, avoiding cracks is achieved by increasing the MA time of the charge to more than 1.8 ks and maintaining the graphite content in the charge at less than 0.5 wt. %. This combination of parameters results in the formation of hot-compacted material with a smooth surface, both on the sides and edges. Additionally, achieving a similar outcome is possible with $C_g = 0.5$ wt. % and in the absence of MA (τ = 0 ks), i.e., when the mixture is obtained solely through agitation.

At high graphite contents, there is an observable increase in non-metallic inclusions, which in turn reduces the plasticity of the material. Increasing the duration of MA leads to a more uniform distribution of graphite throughout the entire bulk of the charge and eliminates the occurrence of cracks during deformation of the material.

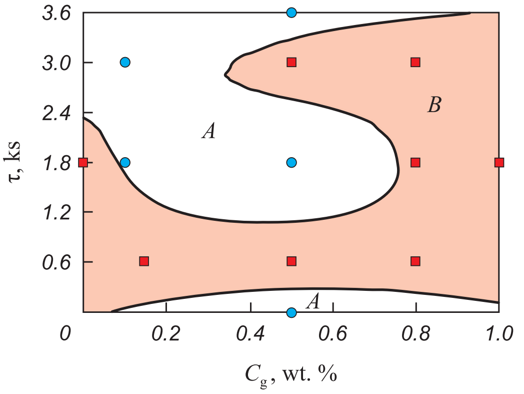

Fig. 2. Ranges of technological parameters ensuring the production of Pb–C material without cracks (***A***) and with cracks (***B***)
● – without cracks, ■ – with cracks

Рис. 2. Области значений технологических параметров, обеспечивающих получение материала Pb–C без трещин (***A***) и с трещинами (***B***)
● – без трещин, ■ – с трещинами

Result and discussion

An analysis of the influence of graphite content in the charge and the duration of mechanical activation has shown that as τ increases, the average particle size of the activated charge (d_0) increases across all studied C_g. Manual processing in a mortar results in the crushing of agglomerates, leading to agglomeration index values (AGI) greater than 1. In this case, the maximum values of d_0 are observed after processing in a planetary mill when both C_g and τare increased. When the graphite con-

Table 2. **Results of multicriteria optimization of technological factors for producing Pb–C composite material**

Таблица 2. **Результаты многокритериальной оптимизации технологических факторов получения композиционного материала Pb–C**

C_g, wt. %	τ, ks	Average particle size of Pb–C charge, μm		Physicomechanical properties of Pb–C HC CM				Desirability function *D*	Quality level
		d_0	d_1	*HRR*	σ_{ahear}, MPa	*P*, %	*L*, Ω^{-1}		
0.15	1.8	141.4	111.4	109	6.3	18.9	1.812	0.81	Excellent
	3.0	126.9	94.3	101	3.8	13.8	0.371	0.67	Acceptable
0.50	1.8	106.8	92.1	87	15.2	24.1	0.142	0.64	Acceptable

tent in the charge is increased to 0.5 wt. % and the treatment duration is extended to 1.8 ks, the dimensions of d_0 stabilize (refer to Table 1). Manual processing contributes to the breakdown of agglomerates across the entire range of studied C_g and τ. Larger average particle sizes, constituting the agglomerates (d_1), are observed when the graphite content in the charge is 0.15 wt. %.

The addition of a higher graphite content (1 wt. %) into the charge results in an increased agglomeration index AGI, defined as the ratio of d_0 to d_1 [1; 2]. When the graphite content in the charge is 0.5 wt. %, and the MA duration is 1.8 ks, it results in the formation of particularly resistant agglomerates ($d_0 \approx d_1$, AGI = 1.16).

An increase in τ to 1.8 ks results an elevated coefficient of determination r_0^2 of the Rosin–Rammler equation when reduced to linear form (1). In this instance, the calculated parameter α_0 decreases. The function $\alpha_0(\tau)$ exhibits an extreme behavior. Following manual processing in a mortar and an extended MA time, there is an observed increase in β_1.

Multicriteria optimization of process variables

In pursuit of multicriterial optimization (MCO) for the technological factors governing mechanical activation (C_g, τ), with the goal of enhancing a comprehensive set of physical and mechanical properties (ultimate shear strength σ_{shear}, hardness *HRR*, electrical conductivity *L*, and porosity *P*) of the Pb–C composite material, a generalized desirability function *D* was determined [3; 24]. This function employs the following scale: *D* = 0.75÷1.0 indicating an excellent level of quality; 0.68÷0.74 representing high quality; 0.6÷0.67 signifying acceptable quality; 0.5÷0.59 denoting sufficient quality; and less than 0.5 reflecting an unacceptable level.

The results of the MCO values for C_g and τ, ensuring the production of high-quality Pb–C composite material, are presented in Table 2, ordered in descending order of *D* values. Analysis of the MCO results has revealed that an excellent level of quality (*D* = 0.81) is achieved with a graphite content in the charge of 0.15 wt. % and a processing time of 1.8 ks. The experimental results and the optimized MA parameters pertain solely to the studied range of graphite contents and processing times in a SAND-1 planetary ball mill.

In order to determine the optimal composition of the composite material (refer to Table 2), *X*-ray phase analysis of the mechanically activated mixture was conducted, and the morphology of its particles was investigated (Fig. 3).

Experimental findings have confirmed the formation of agglomerates during the process of MA in a high-energy mill. These agglomerates are subsequently broken down during grinding in a mortar (Fig. 4). During manual processing in a mortar, a noticeable shift occurs in the extremum of the particle size distribution function toward smaller average sizes of Pb–C composite particles.

Reducing the charge processing time from 3.0 to 1.8 ks results in a decrease in the intensity of the PbO lines due to a lower degree of oxidation of the powder material

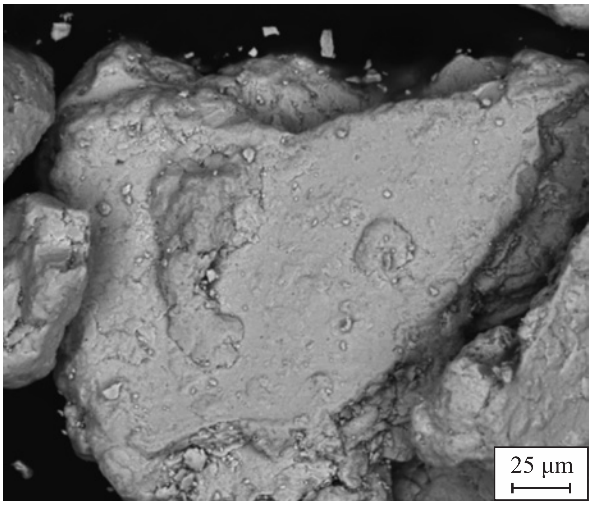

Fig. 3. SEM image of the charge after mechanical activation and manual processing (C_g = 0.15 wt. %, τ = 1.8 ks)

Рис. 3. РЭМ-изображение шихты после процесса механической активации и ручной обработки ($C_г$ = 0,15 мас. %, τ = 1,8 кс)

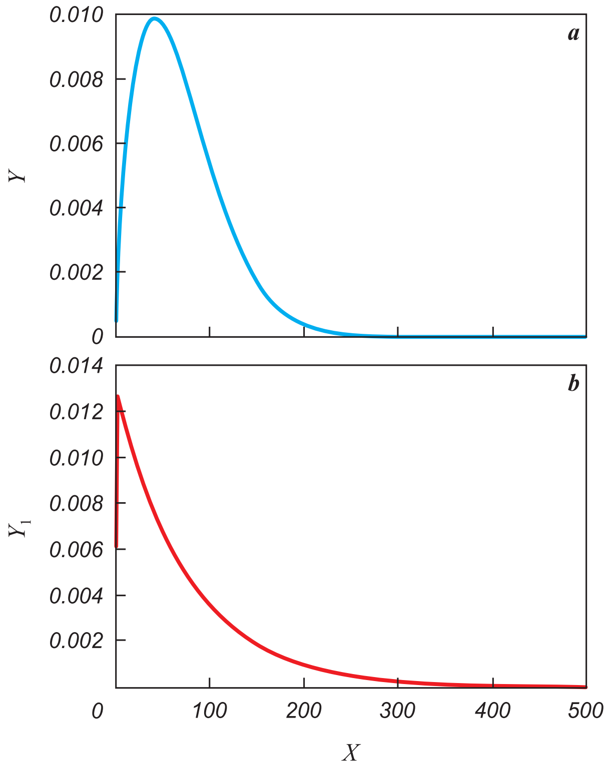

Fig. 4. Particle size distribution, plotted according to the Rosin-Rammler equation, after MA (***a***) and manual processing in a mortar (***b***)
Y(*X*) – differential particle size distribution function (***a***);
$Y_1(X)$ – integral function (***b***)

Рис. 4. Распределение частиц по размерам, построенное по уравнению Розина-Раммлера, после МА (***a***) и ручной обработки в ступке (***b***)
Y(*X*) – дифференциальная функция распределения частиц по размерам (***a***); $Y_1(X)$ – интегральная функция (***b***)

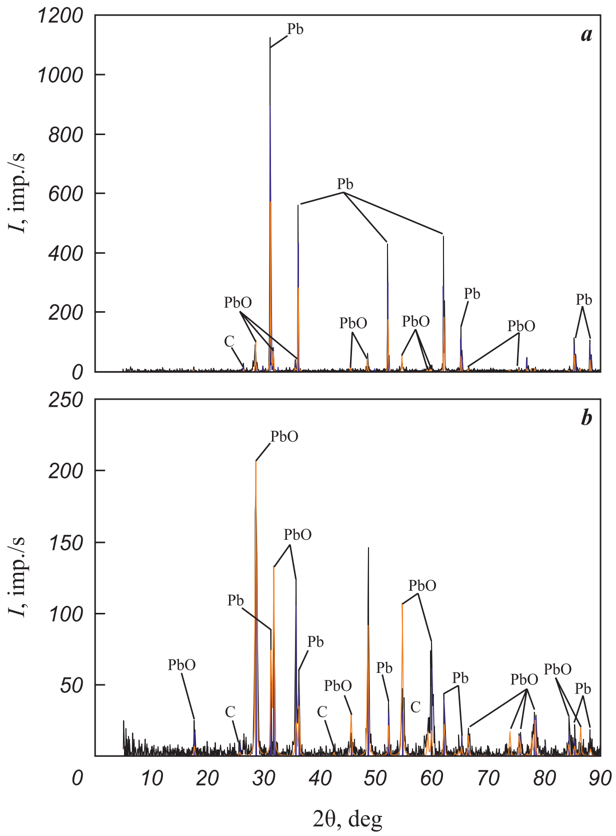

Fig. 5. Diffraction patterns of lead powder in the as-delivered state (***a***) and the charge after mechanical activation and manual processing (***b***)
(C_g = 0.15 wt. %, τ = 1.8 ks)

Рис. 5. Дифрактограммы порошка свинца в состоянии поставки (***a***) и шихты после процесса механической активации и ручной обработки (***b***)
($C_г$ = 0,15 мас. %, τ = 1,8 кс)

(Fig. 5). Increasing the graphite content to 0.5 wt. % with a short processing time (τ = 1.8 ks) enables a reduction in material oxidation during MA.

Analysis of the diffraction pattern revealed that particles within the mechanically activated Pb–C charge contain PbO (Fig. 5). Mechanical activation of the powder charge results in the broadening of the profile of the lines (111) and (222) of lead due to an increase in microstresses and a reduction in the size of the mosaic blocks. Subsequent operations involving short-term heating and HC cause a decrease in the half-width of the diffraction profile of the lines (Table 3).

When substituting lead chips and GK-3 graphite used in [3] with PS-1 and GISM lead powder, the optimal graphite content decreases from 0.5 to 0.15 wt. % at a processing time of 1.8 ks in a high-energy mill.

Figure 6 illustrates the microstructure of the hot-compacted composite powder material (*T* = 473 K, τ = 0.3 ks, medium: air, *W* = 36.6 MJ/m^3) based on Pb–C

Table 3. **Calculated half-widths of the diffraction profile of Pb lines at optimal values of C_g and τ**

Таблица 3. **Расчетные значения полуширины дифракционного профиля линий Pb при оптимальных значениях $C_г$ и τ**

Indices *hkl*	2θ, deg			Half width of diffraction profiles of lines, deg		
	As-delivered powder	After MA	After HC	As-delivered powder	After MA	After HC
111	31.3048	31.3048	31.3829	0.087	0.142	0.096
222	65.2358	65.2358	65.4920	0.094	0.132	0.093

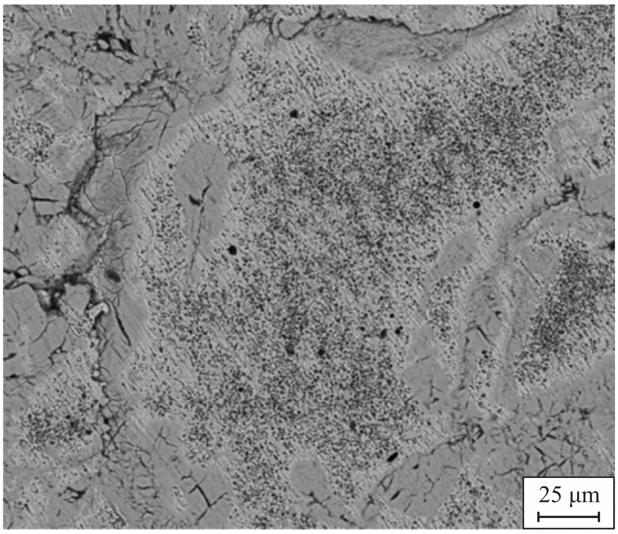

Fig. 6. SEM image of hot-compacted composite powder material

Рис. 6. РЭМ-изображение горячепрессованного композиционного порошкового материала

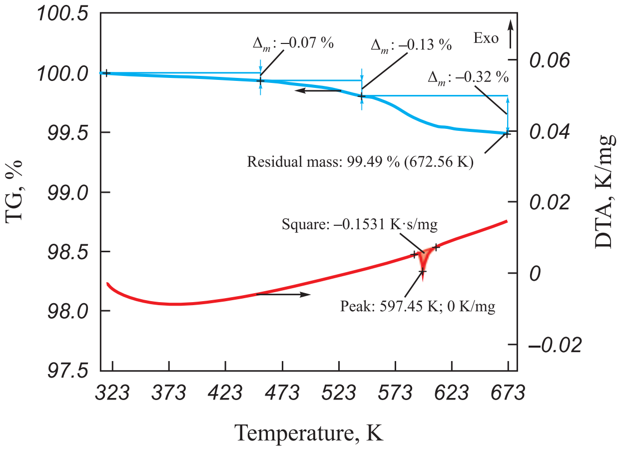

Fig. 7. Thermogravimetric analysis of hot-compacted Pb–C composite powder material

Рис. 7. Термогравиметрический анализ горячепрессованного композиционного порошкового материала Pb–C

charge (C_g = 0.15 wt. %) processed in a high-energy mill (τ = 1.8 ks), resulting in improved physical and mechanical properties, including hardness, strength, electrical conductivity, and porosity. The Pb–C charge (0.15 wt. %) that facilitates the production of hot-compacted material with increased hardness and electrical conductivity is characterized by extreme parameters of the Rosin–Rammler equation ($\alpha_0 = \alpha_{0\min} = 0.001$; $\beta_0 = \beta_{0\max} = 1.59$). Concurrently, the agglomeration index AGI = 1.16 indicates the formation of intractable agglomerates ($d_0 \approx d_1$). Additionally, thermal analysis of the charge material revealed a shift (from 598 to 543 K) in the peak of the melting onset curve of the material compared to PS1 powder in its initial state due to the accumulation of material energy during the mechanical activation process (Fig. 7).

Conclusions

The results of the studies have revealed several important findings. Increasing the duration of mechanical activation to optimal values (τ = 1.8 ks) leads to a higher degree of compliance of the charge's particle size distribution with the Rosin–Rammler equation. The optimal parameters for mechanical activation of the charge ($\tau \sim 1.8$ ks, C_g = 0.15 wt. %), which correspond to the extreme parameters of the Rosin–Rammler equation ($\alpha_0 = \alpha_{0\min} = 0.001$; $\beta_0 = \beta_{0\max} = 1.59$), result in improved values of the generalized desirability functions for the hot-compacted composite powder material (CPM).

Experimental evidence demonstrates that during mechanical processing in a high-energy mill, agglomerates are formed, but these agglomerates are subsequently broken down during manual processing in a mortar. In this scenario, the extremum of the particle size distribution function shifts toward smaller average sizes of the Pb–C composite particles that constitute the agglomerates.

When using the optimal values of technological factors (τ = 1.8 ks, C_g = 0.15 wt. %), the structure of hot-compacted Pb–C CPMs is formed, leading to improved consolidation quality of the composite material. This is characterized by the absence of identifiable interfaces on the interparticle splice surfaces and enhanced mechanical properties (HRR = 109, σ_{shear} = 6.3 MPa) and electrical conductivity (L = 1.812 Ω^{-1}).

Список литературы / References

1. Slabkii D.V., Sergeenko S.N., Popov Yu.V., Saliev A.N. X-ray diffraction analysis of powder materials based on mechanochemically activated D-16 chips with the addition of nickel powder. *Tekhnologii obrabotki materialov*. 2021;19(3):61–67. (In Russ.).
https://doi.org/10.18503/1995-2732-2021-19-3-61-67

Слабкий Д.В., Сергеенко С.Н., Попов Ю.В., Салиев А.Н. Рентгеноструктурный анализ порошковых материалов на основе механохимически активированной стружки Д-16 с добавлением порошка никеля. *Технологии обработки материалов*. 2021;19(3):61–67.
https://doi.org/10.18503/1995-2732-2021-19-3-61-67

2. Sergeenko S.N. Kinetics of dispersion-agglomeration processes during mechanical activation of the charge of 110G13 powder steel. *Chernye Metally*. 2019;(7):47–52. (In Russ.).

Сергеенко С.Н. Кинетика дисперсионно-агломерационных процессов при механоактивации шихты порошковой стали 110Г13. *Черные металлы*. 2019;(7):47–52.

3. Sergeenko S.N., Vasiliev A.N., Yatsenko A.N., Marakhovskii M.A. Multicriteria optimization of obtaining

hot-compacted Pb–C composite materials based on shavings from recycled battery electrodes. *Tsvetnye Metally*. 2020;(11):63–69. (In Russ.).
https://doi.org/10.17580/tsm.2020.11.09

Сергеенко С.Н., Васильев А.Н., Яценко А.Н., Мараховский М.А. Многокритериальная оптимизация получения горячекомпактированных композиционных материалов Pb–C на основе стружки утилизированных электродов аккумуляторных батарей. *Цветные металлы*. 2020;(11):63–69.
https://doi.org/10.17580/tsm.2020.11.09

4. Streletskii A.N., Kolbanev I.V., Borunova A.B., Leonov A.V., Nishchak O.Yu., Permenov D.G., Ivanova O.P. Mechanochemical preparation of highly dispersed MeO/C composites as materials for supercapacitors and ion batteries. *Colloid Journal*. 2021;(83):763–773.
https://doi.org/10.1134/S1061933X21060132
5. Kostikov V.I., Dorofeev Yu.G., Eremeeva Zh.V., Zherditskaya N.N., Ulyanovskii A.P., Sharipzyanova G.Kh. Features of the use of non-traditional carbon-containing components in the technology of powder steels. Message 2. Influence of non-traditional carbon-containing components on sintering processes in powder steel technology. *Izvestiya Vuzov. Powder Metallurgy and Functional Coatings*. 2008;(4):5–8. (In Russ.).

   Костиков В.И., Дорофеев Ю.Г., Еремеева Ж.В., Жердицкая Н.Н., Ульяновский А.П., Шарипзянова Г.Х. Особенности применения нетрадиционных углеродсодержащих компонентов в технологии порошковых сталей. Сообщение 2. Влияние нетрадиционных углеродсодержащих компонентов на процессы спекания в технологии порошковой стали. *Известия вузов. Порошковая металлургия и функциональные покрытия*. 2008;(4):5–8.
6. Shial S.R., Masanta M., Chairab D. Recycling of waste Ti machining chips by planetary milling: Generation of Ti powder and development of in situ TiC reinforced Ti–TiC composite powder mixture. *Powder Technology*. 2018;(15):232–240.
https://doi.org/10.1016/j.powtec.2018.01.080
7. Xiaopeng H., Ying H., Suhua Z., Xu S., Xuanyi P., Xuefang C. Effects of graphene content on thermal and mechanical properties of chromium-coated graphite flakes/Si/Al composites. *Journal of Materials Science: Materials in Electronics*. 2018;(29):4179–4189.
https://doi.org/10.1007/s10854-017-8363-7
8. Jian Gu, Jing Zhong, Kai-da Zhu, Xin-ru Wang, Senlin Wang. In-situ synthesis of novel nanostructured Pb–C composites for improving the performance of lead-acid batteries under high-rate partial-state-of-charge operation. *Journal of Energy Storage*. 2021;(33):102082.
https://doi.org/10.1016/j.est.2020.102082
9. Zhang W., Lin H., Lu H., Liu D., Yin J., Lin Z. On the electrochemical origin of the enhanced charge acceptance of the lead-carbon electrode. *Journal of Materials Chemistry A*. 2015;(3):4399–4404.
https://doi.org/10.1039/C4TA05891G
10. Cheng F., Liang J., Tao Z., Chen J. Functional materials for rechargeable batteries. *Advanced Materials*. 2011;(23): 1695–1715. https://doi.org/10.1002/adma.201003587
11. Marom R., Ziv B., Anerjee A., Cahana B., Luski S., Aurbach D. Enhanced performance of starter lighting ignition type lead-acid batteries with carbon nanotubes as an additive to the active mass. *Journal of Power Sources*. 2015;(296):78–85.
https://doi.org/10.1016/j.jpowsour.2015.07.007
12. Pavlov D., Nikolov P., Rogachev T. Influence of carbons on the structure of the negative active material of lead-acid batteries and on battery performance. *Journal of Power Sources*. 2011;(196):5155–5167.
https://doi.org/10.1016/j.jpowsour.2011.02.014
13. Fernández M., Valenciano J., Trinidad F., Muñoz N. The use of activated carbon and graphite for the development of lead-acid batteries for hybrid vehicle applications. *Journal of Power Sources*. 2010;(195):4458–4469.
https://doi.org/10.1016/j.jpowsour.2009.12.131
14. Zou X., Kang Z., Shu D., Liao Y., Gong Y., He C., Hao J., Zhong Y. Effects of carbon additives on the performance of negative electrode of lead-carbon battery. *Electrochimica Acta*. 2014;(151):89–98.
https://doi.org/10.1016/j.electacta.2014.11.027
15. Kumar S.M., Ambalavanan S., Mayavan S. Effect of graphene and carbon nanotubes on the negative active materials of lead acid batteries operating under high-rate partial-state-of-charge operation. *RSC Advances*. 2014;(4): 36517. https://doi.org/10.1039/C4RA06920J
16. Zhao L., Zhou W., Shao Y., Wang D. Hydrogen evolution behavior of electrochemically active carbon modified with indium and its effects on the cycle performance of valve-regulated lead-acid batteries. *RSC Advances*. 2014;(4): 44152–44157. https://doi.org/10.1039/C4RA04670F
17. Long Q., Ma G., Xu Q., Ma C., Nan J., Li A., Chen H. Improving the cycle life of lead-acid batteries using three-dimensional reduced graphene oxide under the high-rate partial-state-of-charge condition. *Journal of Power Sources*. 2017;(343):188–196.
https://doi.org/10.1016/j.jpowsour.2017.01.056
18. Swogger S.W., Everill P., Dubey D.P., Sugumaran N. Discrete carbon nanotubes increase lead acid battery charge acceptance and performance. *Journal of Power Sources*. 2014;(261):55–63.
https://doi.org/10.1016/j.jpowsour.2014.03.049
19. Sugumaran N., Everill P., Swogger S.W., Dubey D.P. Lead acid battery performance and cycle life increased through addition of discrete carbon nanotubes to both electrodes. *Journal of Power Sources*. 2015;(279):281–293.
https://doi.org/10.1016/j.jpowsour.2014.12.117
20. Li Q., Xu C., Yang L., Pei K., Zhao Y., Liu X., Che R. Pb/C Composite with spherical Pb nanoparticles encapsulated in carbon microspheres as a high-performance anode for lithium-ion batteries. *ACS Applied Energy Materials*. 2020;(3):7416–7426.
https://doi.org/10.1021/acsaem.0c00812
21. Dorofeev Yu.G., Naumenko A.A., Radikainen L.M., Gritsenko S.I., Sergeenko S.N. Measurement of electrical resistivity of sintered products. *Zavodskaya Laboratoriya (Diagnostika Materialov)*. 1995;(8):41–43. (In Russ.).

    Дорофеев Ю.Г., Науменко А.А., Радикайнен Л.М., Гриценко С.И., Сергеенко С.Н. Измерение удельного электрического сопротивления спеченных изделий. *Заводская лаборатория (диагностика материалов)*. 1995;(8):41–43.

22. Khodakov G.S. *Physics of grinding*. Moscow.: Nauka, 1972. 307 p. (In Russ.).

Ходаков Г.С. Физика измельчения. М.: Наука, 1972. 307 с.

23. Dyuzhechkin M.K., Sergeenko S.N., Popov Y.V. Features of structure and property formation for hot-deformed materials of the Al–Si and Al–Si–C systems based on mechanochemically activated charges. *Metallurg*. 2015;(9):86–91. (In Russ.).

Дюжечкин М.К., Сергеенко С.Н., Попов Ю.В. Особенности формирования структуры и свойств горячедеформированных материалов систем Al–Si и Al–Si–C на основе механохимически активированных шихт. *Металлург*. 2015;(9):86–91.

24. Novik F.S. Optimization of metal technology processes by methods of planning experiments. Moscow: Mashinostroenie, 1980. 304 p. (In Russ.).

Новик Ф.С. Оптимизация процессов технологии металлов методами планирования экспериментов. М.: Машиностроение, 1980. 304 с.

Information about the Authors

Aleksandr N. Vasiliev – Postgraduate Student of the Department of Engineering Technology, Technological Machines and Equipment, Platov South Russian State Polytechnical University (NPI)
ORCID: 0000-0002-7172-6090
E-mail: sasha_vasilev55@mail.ru

Sergey N. Sergeenko – Cand. Sci. (Eng.), Associate Prof. of the Department of Engineering Technology, Technological Machines and Equipment, NPI
ORCID: 0000-0002-6718-4591
E-mail: sergeenko@gmail.com

Сведения об авторах

Александр Николаевич Васильев – аспирант кафедры технологии машиностроения, технологических машин и оборудования Южно-Российского государственного политехнического университета им. М.И. Платова (ЮРГПУ (НПИ))
ORCID: 0000-0002-7172-6090
E-mail: sasha_vasilev55@mail.ru

Сергей Николаевич Сергеенко – к.т.н., доцент кафедры технологии машиностроения, технологических машин и оборудования ЮРГПУ (НПИ)
ORCID: 0000-0002-6718-4591
E-mail: sergeenko@gmail.com

Contribution of the Authors

A. N. Vasiliev – formulated the research objectives, conducted experiments, described patterns, authored the manuscript.
S. N. Sergeenko – supervision, described the values of the half-width of the diffraction profile of Pb lines.

Вклад авторов

А. Н. Васильев – определение цели работы, проведение экспериментов, описание закономерностей, написание статьи.
С. Н. Сергеенко – научный руководитель, описание значений полуширины дифракционного профиля линий Pb.

Received 16.10.2022
Revised 13.05.2023
Accepted 17.05.2023

Статья поступила 16.10.2022 г.
Доработана 13.05.2023 г.
Принята к публикации 17.05.2023 г.

Refractory, Ceramic and Composite Materials
Тугоплавкие, керамические и композиционные материалы

UDC 661.66

https://doi.org/10.17073/1997-308X-2023-4-34-40

Research article
Научная статья

Investigation of the properties of high-strength fibers by methods of physico-chemical analysis

E. G. Cheblakova, B. S. Kleusov ✉, V. I. Sapozhnikov, V. A. Gorina, Yu. A. Malinina, A. R. Gareev

Vyatkin R&D Institute of Graphite-Based Structural Materials (JSC "NIIgraphit")
2 Bld. 1, Electrodnaya Str., Moscow 111524, Russia

✉ BSKleusov@rosatom.ru

Abstract. The carbon fiber (CF) of UMT 49-12K-ER grade, manufactured by Alabuga-Volokno LLC (Umatex JSC), was the subject of an extensive study. This investigation encompassed an analysis of its physico-chemical properties. The interplanar dimensions and chemical composition of the CF were determined using *X*-ray diffraction and atomic emission spectroscopy. Surface properties of the CF, including specific surface area and pore size distribution, were investigated through nitrogen adsorption. The BET specific surface area was measured at 0.29 m^2/g. The volume of mesopores and their size distribution were calculated using the Barrett, Joyner, and Halenda method. Additionally, an analysis of surface functional groups was conducted through a back titration method. It was observed that there was no presence of carboxyl, phenolic, or carbonyl groups. The diffraction patterns were processed with a two-component profile description model. The results of atomic emission spectral analysis revealed that silicon compounds were the dominant impurities in the chemical composition of the CF. Further investigations determined that, in an inert environment, the epoxy coupling agent used to enhance the performance properties of this CF undergoes thermal decomposition at temperatures of 300–400 °C. The CF itself does not experience weight loss when heated up to 950 °C. It was also discovered that this CF ignites in the presence of oxygen at temperatures exceeding 550 °C, surpassing the thresholds noted in previous publications for carbon fibers without such specialized additives. The results of this research have suggested new methodologies for studying carbon fibers.

Keywords: carbon fiber, *X*-ray phase structural analysis (XPSA), synchronous thermal analysis (STA), atomic emission spectral analysis (AESA), specific surface area, BET method, functional groups

For citation: Cheblakova E.G., Kleusov B.S., Sapozhnikov V.I., Gorina V.A., Malinina Yu.A., Gareev A.R. Investigation of the properties of high-strength fibers by methods of physico-chemical analysis. *Powder Metallurgy and Functional Coatings*. 2023;17(4): 34–40. https://doi.org/10.17073/1997-308X-2023-4-34-40

Исследования свойств высокопрочных волокон методами физико-химического анализа

Е. Г. Чеблакова, Б. С. Клеусов ✉, В. И. Сапожников, В. А. Горина, Ю. А. Малинина, А. Р. Гареев

Научно-исследовательский институт конструкционных материалов на основе графита им. С.Е. Вяткина (АО «НИИграфит»)
Россия, 111524, г. Москва, ул. Электродная, 2, стр. 1

✉ BSKleusov@rosatom.ru

Аннотация. Проведено исследование углеволокна (УВ) марки UMT 49-12K-EP ООО «Алабуга-Волокно» (АО «Юматекс»). Изучены его физико-химические свойства. С помощью рентгеновской дифракции и атомно-эмиссионной спектроскопии определены межплоскостные размеры и химический состав УВ. Исследования поверхностных свойств углеволокна (удельной поверхности и распределения пор по размерам) проведены по адсорбции азота. Удельная поверхность рассчитана по методу БЭТ и составила 0,29 м^2/г. Объем мезопор и их распределение по размерам рассчитывали по методу Баррета, Джойнера и Халенды. Методом обратного титрования проведен анализ содержания поверхностных функциональных групп. Наличие карбоксильных, фенольных и карбонильных групп не обнаружено. Обработку дифрактограмм осуществляли посредством двухкомпонентной модели описания профиля. По результатам атомно-эмиссионного спектрального анализа установлено, что в примесном химическом составе углеволокна преобладают соединения кремния. Подтверждено, что в инертной среде эпоксидный аппрет, которым пропитано данное УВ для улучшения эксплуатационных свойств, подвергается термической деструкции при температурах 300–400 °С, в то время как само углеволокно не теряет массу при нагревании до 950 °С. Установлено, что данное УВ сгорает на воздухе при температуре свыше 550 °С, что превышает температуру, указанную в литературе для углеродного волокна без специальных добавок. По результатам проведенных исследований предложены методики исследования углеволокна.

Ключевые слова: углеволокно, рентгенофазовый структурный анализ (РФСА), синхронный термический анализ (СТА), атомный эмиссионный спектральный анализ (АЭСА), удельная поверхность, метод БЭТ, функциональные группы

Для цитирования: Чеблакова Е.Г., Клеусов Б.С., Сапожников В.И., Горина В.А., Малинина Ю.А., Гареев А.Р. Исследования свойств высокопрочных волокон методами физико-химического анализа. *Известия вузов. Порошковая металлургия и функциональные покрытия*. 2023;17(4):34–40. https://doi.org/10.17073/1997-308X-2023-4-34-40

Introduction

High-strength carbon fibers (CF) find a wide range of applications in today's technological, transportation, and construction industries. The development of these sectors heavily relies on the utilization of fibrous materials, and CFs are a key component in the production of composite materials. They are primarily derived from various polymer fibers, with polyacrylonitrile (PAN) fibers being the most common choice. PAn fibers offer exceptional properties, such as high strength, a relatively high modulus of elasticity, low specific gravity, and the ability to withstand high temperatures without weight loss. These characteristics make CFs valuable in various applications. Over the last few decades, a significant body of scientific and technical literature [1–18] has been dedicated to this subject. However, some physicochemical parameters' impact on the final properties of CF remains inadequately explored.

The objective of this research was to conduct a comprehensive examination of carbon fiber using a combination of analytical techniques, including *X*-ray phase structural analysis (XPSA), synchronous thermal analysis (STA), atomic emission spectral analysis (AESA), tomographic studies, and the assessment of fiber surface properties. The results obtained from these investigations have been consolidated.

For the experimental studies, UMT 49-12K-EP fiber from Alabuga-Volokno LLC (Umatex JSC) was selected as the starting material.

The data derived from these physico-chemical analytical studies serve as a valuable foundation for the development and proposal of further research methodologies for CF.

Experimental

The image of the fibers was obtained using a "SkyScan 1272" (Bruker, Germany) high resolution microtomograph. The scanning was conducted in filterless mode, with parameters set at 50 kV, 200 mA, a rotation step of 0.1°, and a pixel size of 3.81 μm. The reconstruction of the sections was carried out using "NRecon" and "CTvox" software».

For the *X*-ray phase structural analysis, a D8 Advance diffractometer (Bruker, Germany), which uses Bragg-Brentano geometry, was employed. This device utilized a copper *X*-ray tube capable of delivering up to 2200 W, generating CuK_α radiation with a wavelength of $\lambda = 0.15418$ nm. The occurred within the angular range of $2\theta = 10 \div 90°$, with an exposure time of approximately 10 min. The fibers were positioned on a silicon cuvette designed to minimize background interference, ensuring even distribution over its surface. Prior to each measurement, the *X*-ray tube and detector were calibrated. A specialized program, TOPAS, was utilized for the analysis of the diffractograms. The angular position of the diffraction maxima was measured with an absolute error not exceeding ±0.026°.

Atomic emission spectral analysis of CFs was carried out using a DFS-8 (LOMO company, St. Petersburg) in the wavelength range of 220–330 nm. The sample weight used was 7 mg. A glass electrode (type IV) was employed as the lower electrode, while a cone electrode (type I) served as the upper electrode. The fibers were placed in the lower electrode's crater and lightly dusted with high-purity graphite. The exposure time was set at 10 s, and a 17 A DC arc was employed. Spectra were recorded using a photoelectron cassette, and the analysis was conducted using the SM 2008 program (MORS LLC, Troitsk).

The CF sample also underwent simultaneous thermal analysis using an STA 449 F1 Jupiter device (Netzsch, Germany). The carbon fiber was analyzed under the following conditions:

1) in an argon environment (40 ml/min), with a sample weight of 5 mg. The heating process was uniform, with a rate of 5 °C/min in the temperature range of 25–955 °C, including a 10-min hold time at the maximum temperature;

2) in an air environment (40 ml/min), with a sample weight of 5 mg. Uniform heating at a rate of 5 °C/min took place in the temperature range of 25–950 °C.

The results obtained were processed using the "Proteus Thermal Analysis v.5.1.0" (Netzsch, Germany) software.

This data processing involved the determination of various parameters such as the beginning of weight loss temperatures, residual weight at the final temperature, temperature intervals corresponding to processes with thermal effects (either exo- or endothermic), peak temperature values for thermal effects, and more.

Results and discussion

Figure 1 displays the appearance of the original fiber.

The diffractograms were processed using a two-component profile description model. Figure 2 illustrates a diffractogram of UMT 49-12K-EP carbon fiber, which clearly demonstrates its amorphous nature. Carbon fibers belong to the non-graphitized materials category, meaning that the crystallites are randomly arranged and relatively small compared to graphitizing materials. Notably, there is an asymmetry towards smaller angles, a feature conventionally attributed to the presence of multiple structural components (SCs). In this paper, a two-component model of profile description is chosen (Fig. 3). A component with a larger spacing is referred to as a "kernel," and a component with a smaller spacing is considered a "shell." The approximate content of these components, as estimated by the peak areas, is 57 wt. % for SC 1 and 47 wt. % for SC 2.

The table shows that CF has a large interplanar distance and small crystallite sizes, indicating that this fiber belongs more to amorphous non-graphitic materials.

The absolute error of the AESA measurements was 70–0.5 ppm.

The results of atomic emission spectral analysis for the UMT 49-12K-EP sample are displayed below, ppm:

Fig. 1. UMT 49-12K-EP fiber fragment (3D reconstruction)

Рис. 1. Фрагмент волокна UMT 49-12K-EP (3D-реконструкция)

Al . . . 41	Mg . . . 30	Mo . . . 17	Cd . . . 3
B 5	Ca . . . 230	Ti 26	Ni . . . 7
Fe . . . 73	Co . . . 40	Mn . . . <0.1	Pb . . . 4
Si . . . **420**	Cr . . . 3	Cu . . . 6	V 4

$\Sigma_{\text{impurities}}$ – 909

Data from *X*-ray phase analysis of UMT 49-12K-EP carbon fiber

Данные рентгенофазового анализа углеволокна UMT 49-12K-EP

Structural component	d_{002}, nm	L_c, nm
SC 1	0.3523	2.2
SC 2	0.3894	1.4

Note. d_{002} – interplanar distance; L_c – crystallite size (perpendicular to the layer).
The measurement error for d_{002} was 0.05 % and for L_c it was 4.1 %.

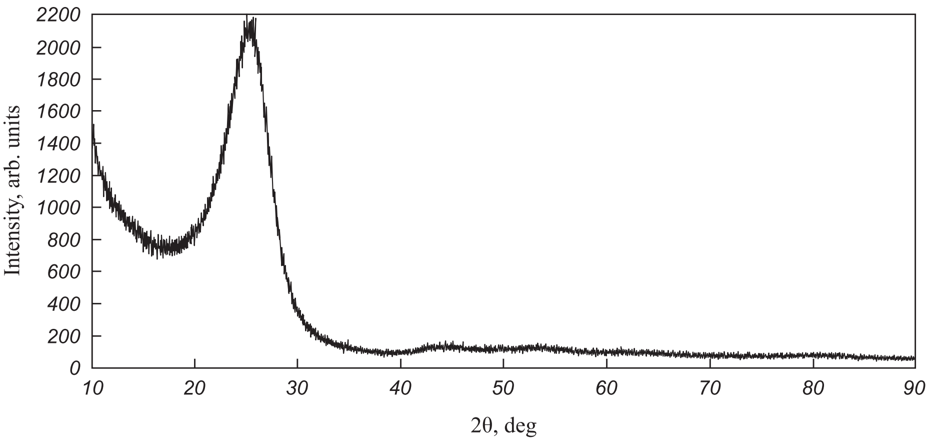

Fig. 2. Carbon fiber diffraction pattern

Рис. 2. Дифрактограмма углеволокна

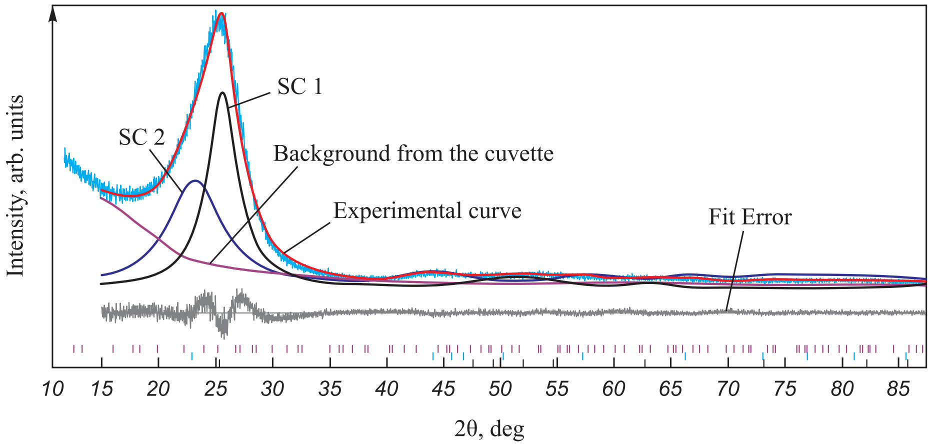

Fig. 3. Example of calculation using a two-component model

Рис. 3. Пример расчета по двухкомпонентной модели

The content of impurities in carbon fiber was determined in accordance with MI00200851-323-2009 (a procedure by JSC "NIIgraphite"). Silicon was identified as the primary contributor to the total impurity content. The presence of silicon is attributed to the addition of an organic compound containing silicon during the precursor's production phase for subsequent catalytic graphitization of hydrocarbons. Further details regarding the presence of Si in high-strength carbon fibers are elaborated upon in reference [19].

The results of thermal analysis of CFs are presented in the form of graphs displaying TG and DSC signals versus temperature (Fig. 4).

In an inert environment, as depicted in Figure 4, *a*, the CF sample initiates weight loss at temperatures exceeding 100 °C. At around 300 °C, a 0.3 % weight loss occurs, attributed to the gradual removal of residual moisture and volatile substances. Subsequently, the weight loss rate escalates significantly as a result of the thermal degradation of the epoxy sizing agent applied to the carbon fiber. This sizing agent serves to enhance the wettability and adhesion of polymer binders to the CF surface when producing composite materials. The drop in weight, about 1.5 % in the temperature range of 300÷400 °C aligns with the sizing agent's manufacturer-declared content in hydrocarbons (1.2–1.7 wt. %). Upon further heating in argon, weight loss essentially ceases (<0.1 wt. % at 400÷955 °C). The residual weight of CF at the final temperature is 98.15 wt. %, consistent with published data suggesting that, in an inert environment, carbon fiber can withstand heating above 1000 °C without altering its mechanical properties [3]. This high thermal resistance is achieved through the rigorous temperature treatment during the production of carbon fiber.

In the presence of atmospheric oxygen, when the temperature reaches 550 °C, the CF sample experiences a loss of over 5 % of its weight. As the temperature continues to rise, active oxidation (combustion) of the sample takes place, marked by a significant exothermic effect (a peak on the DSC curve at 781.5 °C). In previous studies [1; 3], it has been noted that in an air environment, the maximum operational temperature for carbon fiber without

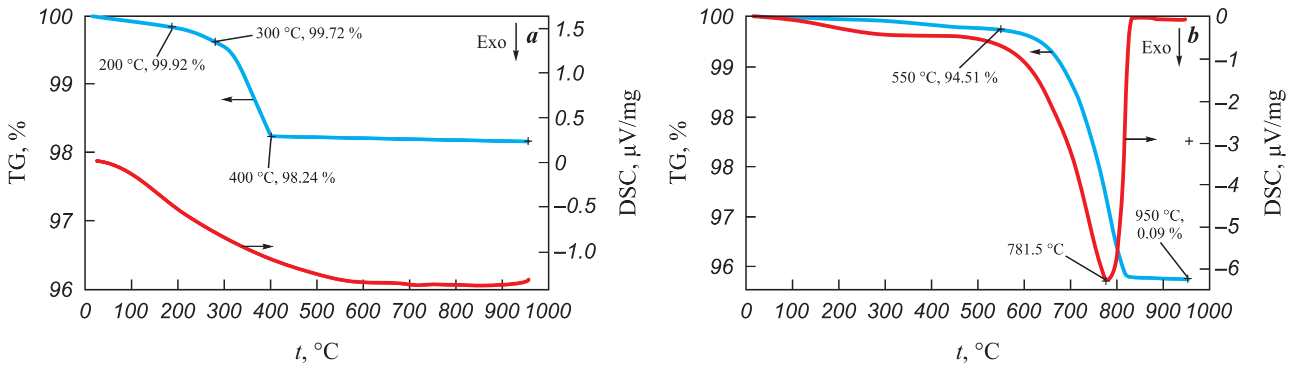

Fig. 4. Results of simultaneous thermal analysis of UMT 49-12K-EP carbon fiber in an inert environment (argon) (***a***) and in air (***b***)

Рис. 4. Результаты синхронного термического анализа углеволокна UMT 49-12K-EP в инертной среде (аргон) (***a***) и на воздухе (***b***) additives, before thermal oxidation initiates, ranges from 300–370 °C. Given that the residual weight at 950 °C is approximately 0.09 wt. % (equivalent to 900 ppm), in line with the earlier AES results ($\Sigma_{\text{impurities}}$ = 909 ppm), it can be inferred that the unburned residue comprises impurities such as silicon compounds, calcium, and other elements present in small quantities within the carbon fiber composition. These compounds appear to contribute to increasing the thermal oxidative stability of CF in the presence of air.

The surface properties of UMT49-12K-EP fiber were examined using nitrogen adsorption with an ASAP 2020 device (Micromeritics, USA). The specific surface area was determined using the BET method, while the volume of mesopores (diameter <900 Å) and their size distribution were calculated using the Barrett, Joyner, and Halenda (BJH) method across a pressure range of 0.35–0.95 p/p_s.

The CF surface properties are as follows:

S_{sp}, m^2/g 0.29
V_{p}, cm^3/g 0.0002
D_{p}, Å 255

where S_{sp} is the specific surface area, V_{p} is the relative volume of mesopores, D_{p} is their average diameter.

Figure 5 displays the mesopore size distribution. The graph of relative pore volume against their diameter exhibits distinct peaks, indicating the presence of groups of pores of similar size.

Figure 6 depicts the isotherm of the carbon sample under study. It falls into the 4th type of isotherms, following the BDDT international classification, which is characteristic of non-porous materials, specifically PAN fiber. On the adsorption branch, there's a consistent increase in specific sorption (V_{ads}) as the relative index p/p_s, rises, followed by a sharp increase at around $p/p_s = 1$. The isotherm exhibits an extended and irreversible hysteresis.

The determination of surface functional group content in the carbon fiber was conducted following the MI-00200851-331-2010 procedure (JSC NIIgraphfit). The analysis revealed the absence of carboxyl, phenolic, and carbonyl groups.

Based on the data acquired, we can deduce that the fiber's surface lacks activation and doesn't possess acid-base centers. In terms of its surface properties, the fiber aligns with the class of carbon fibers derived from PAN precursor [20–22]. It exhibits adsorption and chemical inactivity, which could further delineate its potential application.

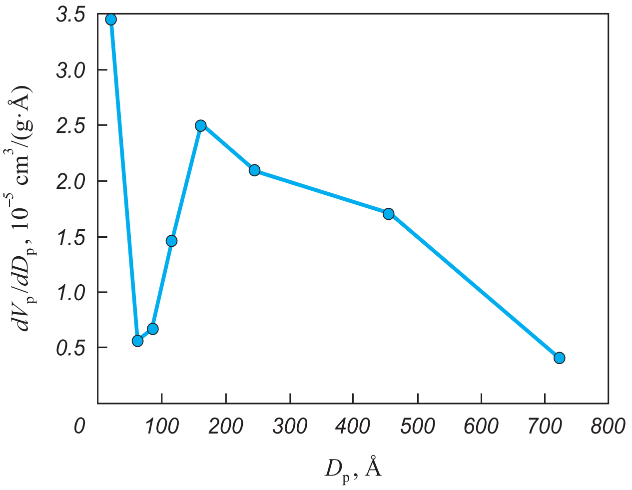

Fig. 5. Relative volume of mesopores as an integral function of their diameter

Рис. 5. Интегральная зависимость относительного объема мезопор от их диаметра

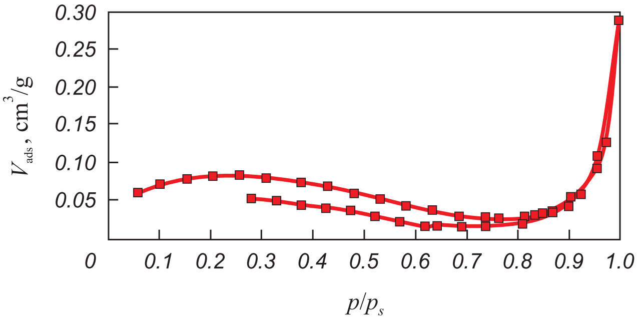

Fig. 6. Nitrogen adsorption-desorption isotherm

Рис. 6. Изотерма адсорбции-десорбции азота

Conclusions

1. The structural characteristics of carbon fiber have been thoroughly examined, and its chemical composition has been detailed. It has been conclusively determined that carbon fiber possesses an underdeveloped surface and does not contain surface carboxyl, phenolic, and carbonyl groups.

2. The predominant impurities in the chemical composition of carbon fiber have been identified as silicon compounds.

3. Precise temperatures for the thermal degradation of the carbon fiber sizing agent in an inert environment (300–400 °C) have been ascertained. The carbon fiber itself demonstrates exceptional heat resistance, enduring temperatures up to 950 °C without any loss of weight.

4. It has been established that the presence of elemental organic compounds in the composition of CF contributes significantly to an increase in thermal oxidative stability. Oxidation (combustion) commences at temperatures exceeding 550 °C, in contrast to the 350 °C threshold for CF without additives.

5. This research suggests new physico-chemical methods for investigating carbon fiber.

References / Список литературы

1. Fialkov A.S. Carbon-graphite materials. Moscow: Energiya, 1979. 320 p. (In Russ.).

   Фиалков А.С. Углеграфитовые материалы. М.: Энергия, 1979. 320 с.

2. Aizenshtein E.M., Klepikov D.N. Polyester fibers: today and tomorrow. *Vestnik Khimicheskoi Promyshlennosti*. 2016;91(4):6–10. (In Russ.).

   Айзенштейн Э.М., Клепиков Д.Н. Полиэфирные волокна: сегодня и завтра. *Вестник химической промышленности*. 2016;91(4):6–10

3. Simamura S. Carbon fiber. Moscow: Mir, 1987. 304 p. (In Russ.).

   Симамура С. (ред.). Углеродные волокна. М.: Мир, 1987. 304 с.

4. Kablov E.N. Innovative developments of FSUE “VIAM” SSC of RF on realization of “Strategic directions of the development of materials and technologies of their processing for the period until 2030”. *Aviatsionnye Materialy i Tekhnologii*. 2015;34(1):3–33. (In Russ.). https://doi.org/10.18577/2071-9140-2015-0-1-3-33

   Каблов Е.Н. Инновационные разработки ФГУП «ВИАМ» ГНЦ РФ по реализации «Стратегических направлений развития материалов и технологий их переработки на период до 2030 года». *Авиационные материалы и технологии*. 2015;34(1):3–33. https://doi.org/10.18577/2071-9140-2015-0-1-3-33

5. Meleshko A.I., Semenov V.I., Shaidurov V.S. Manufacture of carbon fibres and plastics based on them. GONTI-25. 1992;VIII(60):49. (In Russ.).

   Мелешко А.И., Семенов В.И., Шайдуров В.С. Производство углеродных волокон и пластиков на их основе. Под ред. С.П. Половникова. ГОНТИ-25. 1992;VIII(60):49.

6. Tyumentsev V.A., Fazlitdinova A.G. Study of fibrous carbon materials using X-ray diffractometry. *Zavodskaya laboratoriya. Diagnostika materialov*. 2019;85(11):31–36. (In Russ.).

   Тюменцев В.А., Фазлитдинова А.Г. Исследование волокнистых углеродных материалов методом рентгеновской дифрактометрии. *Заводская лаборатория. Диагностика материалов*. 2019;85(11):31–36.

7. Meleshko A.I., Polovnikov S.P. Carbon, carbon fibers, carbon composites. Moscow: Science Press, 2007.189 p. (In Russ.).

   Мелешко А.И., Половников С.П. Углерод, углеродные волокна, углеродные композиты. М.: Сайнс-Пресс, 2007. 192 с.

8. Kablov E.N. Composites: today and tomorrow. *Metally Evrazii*. 2015;1:36–39. (In Russ.).

   Каблов Е.Н. Композиты: сегодня и завтра. *Металлы Евразии*. 2015;1:36–39.

9. Sidorina A.I., Gunyaeva A.G. Market of carbon products and composites based on them. *Khimicheskie Volokna*. 2016;4:48–53. (In Russ.).

   Сидорина А.И., Гуняева А.Г. Рынок углеродных волокон и композитов на их основе. *Химические волокна*. 2016;4:48–53.

10. Bennett S.C., Johnson D.J., Johnson W.J. Strength-structure relationships in PAN-based carbon fibres. *Journal of Materials Science*. 1983;18:3337–3347.

11. Huang X. Fabrication and properties of carbon fibers. *Materials*. 2009;2:2369–2403.

12. Hu X., Wang L., Xu F., Xiao T., Zhang Z. *In situ* observations of fractures in short carbon fiber/epoxy composites. *Carbon*. 2014;67:368–376. https://doi.org/10.1016/j.carbon.2013.10.007

13. Goodhew P.J., Clarke A.J., Bailey J.E. Review of fabrication and properties of carbon-fibers. *Materials Science and Engineering*. 1975;17(1):3–30. https://doi.org/10.1016/0025-5416(75)90026-9

14. Panin M.I., Kapustin V.M., Tsymbalyuk A.E. The use of complex filaments for reinforcement of fibrous composite materials used in the oil and gas industry. *Izvestiya Vuzov. Tekhnologiya Tekstilnoi Promyshlennosti*. 2021;(6):103–106. (In Russ.).

    Панин М.И., Капустин В.М., Цимбалюк А.Е. Об использовании комплексных нитей для армирования волокнистых композиционных материалов, применяемых в нефтегазовой отрасли. *Известия вузов. Технология текстильной промышленности*. 2021;(6):103–106.

15. Gunyaeva A.G., Sidorina A.I., Kurnosov A.O., Klimenko O.N. Polymeric composite materials of new generation on the basis of binder VSE-1212 and the filling agents alternative to ones of Porcher Ind. and Toho Tenax. *Aviatsionnye Materialy i Tekhnologii*. 2018;3(52):18–26. (In Russ.). https://doi.org/10.18577/2071-9140-2018-0-3-18-26

    Гуняева А.Г., Сидорина А.И., Курносов А.О., Клименко О.Н. Полимерные композиционные материалы нового поколения на основе связующего ВСЭ-1212 и наполнителей, альтернативных наполнителям фирм Porcher Ind. и Toho Tenax. *Авиационные материалы и технологии*. 2018;3(52):18–26. https://doi.org/10.18577/2071-9140-2018-0-3-18-26

16. Morgan P. Carbon fibers and their composites. London: Taylor and Francis. 2005. 1200 p.

17. Park S.-J. Carbon fibers. 2nd ed. Springer, 2018. 366 p. (Springer Series in Materials Science, Vol. 210).

18. Frank E., Steudle L.M., Ingildeev D., Spörl J.M., Buchmeiser M.R. Carbon fibers: Precursor systems, processing, structure, and properties. *Angewandte Chemie International Edition in English*. 2014;53(21):5262–5298. https://doi.org/10.1002/anie.201306129

19. Verbets D.B., Samoilov V.M., Bubnenkov I.A., Buchnev L.M., Nakhodnova A.V., Stepareva N.N. Change in the structure and properties of carbon fibers during graphitazion using an exstract or a hologencontaining medium. In: *The Research Institute of Graphite-based Structural Materials is 60 years old*. Moscow: Nauchnye tekhnologii, 2020. P. 86–102. (In Russ.).

    Вербец Д.Б., Самойлов В.М., Бубненков И.А., Бучнев Л.М., Находнова А.В., Степарева Н.Н. Изменение структуры и свойств углеродных волокон при графитации с использованием вытяжки или галогенсодержащей среды. В сб.: *Научно-исследовательскому институту конструкционных материалов на основе графита – 60 лет*. М.: Научные технологии, 2020. С. 86–102.

20. Beck N.V., Meech S.E., Norman P.R., Pears L.A. Characterisation of surface oxides on carbon and their influence on dynamic adsorbtion. *Carbon*. 2002;40: 531–540.
https://doi.org/10.1016/S0008-6223(01)00144-0

21. Ho K., Qian H., Bismarck A. Carbon fiber: Surface properties. In: Wiley Encyclopedia of Composites. John Wiley & Sons, Inc., 2011. P. 1–11.
https://doi.org/10.1002/9781118097298.weoc024

22. Martínez-Alonso A., Jamond M., Montes-Morán M.A., Tascón J.M.D. Microporous texture of activated carbon fibers prepared from aramid fiber pulp. *Microporous and Mesoporous Materials*. 1997;11:303–311.
https://doi.org/10.1016/S0927-6513(97)00050-3

Сведения об авторах

Елена Геннадьевна Чеблакова – к.т.н., ст. науч. сотрудник, начальник Испытательного центра углеродных материалов АО «НИИграфит»
ORCID: 0000-0003-4921-095X
E-mail: EGCheblakova@rosatom.ru

Борис Сергеевич Клеусов – науч. сотрудник Испытательного центра углеродных материалов АО «НИИграфит»
ORCID: 0000-0003-3924-2616
E-mail: BSKleusov@rosatom.ru

Вадим Игоревич Сапожников – науч. сотрудник Испытательного центра углеродных материалов АО «НИИграфит»
ORCID: 0000-0003-3433-3631
E-mail: ValSapozhnikov@rosatom.ru

Валентина Анатольевна Горина – науч. сотрудник Испытательного центра углеродных материалов АО «НИИграфит»
ORCID: 0000-0002-7470-5578
E-mail: VAGorina@rosatom.ru

Юлия Алексеевна Малинина – науч. сотрудник Испытательного центра углеродных материалов АО «НИИграфит»
ORCID: 0000-0002-7677-2803
E-mail: YAMalinina@rosatom.ru

Артур Радикович Гареев – к.т.н., заместитель директора по науке и инновациям АО «НИИграфит»
ORCID: 0000-0001-5934-8456
E-mail: ARGareev@rosatom.ru

Information about the Authors

Elena G. Cheblakova – Cand. Sci. (Eng.), Senior Researcher, Head of Testing Center of Carbon Materials of NIIgraphite JSC
ORCID: 0000-0003-4921-095X
E-mail: EGCheblakova@rosatom.ru

Boris S. Kleusov – Researcher of Testing Center of Carbon Materials of NIIgraphite JSC
ORCID: 0000-0003-3924-2616
E-mail: BSKleusov@rosatom.ru

Vadim I. Sapozhnikov – Researcher of Testing Center of Carbon Materials of NIIgraphite JSC
ORCID: 0000-0003-3433-3631
E-mail: ValSapozhnikov@rosatom.ru

Valentina A. Gorina – Researcher of Testing Center of Carbon Materials of NIIgraphite JSC
ORCID: 0000-0002-7470-5578
E-mail: VAGorina@rosatom.ru

Yuliya A. Malinina – Researcher of Testing Center of Carbon Materials of NIIgraphite JSC
ORCID: 0000-0002-7677-2803
E-mail: YAMalinina@rosatom.ru

Artur R. Gareev – Cand. Sci. (Eng.), Deputy Director for Science and Innovation of NIIgraphite JSC
ORCID: 0000-0001-5934-8456
E-mail: ARGareev@rosatom.ru

Вклад авторов

Е. Г. Чеблакова – определение цели работы, первоначальная редакция, написание статьи.
Б. С. Клеусов – проведение рентгенофазового анализа и атомно-эмиссионного спектрального анализа, участие в обсуждении результатов.
В. И. Сапожников – проведение синхронного термического анализа, участие в обсуждении результатов.
В. А. Горина – проведение компьютерной томографии и определение поверхностных свойств, участие в обсуждении результатов.
Ю. А. Малинина – определение функциональных групп, участие в обсуждении результатов.
А. Р. Гареев – постановка задачи исследования, общая редакция статьи, участие в обсуждении результатов.

Contribution of the Authors

E. G. Cheblakova – formulated the research objectives, carried out the initial draft of the article, and authored the manuscript.
B. S. Kleusov – conducted *X*-ray phase analysis and atomic emission spectral analysis, contributed to result discussions.

V. I. Sapozhnikov – performed synchronous thermal analysis, participated in result discussions.
V. A. Gorina – carried out computer tomography and assessed surface properties, contributed to result discussions.

Yu. A. Malinina – identified functional groups, participated in result discussions.
A. R. Gareev – framed the research objectives, oversaw general article editing, and participated in result discussions.

Статья поступила 27.09.2022 г.
Доработана 01.12.2022 г.
Принята к публикации 09.12.2022 г.

Received 27.09.2022
Revised 01.12.2022
Accepted 09.12.2022

Refractory, Ceramic and Composite Materials
Тугоплавкие, керамические и композиционные материалы

UDC 621.762

https://doi.org/10.17073/1997-308X-2023-4-41-50

Research article
Научная статья

In situ study of mechanical properties and structural transformations during heating of WC–TaC–Co cemented carbides in a transmission electron microscope column

A. A. Zaitsev, P. A. Loginov, E. A. Levashov

National University of Science and Technology "MISIS"
4 Bld. 1 Leninskiy Prosp., Moscow 119049, Russia

aazaitsev@bk.ru

Abstract. This study investigated the hardness of lamella with varying thickness, obtained from a massive, fine-grained cemented carbide comprising WC–6 %Co–0.2 %TaC, characterized by an average grain size of approximately 5 μm. The picoindentation method was employed for this analysis. Picoindentation was carried out using a Berkovich diamond indenter with a radius of curvature around 50 nm, and the experimental data were analyzed using the Oliver–Pharr model. The results revealed a significant correlation between hardness and lamella thickness. The hardness of the electron transparent section (thickness less than 100 nm) of the lamella measured 11.3±2.8 GPa, while the electron nontransparent section (thickness more than 200 nm) exhibited a hardness of 20.8±1.2 GPa. The lower hardness in electron transparent objects (thickness ~100 nm) is likely attributed to a combination of factors, including the potential bending of thin cobalt layers, the presence of edge effect, and closely spaced structural defect dislocations on the lamella surface. *In situ* TEM studies were conducted to examine structural transformations during the heating of WC–6 %Co–0.2 %TaC lamella, including in the presence of oxide phases (WO_x). Oxide phases on the lamella's surface were generated by oxidizing the lamella at 200 °C in an air atmosphere. The results indicated that heating up to 500 °C did not bring about significant changes in the structure. However, at 600 °C, there was a notable thinning of cobalt layers due to intense surface diffusion of cobalt. Simultaneously, the formation of nanosized particles of the Co_3W_3C phase, ranging in size from 5 to 20 nm, was observed in the binder. These particles resulted from a shift in the equilibrium phase composition of the carbide, changing from a two phase region (WC + γ) to a three phase region ($WC + \gamma + Co_3W_3C$) as a consequence of the lamella's oxidation.

Keywords: hardmetals, *in situ* testing, picoindentation, hardness, deformation, tantalum carbide, oxidation of hardmetals

Acknowledgements: This research was supported by the Ministry of Science and Higher Education of the Russian Federation (project No. 0718-2020-0034).

For citation: Zaitsev A.A., Loginov P.A., Levashov E.A. *In situ* study of mechanical properties and structural transformations during heating of WC–TaC–Co cemented carbides in a transmission electron microscope column. *Powder Metallurgy and Functional Coatings*. 2023;17(4):41–50. https://doi.org/10.17073/1997-308X-2023-4-41-50

In situ исследование механических свойств и структурных превращений при нагреве твердых сплавов WC–TaC–Co в колонне просвечивающего электронного микроскопа

А. А. Зайцев, П. А. Логинов, Е. А. Левашов

Национальный исследовательский технологический университет «МИСИС»
Россия, 119049, г. Москва, Ленинский пр., 4, стр. 1

aazaitsev@bk.ru

Аннотация. Методом пикоиндентирования изучена твердость ламели переменной толщины, вырезанной из массивного мелкозернистого твердого сплава WC–6 %Co–0,2 %TaC с размером зерна около 0,5 мкм. Пикоиндентирование проводилось алмазным индентором Берковича с радиусом закругления около 50 нм, а обработка экспериментальных кривых выполнена по модели Оливера–Фарра. Показано, что значения твердости, получаемые при пикоиндентировании ламели, существенно зависят от ее толщины. Твердость электронно-прозрачного участка (толщина менее 100 нм) ламели составляет 11,3 ± 2,8 ГПа, а электронно-непрозрачного (толщина более 200 нм) – 20,8 ± 1,2 ГПа. Пониженные значения твердости в электронно-прозрачных объектах (толщина ~100 нм) предположительно связаны с комбинацией нескольких факторов: возможным изгибом тонких кобальтовых прослоек, наличием краевого эффекта и близко расположенных стоков дефектов структуры, в роли которых выступает поверхность ламели. Выполнены *in situ* ПЭМ-исследования структурных превращений при нагреве ламели WC–6 %Co–0,2 %TaC, в том числе в присутствии оксидных фаз (WO_x). Оксидные фазы на поверхности ламели были получены в результате окисления ламели при температуре 200 °C в воздушной атмосфере. Показано, что при нагреве до 500 °C существенных изменений структуры не наблюдается, а при температуре 600 °C начинается быстрое утонение кобальтовых прослоек за счет интенсивной поверхностной диффузии кобальта. Одновременно с этим зафиксировано образование в связке наноразмерных частиц фазы Co_3W_3C дисперсностью от 5 до 20 нм, которые появляются по причине смещения равновесного фазового состава твердого сплава из двухфазной области WC + γ в трехфазную WC + γ + Co_3W_3C в результате окисления ламели.

Ключевые слова: твердые сплавы, *in situ* испытания, пикоиндентирование, твердость, деформация, карбид тантала, окисление твердых сплавов

Благодарности: Работа выполнена при поддержке Министерства науки и высшего образования РФ в рамках государственного задания (проект № 0718-2020-0034).

Для цитирования: Зайцев А.А., Логинов П.А., Левашов Е.А. *In situ* исследование механических свойств и структурных превращений при нагреве твердых сплавов WC–TaC–Co в колонне просвечивающего электронного микроскопа. *Известия вузов. Порошковая металлургия и функциональные покрытия*. 2023;17(4):41–50. https://doi.org/10.17073/1997-308X-2023-4-41-50

Introduction

Cemented carbides, often referred to as hardmetals, represent a class of metal composites characterized by a hard carbide skeleton embedded within a ductile metallic binder predominantly composed on iron-group metals. Due to their exeptional performance characteristics, carbide tools are widely used in the metalworking and mining industries, as well as in construction and mechanical engineering.

In the metalworking and mining sectors, the most significant cost savings are often achieved by increasing metal cutting speeds and rock drilling. This results in higher tool loads and elevated temperatures, which can reach 1000 °C or more on the tool surface. High contact stresses can lead to substantial plastic deformation of carbide cutting edges, and it is often this plastic deformation that determines the tool's lifespan. Research into the plastic deformation of hardmetals at elevated temperatures [1] has revealed that the carbide skeleton is destroyed during high-temperature deformation. This, in turn, results in the formation of cohesive phase interlayers between WC grains, facilitating the of grain-boundary sliding process.

In recent years, efforts have been made to enhance the plastic deformation resistance of hardmetals through the addition of refractory metal carbides [2–5]. Various works have employed Mo_2C [6–11], TiC, and TaC [12–19] additives. It has been found that even small additions of TaC significantly improve the plastic deformation resistance of cemented carbides at higher temperatures. It is hypothesized that tantalum affects the interfacial energy at the WC/Co and WC/WC interfaces, resulting in the reinforcement of the carbide skeleton [18]. Nevertheless, the mechanism of tantalum carbide's influence on the mechanical and high-temperature properties of hardmetals remains inadequately studied, as indicated by the data in [20].

Over the last few decades, new approaches to studying mechanical properties and structural characteristics of materials have been intensively developed. These approaches include micromechanical testing [21; 22], as well as the investigation of structural transformations during the heating of electron-transparent objects directly within the transmission electron microscope (TEM) column [23–25]. Such studies yield substantial fundamental insights, enabling a deeper comprehension of the deformation and fracture mechanisms of bulk materials, as well as the prediction of their performance characteristics.

The objective of this study was to examine the mechanical properties at room temperature and structural transformations at elevated temperatures of hardmetals containing TaC additives. The investigations were conducted in situ within a transmission electron microscope column at both ambient and higher temperatures.

Experimental

The subject of investigation in this study was a fine-grained WC–6 %Co–0.2 %TaC hard metal, which was derived from a mixture of WC, Co, and TaC powders. A lamella was cut out from a solid carbide sample using the focused ion beam method on the FEI Quanta 200 3D (FEI Company, USA) for the picoindentation experiment and then soldered to a special holder, as depicted in Figure 1.

Picoindentation [26] was carried out *in situ* within a PEM column using a “Hysitron PI 95 TEM Picoindenter” holder (Bruker, USA) designed for mechanical testing and equipped with a Berkovich diamond indenter. The indentation process was recorded *in situ* in a JEM-2100 TEM column (JEOL Ltd., Japan). The lamella had a length of about 11 µm and consisted of two sections with varying thickness: one of them was electron-transparent (with a thickness ranging from 70 to 120 nm), while the other was nontransparent to the electron beam (with a thickness exceeding 200 nm).

According to the well-known Oliver–Pharr model [27], which is applicable for interpreting picoindentation results, hardness is determined by the following equation:

$$H = F_{\max}/A, \tag{1}$$

where $F_{\max}$ represents the maximum load, N; A is the surface area of the indenter’s contact with the sample, m^2.

The contact area, accounting for the radius of curvature of a real Berkovich indenter (approximately 50 nm), was determined as follows:

$$A = 24.5h_c^2 + 1.65\cdot 10^{-6} h_c. \tag{2}$$

The depth of contact between the indenter and the sample (h_c, m) was calculated using the equation:

$$h_c = h_{\max} - 0.75F_{\max}\left(\frac{dh}{dF}\right)_{F_{\max}}, \tag{3}$$

where $h_{\max}$ is the maximum depth of indenter penetration, m.

The lamella was heated using a “Gatan heating holder 652” (Gatan, USA) by passing an electric current through a ring-shaped tantalum heater that surrounded the lamella. The heating rate was set at 50±5 K/min. In order to examine the alloy’s structure, temperatures of 300, 400, 500 and 600 °C were selected. *In situ* imaging of the structure was performed within a JEM-2100 TEM column (JEOL Ltd., Japan) at these specific temperatures. The samples were allowed to stabilize for several

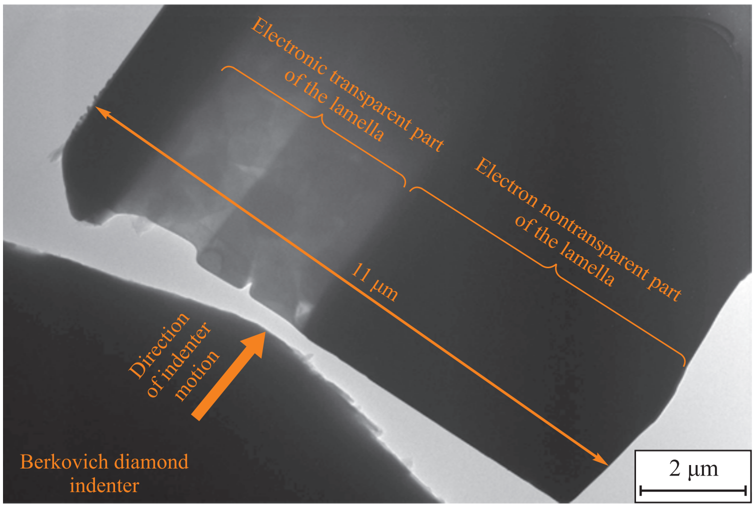

Fig. 1. Appearance of the lamella before picoindentation tests

Рис. 1. Внешний вид ламели перед началом испытаний по пикоиндентированию minutes to eliminate temperature gradients, which could cause sample drift. The recording duration ranged from 15 to 20 min before activating the heating process.

Results and discussion

The average grain size of the examined hard metal, composed of WC–6 %Co–0.2 %TaC, measured approximately 0.5 μm (Fig. 2). The thickness of the cobalt interlayers fell within the range of 100 to 200 nm. As a result, the size relationship between the indenter and the structural elements of the alloy leads us to conclude that during picoindentation, multiple grains of the carbide phase and cobalt interlayers were concurrently deformed. The resultant picohardness characterizes the hardness of the entire composite, rather than individual structural components.

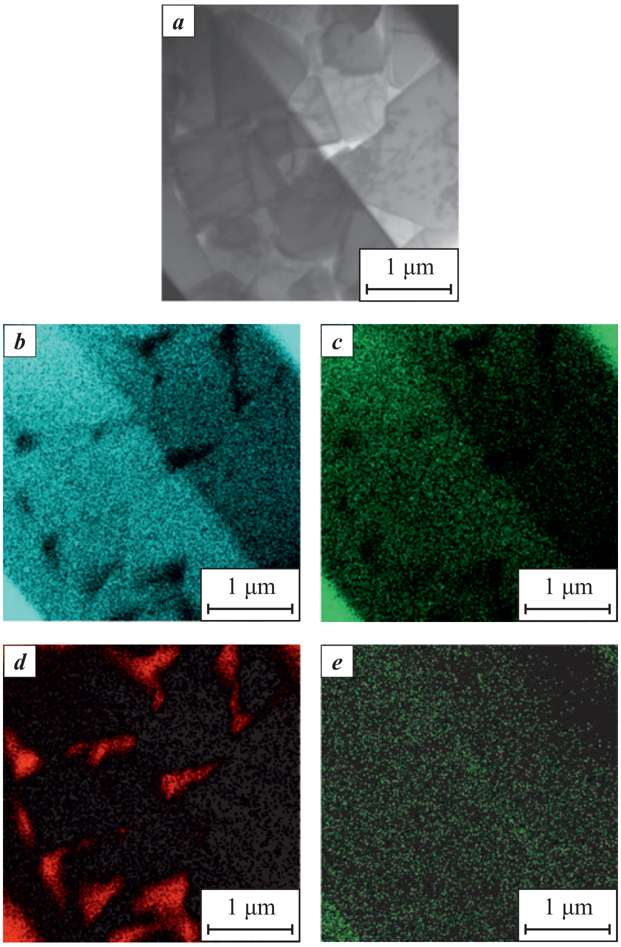

Fig. 2. EDS maps of electron-transparent part of the WC–6 %Co–0.2 %TaC lamella
a – STEM image; ***b–e*** – W, Ta, Co and C EDS maps, respectively

Рис. 2. Карты распределения элементов в электронно-прозрачной части ламели твердого сплава WC–6 %Co–0,2 %TaC
a – изображение, полученное в режиме СТЭМ; ***b–e*** – изображения, полученные в характеристическом излучении W, Ta, Co, C, соответственно

Figure 3 displays two characteristic curves obtained during picoindentation of a hard metal. A series of 12 individual tests were conducted in different areas of the lamella, with a maximum test load of 900 μN, and the exposure time at maximum load was 5 s. The resulting curves can be categorized based on the maximum indenter penetration depth ($h_{\max}$). The first group comprises tests with a penetration depth ranging from 100 to 115 nm, while the second group covers tests with a depth of 50 to 60 nm. Notably, all tests in the first group were executed on a thin (electron-transparent) section of the lamella, whereas those in the second group were performed on a thicker section. Figure 3 illlustrates that at the maximum load, there is a slight displacement (drift) of the testing system, ranging from 1 nm (Fig. 3, *a*) to 2 nm (Fig. 3, *b*). This corresponds from 2 to 4 % of the maximum indenter penetration depth. Consequently, the displacement of the testing system has minimal impact on the shape of the displacement-load curve. The drift rate fluctuates between 0.2 to 0.4 nm/s at a load of 900 μN. However, since the relationship between drift speed and load is unknown, no adjustments were made to the experimental data.

Figure 4 presents a videogram depicting the indentation of a thin section of the lamella. Clearly, during the test,

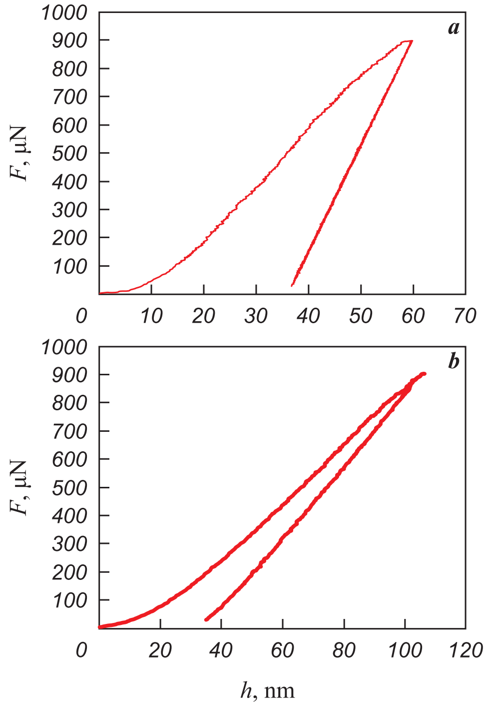

Fig. 3. Typical indentation curves in "load–displacement" coordinates
a – electron-nontransparent part of the lamella
b – electron-transparent part of the lamella

Рис. 3. Характерные кривые индентирования в координатах «нагрузка–перемещение»
a – для электронно-непрозрачного участка ламели
b – для электронно-прозрачного участка ламели

the indenter made contact with multiple WC grains and the cobalt layers that separate them. Importantly, no cracks or defects were observed after the indentation of the electron-transparent portion of the lamella (Fig. 4, *d*).

The picoindentation results were analyzed using the Oliver–Pharr model [22], and the calculated hardness values are summarized in Table.

The hardness of the electron-transparent section of the lamella measured 11.3±2.8 GPa, while the electron non-transparent section records a hardness of 20.8±1.2 GPa. Indentation of the electron-transparent part of the lamella is associated with significantly greater deformations, resulting in an underestimation of hardness and greater result dispersion. This reduction in hardness is likely attributed to edge effects and the proximity of structural defects, which are often located on the surface of the sample. The proximity of structural defects also accounts for the higher plasticity observed in nanoscale objects during *in situ* micromechanical tests. Another possible factor that could distort the picoindentation results is the bending of cobalt layers. It's probable that during picoindentation, there is a transition from purely compressive to mixed bending-compressive loads.

The hardness obtained from the electron nontransparent region correlates well with published data, which suggests that for massive samples of fine-grained WC–6 %Co alloys, hardness typically falls within the range of 18 to 20 GPa [28].

Picoindentation curve results analized using the Oliver–Pharr model

Результаты обработки кривых пикоиндентирования по модели Оливера–Фарра

Measurement No.	Indentation point	H_i, GPa	H, GPa
1	Electron-transparent part of the lamella	13.2	11.3 ± 2.8
2		6.7	
3		8.9	
4		13.3	
5		12.4	
6		13.0	
7	Electron non-transparent part of the lamella	19.6	20.8 ± 1.2
8		22.1	
9		19.3	
10		21.3	
11		20.8	
12		21.9	

As previously mentioned, during the operation of hardmetals in cutting metals and mining minerals, local temperature increases of up to 1000 °C or more are observed. This rise in the temperature of the air-exposed surface layers of the tool results in the formation of oxides due to interaction with atmospheric oxygen, contributing to abrasive (or hydro-abrasive) corrosion-abrasive

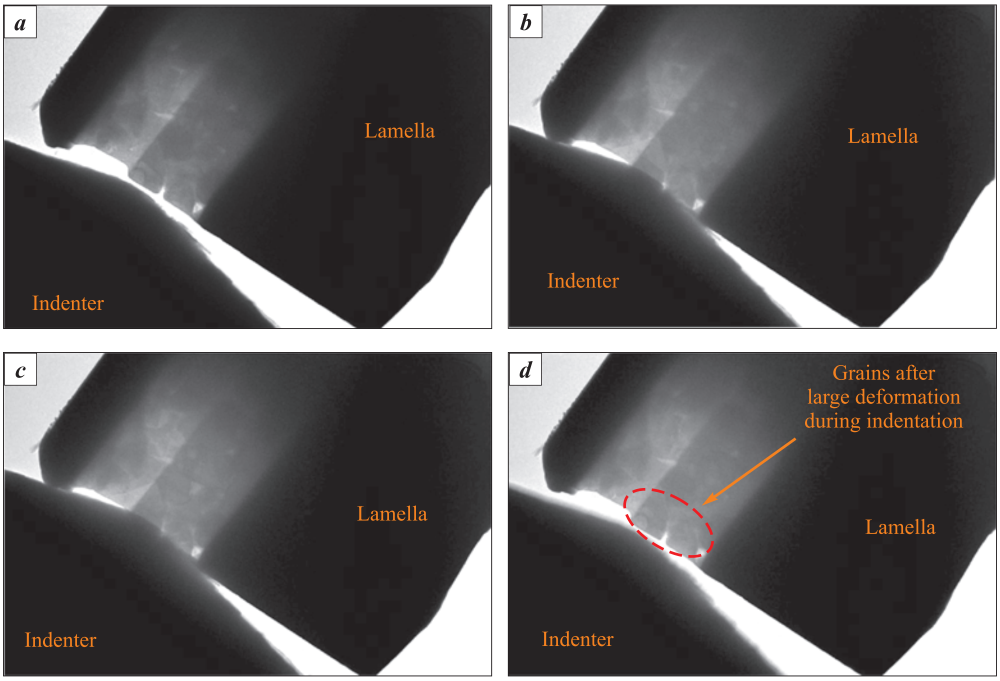

Fig. 4. Videogram of the picoindentation of electron-transparent section of the lamella
F, μN: 0 (***a***, before indentation); 450 (***b***); 900 (***c***); 0 (***d*** after indentation, the indenter is pulled back)

Рис. 4. Видеограмма процесса пикоиндентирования электронно-прозрачной части ламели
F, мкН: 0 (***a***, до начала индентирования); 450 (***b***); 900 (***c***); 0 (***d***, после индентирования, индентор отведен)

wear. Therefore, the study of structural transformations of carbide surface layers during heating in an oxidizing atmosphere is crucial for understanding the dynamic processes occurring in hardmetals tool during operations.

In order to investigate the characteristics of structural transformations in lamellas when heated within a transmission electron microscope column in the presence of oxide phases, a lamella was created from a fine-grained hard metal WC–6 %Co–0.2 %TaC. The TEM column is maintained under deep vacuum (less than 10^{-5} Pa), making it impossible to create even a very rarefied oxidizing atmosphere. As a result, the lamella was subjected to oxidation at a temperature of 200 °C for 4 h in an air atmosphere. These mild oxidation conditions led to the development of an oxidized layer on the lamella's surface, which was intended to serve as a source of oxygen with further temperature increases.

TEM images of the lamella structure after oxidation are depicted in Figure 5. The sample exhibited a typical hard metal structure with faceted WC grains ranging in size from 0.2 to 0.6 μm, embedded within a γ phase binder (cobalt-based solid solution), with interlayer thicknesses spanning from 50 to 250 nm. As seen in Figure 5, *b*, the binding γ phase contains needle-shaped particles measuring about 5 nm in diameter, the composition of which can presumably be described by the formula: $W_xTa_yCo_zC_u$. The surface of WC grains is uniformly covered with nanoparticles ranging in size from 5 to 30 nm, which, according to electron probe microanalysis (EPMA), are tungsten oxides WO_x with variable stoichiometry.

It's worth noting that the presence of copper, as indicated by EPMA data (Fig. 5, *e*), is an artifact attributed to the soldering of the lamella to the copper holder. No oxide particles were detected in the cobalt phase, which confirms the greater affinity of tungsten for oxygen compared to cobalt.

In order to investigate the behavior of the oxidized hard metal after heating, the lamella was subjected to temperature increases within the TEM column, reaching 400, 500 and 600 °C. The images illustrating the alloy's structure after heating phase are presented in Figures 6, 7 and 8, respectively.

Up to a temperature of 500 °C, no significant alterations in the lamella's structure are observed. Some thinning of the cobalt layers was detected, which enhances the contrast of the $W_xTa_yCo_zC_u$ phase. At a temperature of 600 °C, rapid thinning of the cobalt interlayers commences, leading to the formation of voids (Fig. 8, *b*). The redistribution of cobalt across the sample's surface, including the surface of tungsten carbide grains, appears to occur through a mechanism of surface diffusion. This effect was previously established when heating a lamella composed of a hard metal that has not undergone oxidation [29]. In the case of grains coated with WO_x nanoparticles, no droplet accumulations of the cobalt phase are formed, which is explained by the limited wettability of oxide particles by cobalt.

Another phenomenon observed in the γ phase at a temperature of 600 °C is the development of equiaxed nanoparticles with sizes ranging from 5 to 20 nm, as clearly depicted in Figure 8, *d*. Based on the results of microdiffraction analysis (see the inset in Figure 8, *c*), the following interplanar distances were identified within this phase, measured in nm: 0.239, 0.205 and 0.1846. These correspond to reflections from crystallographic planes with indices (422), (440) and (620) of Co_3W_3C phase, with reference interplanar distances of 0.2269, 0.1965, and 0.1758 nm, respectively. The noticeable discrepancy between the experimental and reference interplanar distances can be attributed to the temperature-induced expansion of the crystal lattice. Without account-

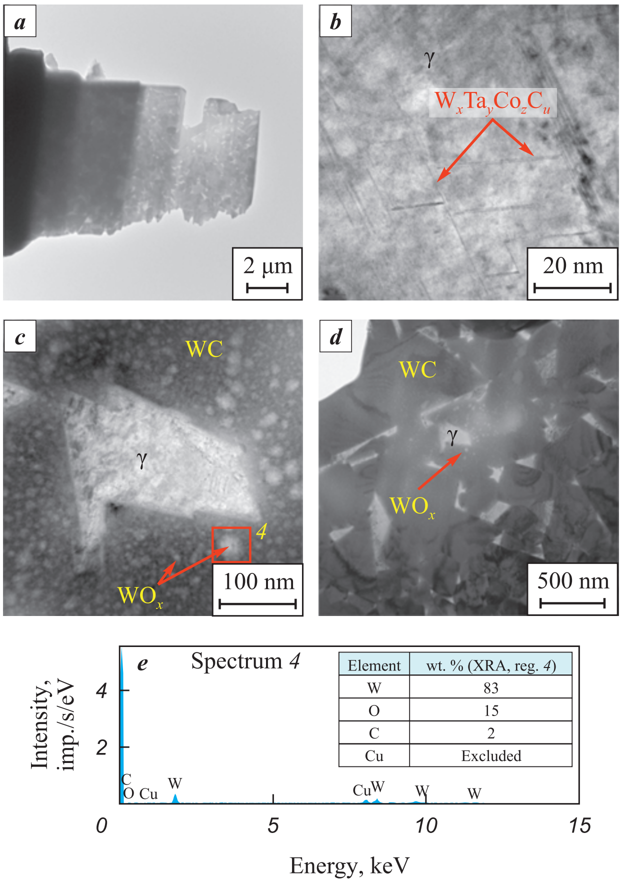

Element	wt. % (XRA, reg. 4)
W	83
O	15
C	2
Cu	Excluded

Fig. 5. TEM images of the fine-grained WC–6 %Co–0.2 %TaC lamella after oxidation
a – general view of the lamella; ***b*** – γ-phase structure with of $W_xTa_yCo_zC_u$ nanoparticles; ***c, d*** – lamella areas with clearly visible nanoparticles of the oxide phase on the surface of WC grains; ***e*** – EDS spectrum from the region depicted in Fig. 5, ***c***

Рис. 5. ПЭМ-изображения ламели из мелкозернистого твердого сплава WC–6 %Co–0,2 %TaC после окисления
a – общий вид ламели; ***b*** – структура γ-фазы с наночастицами, состоящими из $W_xTa_yCo_zC_u$; ***c, d*** – участки ламели с хорошо видимыми наночастицами оксидной фазы на поверхности зерен WC; ***e*** – спектр ЭДС с области, показанной на рис. 5, ***c***

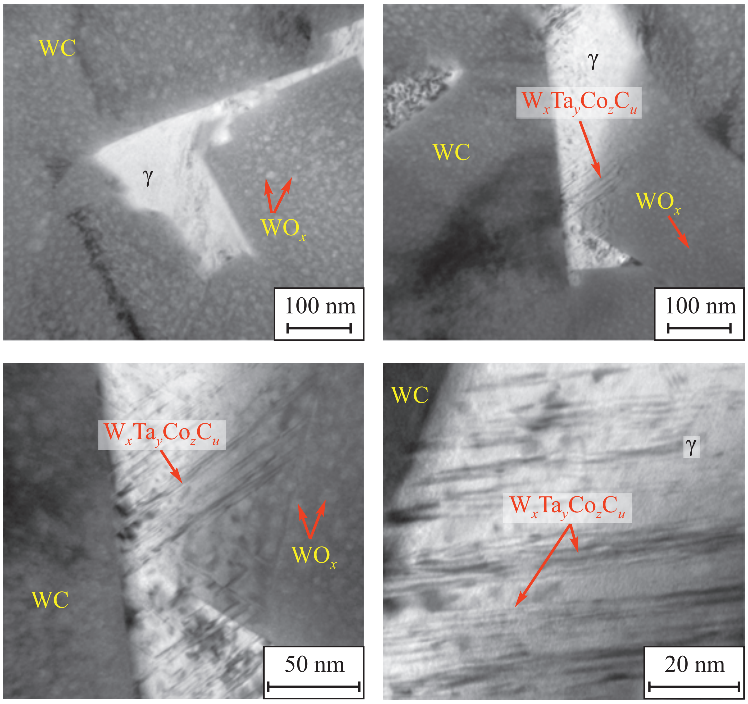

Fig. 6. TEM images of the WC–6 %Co–0.2 %TaC lamella after heating to 400 °C

Рис. 6. ПЭМ-изображения ламели из твердого сплава WC–6 %Co–0,2 %TaC после нагрева до 400 °C

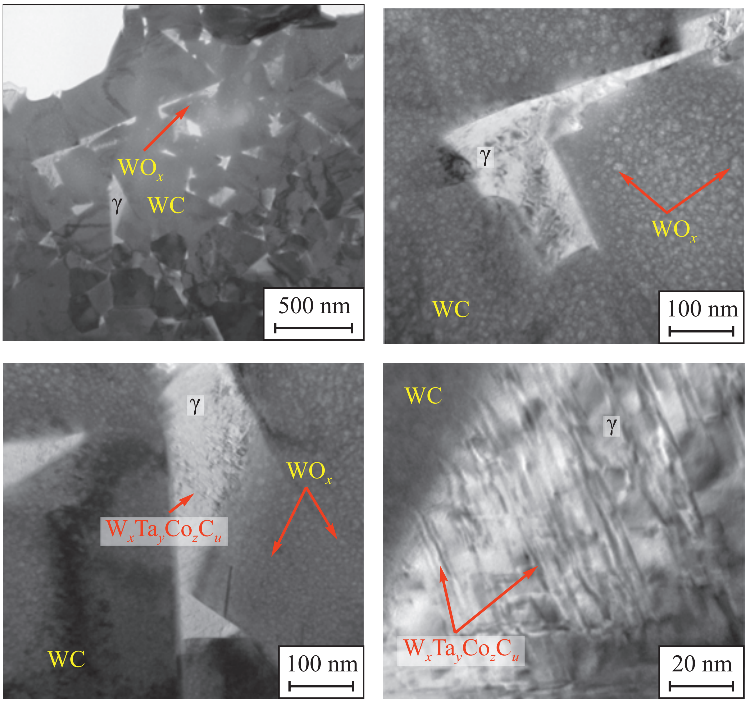

Fig. 7. TEM images of the WC–6 %Co–0.2 %TaC lamella after heating to 500 °C

Рис. 7. ПЭМ-изображения ламели из твердого сплава WC–6 %Co–0,2 %TaC после нагрева до 500 °C

ing for the anisotropy of the linear expansion coefficient of the Co_3W_3C phase (approximately $9{\cdot}10^{-6}$ K^{-1}) at 600 °C, the reference lattice periods increase to 0.23212, 0.20172, and 0.18102 nm, aligning more closely with the experimental data. The formation of the Co_3W_3C phase arises as a consequence of a shift in the carbon balance due to the lamella's oxidation, leading to an alteration in the equilibrium phase composition of the carbide from a two-phase region ($WC + \gamma$) to a three-phase region $WC + \gamma + Co_3W_3C$. In addition to the sur-

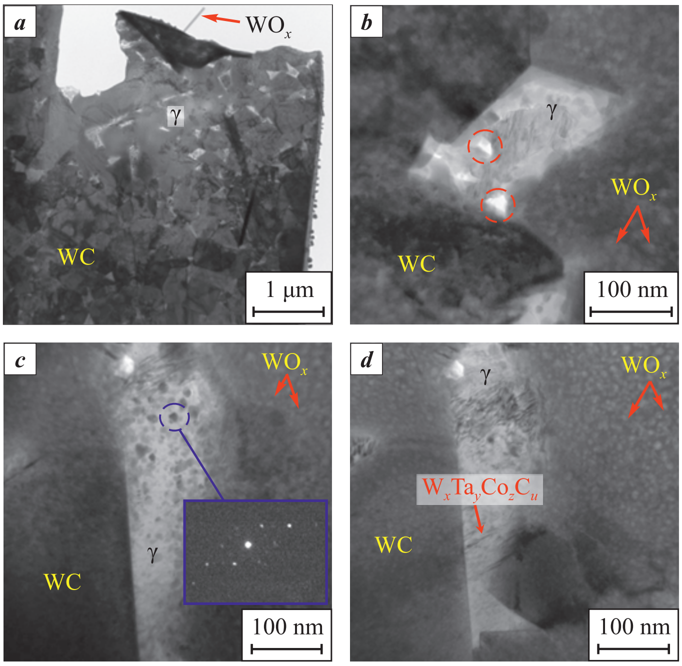

Fig. 8. TEM images of the WC–6 %Co–0.2 %TaC lamella after heating to 600 °C

Рис. 8. ПЭМ-изображения ламели из твердого сплава WC–6 %Co–0,2 %TaC после нагрева до 600 °C

face diffusion of cobalt and the formation of Co_3W_3C phase, the appearance of WO_x particles along the edges of the lamella was observed. Some of these particles took the form of nanofibers with a diameter of roughly 30 nm and a length of approximately 0.8 μm. Electron-probe microanalyzer (EPMA) was employed to determine the composition of these particles, as illustrated in Figure 9, which corresponds to tungsten oxide with stoichiometry closely resembling WO_2.

Conclusions

The study examined the hardness of the lamella with varying thickness, composed of WC–6 %Co–0.2 %TaC alloy, using picoindentation. The results clearly illustrate that the hardness values obtained via picoindentation are notably influenced by the lamella's thickness. The hardness of the electron-transparent segment of the lamella measures 11.3±2.8 GPa, while the electron-opaque portion records a hardness of 20.8±1.2 GPa. The lower hardness observed in electron transparent regions (thickness ~100 nm) is likely due to a combination of various factors, including potential bending of thin cobalt layers, the presence of edge effects, and the proximity of closely spaced structural defect sites along the lamella's surface.

In situ studies were conducted to investigate structural transformations during heating of WC–6 %Co–0.2 %TaC alloy, including in the presence of oxide phases. The findings revealed that up to a temperature of 500 °C, no significant structural changes were observed. However, at 600 °C, a rapid thinning of cobalt layers commenced, due to intensive surface diffusion of cobalt.

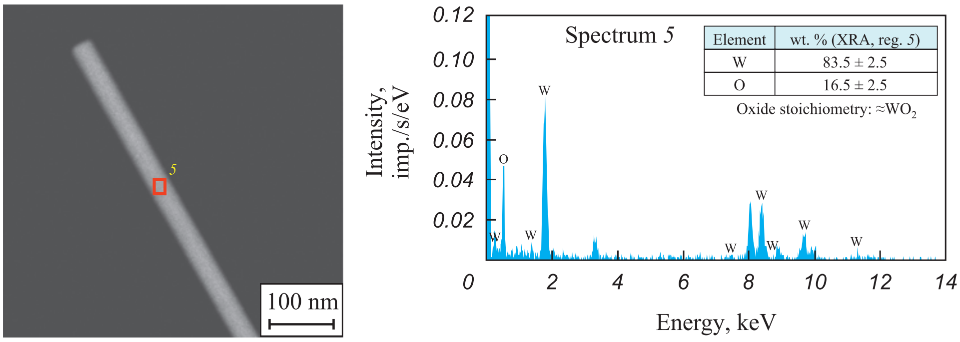

Fig. 9. EPMA results of oxide particles formed at the edge of the WC–6 %Co–0.2 %TaC lamella after heating to 600 °C

Рис. 9. Результаты МРСА оксидных частиц, сформировавшихся на краях ламели из твердого сплава WC–6 %Co–0,2 %TaC после нагрева до 600 °C

Simultaneously, the formation of nanosized particles of the Co_3W_3C phase, with sizes ranging from 5 to 20 nm, was documented within the binder. This formation can be attributed to a shift in the equilibrium phase composition of the carbide, shifting it from a two-phase region to a three-phase region as a consequence of the lamella's oxidation.

References / Список литературы

1. Östberg G., Buss K., Christensen M., Norgren S., Andrén H.-O., Mari D., Wahnström G., Reineck I. Mechanisms of plastic deformation of WC–Co and Ti(C, N)–WC–Co. *International Journal of Refractory Metals and Hard Materials*. 2006;4(1-2):135–144.
https://doi.org/10.1016/j.ijrmhm.2005.04.009

2. Lay S., Hamar-Thibault S., Lackner A. Location of VC in VC, Cr_3C_2 codoped WC–Co cermets by HREM and EELS. *International Journal of Refractory Metals and Hard Materials*. 2002;20(1):61–69.
https://doi.org/10.1016/S0263-4368(01)00071-3

3. Yamamoto T., Ikuhara Y., Watanabe T., Sakuma T., Taniuchi Y., Okada K., Tanase T. High resolution microscopy study in Cr_3C_2-doped WC–Co. *Journal of Materials Science*. 2001;36:3885–3890.
https://doi.org/10.1023/A:1017953701641

4. Jaroenwald A., Yamamoto T., Ikuhara Y., Sakuma T., Taniuchi T., Okada K., Tanase T. Segregation of vanadium at the WC/Co interface in VC-doped WC–Co. *Journal of Materials Research*. 1998;13(9):2450–2452.
https://doi.org/10.1557/JMR.1998.0341

5. Roebuck B., Gee M.G. TiC and Ti(C,N) cermet microstructures. In: *Proc. 12th Int. Plansee Seminar*. Eds. H. Bildstein, H.M. Ortner. Innsbruck, Tirol, 1989. Vol. 2. P. 1–29.

6. Viatte T., Bolognini S., Cutard T., Feusier G., Mari D., Benoit W. Investigation into the potential of a composite combining toughness and plastic deformation resistance. *International Journal of Refractory Metals and Hard Materials*. 1999;17(1-3):79–89.
https://doi.org/10.1016/S0263-4368(98)00044-4

7. Cutard T., Bolognini S., Feusier G., Verdon C., Viatte T., Benoit W. Microstructure and mechanical properties of Ti(C, N)–Mo_2C–(Ni, Co) cermets as a function of their initial chemical composition. *Key Engineering Materials*. 1997;132–136:747–750.
https://doi.org/10.4028/www.scientific.net/KEM.132-136.747

8. Feusier G., Cutard T., Verdon C., Viatte T., Benoit W. High temperature properties of TiCN–Mo_2C–Co cermets studied by mechanical spectroscopy. *Journal de Physique IV*. 1996;6:C8-751–C8-754.
https://doi.org/10.1051/jp4:19968163

9. Bolognini S., Feusier G., Mari D., Viatte T., Benoit W. High temperature mechanical behaviour of Ti(C, N)–Mo–Co cermets. *International Journal of Refractory Metals and Hard Materials*. 1998;16(4-6):257–268.
https://doi.org/10.1016/S0263-4368(98)00033-X

10. Viatte T., Cutard T., Feusier G., Benoit W. High temperature mechanical properties of Ti(C, N)–Mo_2C–Ni cermets studied by internal friction measurements. *Journal de Physique IV*.1996;6:C8-743–C8-746.
https://doi.org/10.1051/jp4:19968161

11. Qiu H., Li X., Pan C., Fan J., Qu S. Effect of Mo_2C addition on the formation of core-rim structure and mechanical properties of Ti(C, N)–WC–Mo_2C–(Ni, Co) cermet. *Journal of Materials Research and Technology*. 2023;25:750–762.
https://doi.org/10.1016/j.jmrt.2023.05.224

12. Östberg G., Buss K., Christensen M. Norgren S., Andrén H.-O., Mari D., Wahnström G., Reineck I. Effect of TaC on plastic deformation of WC–Co and Ti(C, N)–WC–Co. *International Journal of Refractory Metals and Hard Materials*. 2006;24(1-2):145–154.
https://doi.org/10.1016/j.ijrmhm.2005.04.010

13. Mahmoodan M., Aliakbarzadeh H., Gholamipour R. Microstructural and mechanical characterization of high energy ball milled and sintered WC–10 wt.%Co–*x*TaC nano powders. *International Journal of Refractory Metals and Hard Materials*. 2009;27:801–805.
https://doi.org/10.1016/j.ijrmhm.2009.02.001

14. Zaitsev A.A., Korotitskiy A.V., Levashov E.A., Avdeenko E.N. Compressive creep of coarse-grain WC–Co and WC–TaC–Co hardmetals with uniform microstructure comprising rounded WC grains. *Materials Science and Engineering: A*. 2020;795:139998.
https://doi.org/10.1016/j.msea.2020.139998

15. Buitrago J.D.R., Plazas A.F.G., Quintero L.K.H. Influence of TiC and Cr_3C_2 additions on the mechanical properties of a (W–Ti–Cr)C–Co sintered hardmetal. *Journal of Materials Research and Technology*. 2019;8(6):5736–5744.
https://doi.org/10.1016/j.jmrt.2019.09.042

16. Exner H.E. Physical and chemical nature of cemented carbides. *International Metals Reviews*. 1979;24(1):149–173.
https://doi.org/10.1179/imtr.1979.24.1.149

17. Rolander U., Weinl G., Zwinkels M. Effect of Ta on structure and mechanical properties of (Ti,Ta,W)(C,N)–Co cermets. *International Journal of Refractory Metals and Hard Materials*. 2001;19(4-6):325–328.
https://doi.org/10.1016/S0263-4368(01)00042-7

18. Upadhyaya G.S. Materials science of cemented carbides – An overview. *Materials and Design*. 2001;22(6):483–489.
https://doi.org/10.1016/S0261-3069(01)00007-3

19. Farag S., Konyashin I., Ries. B. The influence of grain growth inhibitors on the microstructure and properties of submicron, ultrafine and nano-structured hardmetals – A review. *International Journal of Refractory Metals and Hard Materials*. 2017;77:12–30.
https://doi.org/10.1016/j.ijrmhm.2018.07.003

20. Li N., Zhang W., Du Y., Xie W., Wen G., Wang S. A new approach to control the segregation of (Ta, W)C cubic phase in ultrafine WC–10Co–0.5Ta cemented carbides. *Scripta Materialia*. 2015;100:48–50.
https://doi.org/10.1016/j.scriptamat.2014.12.009

21. Nili H., Kalantar-zadeh K., Bhaskaran M., Sriram S. *In situ* nanoindentation: Probing nanoscale multifunctionality. *Progress in Materials Science*. 2013;58(1):1–29.
https://doi.org/10.1016/j.pmatsci.2012.08.001

22. Taheri M.L., Stach E.A., Arslan I., Crozier P.A., Kabius B.C., LaGrange T., Minor A.M., Takeda S., Tanase M., Wagner J.B., Sharma R. Current status and future direc-

tions for *in situ* transmission electron microscopy. *Ultramicroscopy*. 2016;170:86-95.
https://doi.org/10.1016/j.ultramic.2016.08.007

23. Yoreo J.J.De. In-situ liquid phase TEM observations of nucleation and growth processes. *Progress in Crystal Growth and Characterization of Materials*. 2016;62(2):69–88.
https://doi.org/10.1016/j.pcrysgrow.2016.04.003

24. Song Z., Xie Z.-H. A literature review of in situ transmission electron microscopy technique in corrosion studies. *Micron*. 2018;112:9–83.
https://doi.org/10.1016/j.micron.2018.04.011

25. Chen L.J., Wu W.W. In situ TEM investigation of dynamical changes of nanostructures. *Materials Science and Engineering: R: Reports*. 2010;70(3-6):303–319.
https://doi.org/10.1016/j.mser.2010.06.014

26. Bhushan B., Kulkarni A.V., Bonin W., Wyrobek J.T. Nanoindentation and picoindentation measurements using a capacitive transducer system in atomic force microscopy. *Philosophical Magazine A*. 1996;74(5):1117–1128.
https://doi.org/10.1080/01418619608239712

27. Oliver W.C., Pharr G.M. An improved technique for determining hardness and elastic modulus using load and displacement sensing indentation experiments. *Journal of Materials Research*. 1992;7:1564–1583.
https://doi.org/10.1557/JMR.1992.1564

28. Konyashin I., Ries B., Lachmann F. Near-nano WC–Co hardmetals: will they substitute conventional coarse-grained mining grades? *International Journal of Refractory Metals and Hard Materials*. 2010;28(4):489–497.
https://doi.org/10.1016/j.ijrmhm.2010.02.001

29. Zaitsev A.A., Konyashin I., Loginov P.A., Levashov E.A., Orekhov A.S. Radiation-enhanced high-temperature cobalt diffusion at grain boundaries of nanostructured hardmetal. *Materials Letters*. 2021;294:129746.
https://doi.org/10.1016/j.matlet.2021.129746

Information about the

Alexander A. Zaitsev – Cand. Sci. (Eng.), Senior Research Scientist of the Laboratory “*In situ* diagnostics of structural transformations”, National University of Science and Technology “MISIS” (NUST MISIS)
ORCID: 0000-0001-6934-9137
E-mail: aazaitsev@bk.ru

Pavel A. Loginov – Cand. Sci. (Eng.), Senior Research Scientist of the Laboratory “*In situ* diagnostics of structural transformations”, NUST MISIS
ORCID: 0000-0003-2505-2918
E-mail: pavel.loginov.misis@list.ru

Evgeny A. Levashov – Dr. Sci. (Eng.), Prof., Acad. of the Russian Academy of Natural Science, Head of the Department of Powder Metallurgy and Functional Coatings of NUST MISIS, Head of the Scientific-Educational Centre of SHS of MISIS–ISMAN
ORCID: 0000-0002-0623-0013
E-mail: levashov@shs.misis.ru

Authors Сведения об авторах

Александр Анатольевич Зайцев – к.т.н., ст. науч. сотрудник лаборатории «*In situ* диагностика структурных превращений» Национального исследовательского технологического университета «МИСИС» (НИТУ МИСИС)
ORCID: 0000-0001-6934-9137
E-mail: aazaitsev@bk.ru

Павел Александрович Логинов – к.т.н., ст. науч. сотрудник лаборатории «*In situ* диагностика структурных превращений» НИТУ МИСИС
ORCID: 0000-0003-2505-2918
E-mail: pavel.loginov.misis@list.ru

Евгений Александрович Левашов – д.т.н., проф., акад. РАЕН, заведующий кафедрой порошковой металлургии и функциональных покрытий НИТУ МИСИС, директор Научно-учебного центра СВС МИСИС–ИСМАН
ORCID: 0000-0002-0623-0013
E-mail: levashov@shs.misis.ru

Contribution of the Authors

A. A. Zaitsev – conceptualization of the research, defining study objectives, writing the article, and formulating conclusion.

P. A. Loginov – conducted calculations and performed sample testing.

E. A. Levashov – contributed to the conceptualization of the research, defining study objectives, writing the article, and formulating conclusion.

Вклад авторов

А. А. Зайцев – формирование основной концепции, постановка цели и задачи исследования, подготовка текста, формулировка выводов.

П. А. Логинов – осуществление расчетов, проведение испытаний образцов.

Е. А. Левашов – формирование основной концепции, подготовка текста, формулировка выводов.

Received 24.05.2023
Revised 19.09.2023
Accepted 28.09.2023

Статья поступила 24.05.2023 г.
Доработана 19.09.2023 г.
Принята к публикации 28.09.2023 г.

УДК 621.762; 62-408.2

https://doi.org/10.17073/1997-308X-2023-4-51-58

Научная статья
Research article

Электроискровое осаждение покрытий Fe–Cr–Cu на сталь Ст3

А. А. Бурков ✉, М. А. Кулик

Институт материаловедения Хабаровского федерального исследовательского центра
Дальневосточного отделения РАН
Россия, 680042, г. Хабаровск, ул. Тихоокеанская, 153

✉ burkovalex@mail.ru

Аннотация. Известно, что хром в составе металлических композиций формирует плотные пассивирующие пленки, замедляющие коррозию. Новое Fe–Cr–Cu-покрытие осаждено на сталь Ст3 электроискровой обработкой в анодной смеси, состоящей из медных и титановых гранул с добавлением порошка хрома в количестве от 4,85 до 13,26 мас. %. Привес катода увеличивался почти двукратно с ростом добавки порошка хрома в анодную смесь. Структуру покрытий исследовали методами рентгенофазового анализа, сканирующей электронной микроскопии и энергодисперсионной спектрометрии. Фазовый состав покрытий представлен феррохромом и медью. Показано, что предложенная методика электроискровой обработки позволяет получать Fe–Cr–Cu-покрытия со средней концентрацией хрома от 55 до 83 ат. %. Среднее содержание меди в приготовленных покрытиях находилось в диапазоне от 5 до 16 ат. %. Наибольшая концентрация хрома наблюдалась в покрытии, приготовленном с добавкой 13,26 мас. % Cr в анодную смесь. Коррозионное поведение покрытий исследовали методами потенциодинамической поляризации и импедансной спектроскопии в 3,5 %-ном растворе NaCl. Поляризационные испытания показали, что нанесение Fe–Cr–Cu-покрытий на сталь Ст3 позволяет повысить ее коррозионный потенциал от 12 до 19 % и снизить ток коррозии от 1,5 до 3,4 раза. Микротвердость поверхности покрытий составляла от 3,08 до 4,37 ГПа, а коэффициент трения – от 0,75 до 0,91. Максимальная твердость и наименьший коэффициент трения наблюдались у покрытия с наибольшим содержанием хрома. Показано, что Fe–Cr–Cu-покрытия позволяют улучшить износостойкость поверхности стали Ст3 от 1,5 до 3,8 раз.

Ключевые слова: покрытия Fe–Cr–Cu, электроискровое легирование, сталь Ст3, плотность тока коррозии, коэффициент трения, твердость, износ

Благодарности: Работа выполнена в рамках государственного задания Министерства науки и высшего образования Российской Федерации № 075-01108-23-02 (тема № 123020700174-7 «Создание и исследование новых металлических, керамических, интерметаллидных, композиционных материалов и наноструктурных покрытий с высокими физико-химическими и эксплуатационными свойствами»).

Для цитирования: Бурков А.А., Кулик М.А. Электроискровое осаждение покрытий Fe–Cr–Cu на сталь Ст3. *Известия вузов. Порошковая металлургия и функциональные покрытия*. 2023;17(4):51–58. https://doi.org/10.17073/1997-308X-2023-4-51-58

Electrospark deposition of Fe–Cr–Cu coatings on St3 steel

A. A. Burkov ✉, M. A. Kulik

Institute of Materials Science of the Khabarovsk Federal Research Center
of the Far Eastern Branch of the Russian Academy of Sciences
153 Tikhookeanskaya Str., Khabarovsk 680042, Russia

✉ burkovalex@mail.ru

Abstract. It is well-known that chromium in metallic compositions forms dense passivating films that slow down corrosion. The new Fe–Cr–Cu coating was applied on St3 steel through electrospark deposition in an anode mixture consisting of copper and titanium granules, with the addition of chromium powder ranging from 4.85 to 13.26 wt. %. The weight gain of the cathode increased nearly twofold with the addition of chromium powder to the anode mixture. The structure of the coatings was analyzed through *X*-ray phase analysis, scanning electron microscopy, and energy dispersive spectrometry. The phase composition of the coatings consists of ferrochrome and copper. It is demonstrated that the proposed method of electrospark processing allows for the creation of Fe–Cr–Cu coatings with an average chromium concentration ranging from 55 to 83 at. %. The average copper content in the prepared coatings varied from 5 to 16 at. %. The highest concentration of chromium was observed in the coating prepared with the addition of 13.26 wt. % Cr to the anodic mixture. The corrosion behavior of the coatings was investigated using potentiodynamic polarization and impedance spectroscopy in a 3.5 % NaCl solution. Polarization tests have shown that applying Fe–Cr–Cu coatings to St3 steel can increase its corrosion potential by 12 to 19 % and reduce the corrosion current by 1.5 to 3.4 times. The microhardness of the coating surface ranged from 3.08 to 4.37 GPa, and the coefficient of friction ranged from 0.75 to 0.91. The maximum hardness and the lowest coefficient of friction were observed in the coating with the highest chromium content. It has been demonstrated that Fe–Cr–Cu coatings can enhance the wear resistance of the surface of St3 steel by 1.5 to 3.8 times.

Keywords: Fe–Cr–Cu coatings, electrospark deposition, St3 steel, corrosion current density, coefficient of friction, hardness, wear

Acknowledgements: This research has received support from the Ministry of Science and Higher Education of the Russian Federation, Governmental contract No. 075-01108-23-02 “Development and study of innovative metallic, ceramic, intermetallic, composite materials and nanostructural coatings with superior physicochemical and operational properties”).

For citation: Burkov A.A., Kulik M.A. Electrospark deposition of Fe–Cr–Cu coatings on St3 steel. *Powder Metallurgy and Functional Coatings*. 2023;17(4):51–58. https://doi.org/10.17073/1997-308X-2023-4-51-58

Introduction

The economic damage caused by corrosion is estimated at approximately US$ 2.5 trillion, which is equivalent to 3.4 % of the world’s gross domestic product [1]. This figure does not include indirect losses associated with negative environmental impacts and the potential for emergency incidents [2]. As of 2014, China’s total spending on anti-corrosion measures reached US$ 152 billion, with the majority allocated to coatings (66.15 %) and surface treatment (13.24 %) [3]. In the Russian Federation, the annual loss of metals due to corrosion amounts to up to 12 % of the total mass of the metal stock, which corresponds to a loss of up to 30 % of the metal produced annually [4; 5].

It is well-known that the corrosion resistance of steels can be significantly improved by applying protective coatings [6]. Currently, the most widely used methods involve electroplating with chromium or nickel-chromium compositions. However, electroplated coatings exhibit poor adhesion and are susceptible to damage under harsh operating conditions, often resulting in local peeling of the chromium coating at the interface with the substrate [7]. Moreover, hexavalent chromium, which is used in electroplating, is classified as a hazardous substance. Air pollution from hexavalent chromium can lead to fatal diseases among plant employees, and severe wastewater contamination poses environmental risks, prompting several governments to restrict the use of electroplating [8].

Widespread magnetron sputtering methods are not well-suited for use with ferromagnetic materials due to poor plasma stability. In contrast to electroplating, electrospark deposition (ESD) offers superior adhesion of coatings because of the metallurgical bonding between the deposited material and the substrate. Chromium is commonly used to coat steels because it forms a passive Cr_2O_3 oxide on its surface, contributing to corrosion resistance [9; 10]. Moreover, Cr–Ti composite coatings show higher corrosion resistance compared to pure chromium or titanium coatings [11]. Furthermore, Cr–Ti composite coatings exhibit enhanced corrosion resistance when compared to pure chromium or titanium coatings [11]. However, it is known that even corrosion-resistant chromium alloys can experience localized corrosion due to bacteria-induces ennoblement [12]. On the other hand, the addition of more than 5 wt. % Cu to the alloy has been found to confer sustained antibacterial properties [13]. Consequently, adding copper to the Cr–Ti composite should provide it with antimicrobial capabilities and reduce the risk of corrosion caused by microbially induced ennoblement. Previously, we developed an automated ESD technique using a nonlocalized electrode, potentially matching the performance and energy efficiency of chromium plating [14; 15].

The objective of this study was to assess the suitability of ESD with a nonlocalized electrode for applying protective Fe–Cr–Cu coatings to St3 steel. Additionally, we aimed to investigate the impact of the concentration of chromium powder in the anode mixture on the structure, corrosion resistance, and tribological characteristics of the coatings.

Experimental

Copper and titanium granules were used in a molar ratio of 3:2 ($Cu_{60}Ti_{40}$) along with chromium powder with a purity of 98.5%, as the anode mixture. $Cu_{60}Ti_{40}$ granules was chosen as the sources of copper and titanium. These granules were created by cutting copper (M0) and titanium (VT-00) wires with a 4 mm diameter into pieces that were 4 ± 0.5 mm long. The chromium powder was pre-ground using a Retsch PM400 planetary mill (Retsch GmbH, Germany) in alcohol and an argon atmosphere at a speed of 250 min^{-1} for 80 min. The average size of chromium particles after grinding was 1.90 ± 0.98 µm. The amount of chromium added to the anode mixture varied from 4.85 to 13.26 wt. % (Table 1). The substrate (cathode) was made of St3 steel in the shape of a cylinder with a diameter of 12 mm and a height of 10 mm. The facility for depositing coatings using a nonlocalized anode with the addition of Cr_3C_2 powder is described in detail in [16]. The IMES-40 discharge pulse generator (Institute of Materials Science, Khabarovsk) generated rectangular current pulses with an amplitude of 110 A, 100 µs, 1000 Hz, and 40 V. To prevent oxidation of the sample surfaces, argon was supplied to the working volume of the container at a rate of 5 l/min.

The kinetics of mass transfer were studied by alternately weighing the cathode every 2 min using ESA on a Vibra HT120 analytical balance (Shinko Denshi, Japan) with an accuracy of 0.1 mg. The total processing time for one sample was 8 min. To ensure reproducibility of the results, the cathode weight gain was studied for three samples from each series.

The phase composition of the prepared coatings was analyzed using a DRON-7 *X*-ray diffractometer (NPP "Burevestnik", St. Petersburg) with CuK_α radiation in the angle range $2\theta = 20 \div 90°$. The microstructure of the coatings was examined using a Vega 3 LMH scanning electron microscope (SEM) (Tescan, Czech Republic) equipped with an X-max 80 energy dispersive spectrometer (EDS) (Oxford Instruments, UK).

The roughness of the coatings was measured using a TR 200 profilometer (TIME GROUP Inc., China).

Polarization tests were conducted in a three-electrode cell using a 3.5 % NaCl solution. A P-2X galvanostat (Electro Chemical Instruments, Chernogolovka) with a scanning speed of 4 mV/s was employed. A standard silver chloride electrode served as the reference electrode, and a paired platinum electrode ETP-02 was utilized as the counter electrode. Before recording, the samples were allowed to stabilize in the open circuit current for 30 min. The corrosion current density was determined from the plots using the Tafel extrapolation method. Impedance studies were carried out using a Z2000 device (Elins LLC, Moscow) within a frequency range of 100,000 to 1 Hz.

Table 1. **The composition of the anode mixture and the designation of coatings**

Таблица 1. **Состав анодной смеси и обозначение покрытий**

Designation	Ratio of metallic granules, at.%		Powdered chrome, wt. %
	Cu	Ti	
Cr5	60	40	4.85
Cr9			9.25
Cr13			13.26

The hardness of the coatings was measured using a PMT-3M microhardness tester (JSC LOMO, St. Petersburg) with a load of 0.5 N, employing the Vickers method. The wear resistance and coefficient of friction of the samples were assessed following the ASTM G99-17 procedure, involving dry sliding friction at a speed of 0.47 m/s under a load of 25 N. The testing time was set at 10 min, and high-speed steel M45 disks with a hardness of 60 HRC were employed as the counterbodies. Wear was evaluated gravimetrically, with each sample type subjected to at least three times.

Results and discussion

As the electrospark treatment time increased, the St3 steel cathode continuously gained weight, and the rate of weight gain significantly increased with the content of chromium powder in the anode mixture ranging from 4.85 to 9.25 wt. % (Fig. 1, *a*). With a larger quantity of Cr powder (from 9.25 to 13.26 wt. %), the weight gain of the substrates increased slightly, considering the margin of error. This observation suggests that the chromium powder content in the anode mixture is approaching an optimal value. In general, the cathode weight gain indicates that chromium powder can be successfully deposited on St3 steel using the ESD method with a $Cu_{60}Ti_{40}$ anode mixture.

X-ray diffraction patterns of the prepared coatings are displayed in Fig. 1, *b*. Reflections of ferrochrome Fe–Cr (#34-396 PDWin base) and copper (#4-836) are evident in the *X*-ray spectra of the coatings. Based on the intensities of the reflections, it is evident that the composition of the coatings was predominantly ferrochrome, which is a solid solution of chromium substituting for iron. This finding aligns with data from [17], where M50 steel was treated with the ESD method using a chromium electrode. The relative intensity of copper reflections in the *X*-ray spectra decreased with an increasing addition of chromium to the anode mixture, indicating a reduction in the copper concentration within the coatings.

The average thickness of the coatings increased within the range of 38.1 to 48.6 µm with an increasing addition of chromium to the anode mixture (Table 2). Figure 2, *a* displays an electron image of the cross-section of the Cr5 coating in the back-reflected electron mode. Within the coating's microstructure, there are light inclusions rich in copper (Fig. 2, *b*). These inclusions are likely the ones identified in the *X*-ray diffraction pattern. The coating exhibits a dense structure with a minimal number of small pores and inclusions

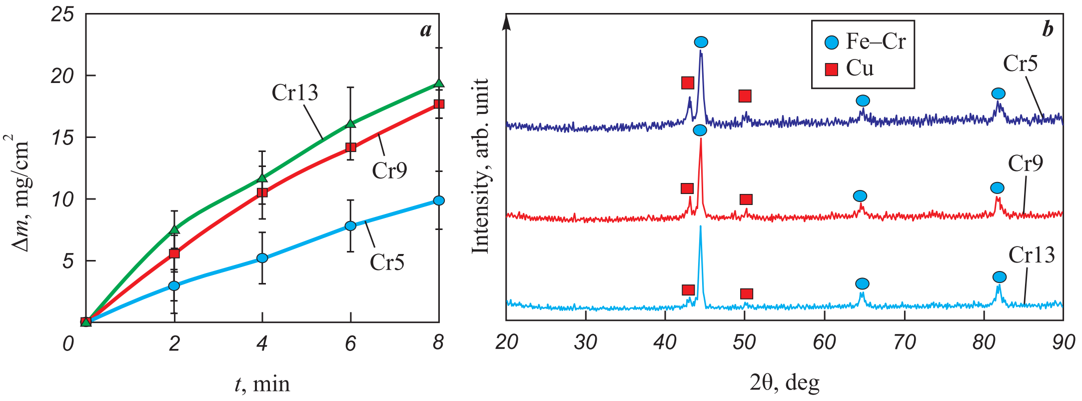

Fig. 1. The kinetics of cathode weight gain during the electrospark deposition of coatings (***a***) and *X*-ray diffraction patterns of the deposited coatings (***b***)

Рис. 1. Кинетика привеса катода при электроискровом нанесении покрытий (***a***) и рентгеновские дифрактограммы осажденных покрытий (***b***)

of copper oxides. The presence of copper oxides is a result of copper's high affinity for oxygen, even with the supply of argon to the container containing the granules. A significant accumulation of copper was found at the interface between the coating and the substrate (as shown in Fig. 2, *c*). This accumulation likely formed when a discharge occurred between the substrate and the copper granule at the outset of the ESD process.

The average chromium concentration in the coating composition ranged from 55 to 83 at. %. As the chromium content in the anodic mixture increased, its concentration in the coating exhibited a non-monotonic trend, with a minimum for the Cr9 sample and a maximum for the Cr13 sample (Fig. 3). Consequently, the average copper concentration in the coatings decreased from 16 to 5 at. %, reaching its maximum in the Cr9 sample.

The discrepancy between the data from *X*-ray phase analysis and energy dispersive analysis regarding the trend of changes in copper content with the addition of chromium to the anode mixture can be attributed to the fact that the concentration of chromium in the ferrochrome phase can vary widely. Additionally, the results obtained through the EDS method are generally considered more accurate compared to *X*-ray phase analysis. The average titanium content in the coatings ranged from 0.6 to 4 at. %. A comparison of copper and titanium data reveals that copper from the granules is

Table 2. **Characteristics of coatings**

Таблица 2. **Характеристики покрытий**

Sample	Thickness, μm	Roughness R_a, μm	Microhardness, GPa
Cr5	38.1 ± 12.2	3.82 ± 0.79	3.46 ± 0.44
Cr9	47.9 ± 6.0	4.63 ± 0.85	3.08 ± 0.26
Cr13	48.6 ± 5.4	4.04 ± 1.24	4.37 ± 0.46

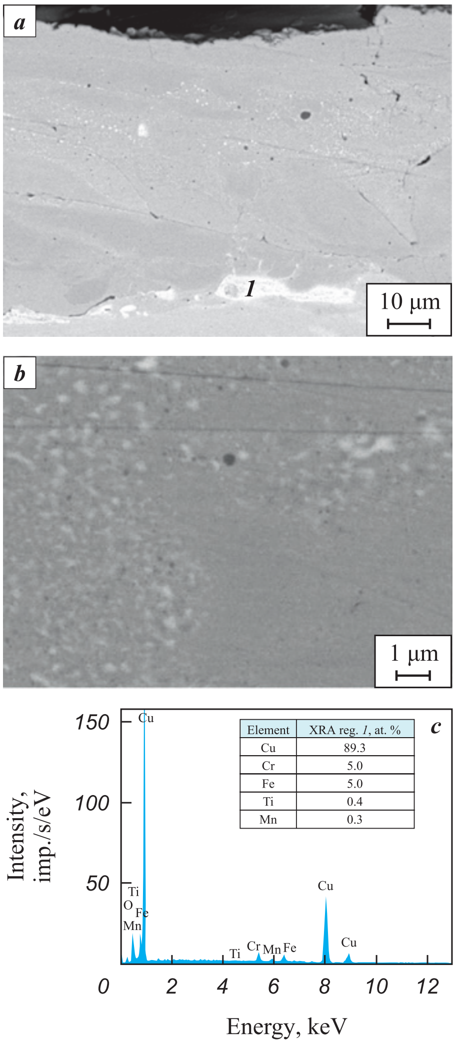

Element	XRA reg. *1*, at. %
Cu	89.3
Cr	5.0
Fe	5.0
Ti	0.4
Mn	0.3

Fig. 2. The SEM images of the Cr5 coating sample cross-section (***a***), its microstructure (***b***), and the EDS spectrum of a light inclusion (***c***)

Рис. 2. СЭМ-изображения поперечного сечения покрытия Cr5 (***a***), его микроструктура (***b***) и ЭДС-спектр светлого включения (***c***)

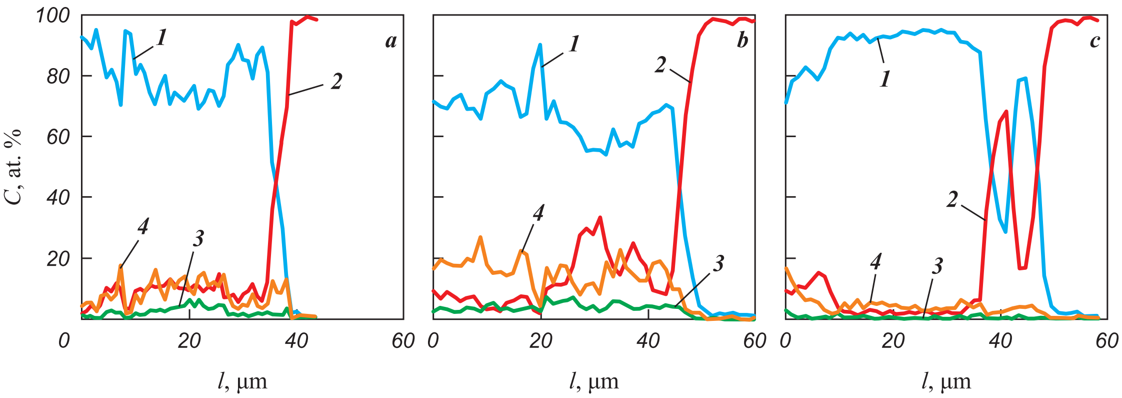

Fig. 3. The EDS analysis of elemental distribution along the coating cross-sections of samples Cr5 (***a***), Cr9 (***b***), and Cr13 (***c***)
1 – Cr, ***2*** – Fe, ***3*** – Ti, ***4*** – Cu

Рис. 3. Типичное распределение элементов по поперечному сечению покрытий Cr5 (***а***), Cr9 (***b***), Cr13 (***c***) согласно ЭДС-анализу
1 – Cr, ***2*** – Fe, ***3*** – Ti, ***4*** – Cu

much more actively transferred into the coating during ESD than titanium. This can be attributed to the higher melting point of titanium (1660 °C) when compared to copper (1083 °C).

An increase in the corrosion potential of St3 steel after coating indicates a reduction in its susceptibility to spontaneous corrosion (Fig. 4, *a*). To provide a detailed description of the corrosion behavior of the samples, the corrosion current density I_{corr} was calculated. The values of I_{corr} are in the range from 43.7 to 101.1 A/cm^2, as shown in Table 3. The corrosion current density varied inversely with the chromium concentration in the coatings, with a minimum for the Cr9 sample and a maximum for the Cr13 sample, mirroring the trend observed in the corrosion potential. The corrosion current density of the coatings was 1.47 to 3.39 times lower than that of St3 steel, despite the coatings' higher actual metal-to-electrolyte interface formed by the roughness of the coatings (see Table 2) in comparison to steel.

The electrical impedance spectra in a 3.5 % NaCl solution at room temperature are presented in Fig. 4, *b*. In this representation, the Im and Re axes represent the imaginary and real components of electrical impedance, respectively. The Nyquist diagrams for all coatings feature similar semicircular capacitive contours in the high-frequency region. Typically, a larger radius of the capacitive arc indicates higher corrosion resis-

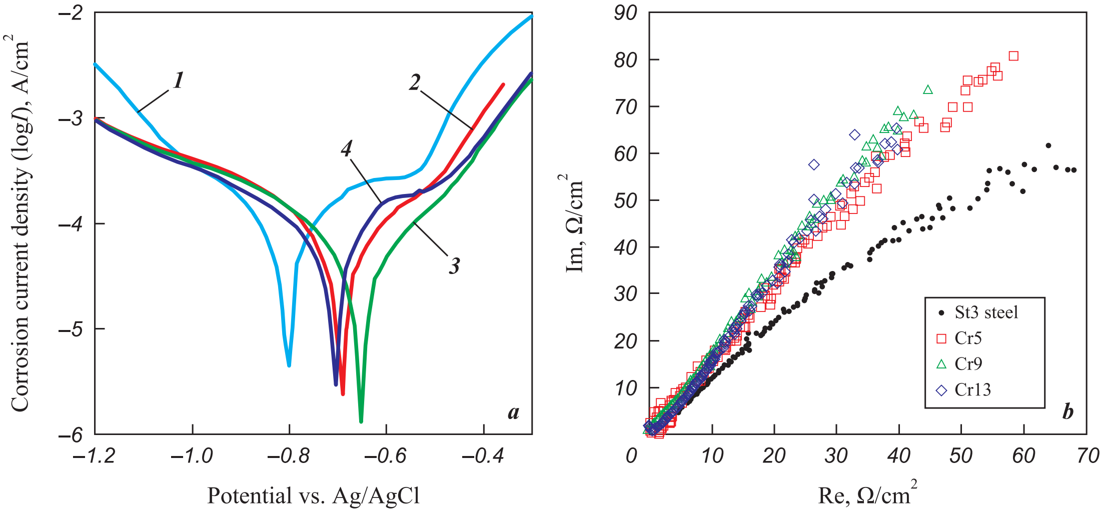

Fig. 4. The potentiodynamic polarization curves (***a***) and Nyquist plot (***b***) of Fe–Cr–Cu coatings and St3 steel
1 – steel St3, ***2*** – Cr5, ***3*** – Cr9, ***4*** – Cr13

Рис. 4. Потенциодинамические поляризационные кривые (***а***) и импедансные графики в координатах Найквиста (***b***) Fe–Cr–Cu-покрытий и стали Ст3
1 – сталь Ст3, ***2*** – Cr5, ***3*** – Cr9, ***4*** – Cr13

Table 3. **Corrosion potential and corrosion current density of coatings**

Таблица 3. **Коррозионный потенциал и ток коррозии покрытий**

Sample	E_{corr}, V	I_{corr}, μA/cm^2
St3	–0.80	148.3
Cr5	–0.69	64.9
Cr9	–0.65	43.7
Cr13	–0.70	101.1

tance of the material [18]. The radius of the capacitive circuit for all coatings was relatively close, but there was a tendency for it to increase with the addition of more chromium to the anode mixture. This implies that the corrosion resistance of Fe–Cr–Cu coatings improved with higher chromium concentrations. The radius of the capacitive circuit for St3 steel was notably smaller than that of the coatings, aligning with the potentiodynamic polarization data.

The microhardness measured at the surface of the coatings was consistent among all samples, ranging from 3.08 to 4.37 GPa (as shown in Table 2). As it is well-known, the microhardness of a coating is influenced by the phase composition and the distribution of residual stresses [19]. Chromium is known for its greater hardness compared to iron or copper. Consequently, the Cr9 coating with a low chromium concentration exhibited the lowest hardness, while the Cr13 coating with the highest chromium content displayed the highest hardness (see Fig. 3). Additionally, the increased hardness of the coatings was influenced by the refinement of the structure due to high cooling rates of the material after the ESD discharge completion [20]. Given that the hardness of St3 steel was 1.09 ± 0.2 GPa, the electrospark deposition of chromium can enhance the surface hardness by up to four times.

The average values of the coefficient of friction (*COF*) for the coatings ranged from 0.75 to 0.91 (Fig. 5, *a*). These higher *COF* values are in line with data from Fe–Cr coatings prepared through induction surfacing, where *COF* = 0.9 [21]. The coefficient of friction for the coatings was higher than that of St3 steel (*COF* = 0.63). Despite the relatively elevated *COF* level, the wear rate of the Fe–Cr–Cu coatings was 1.5 to 3.8 times lower than that of uncoated steel (Fig. 5, *b*). With an increasing chromium concentration in the anodic mixture, the wear of the electrospark coatings steadily increased from $1.88 \cdot 10^{-5}$ to $4.61 \cdot 10^{-5}$ mm^3/(N·m). This is likely due to the embrittlement of coatings as they become enriched with chromium, resulting in increased fluctuations in the friction force in the coefficient of friction curves for the Cr6 sample (Fig. 5, *a*).

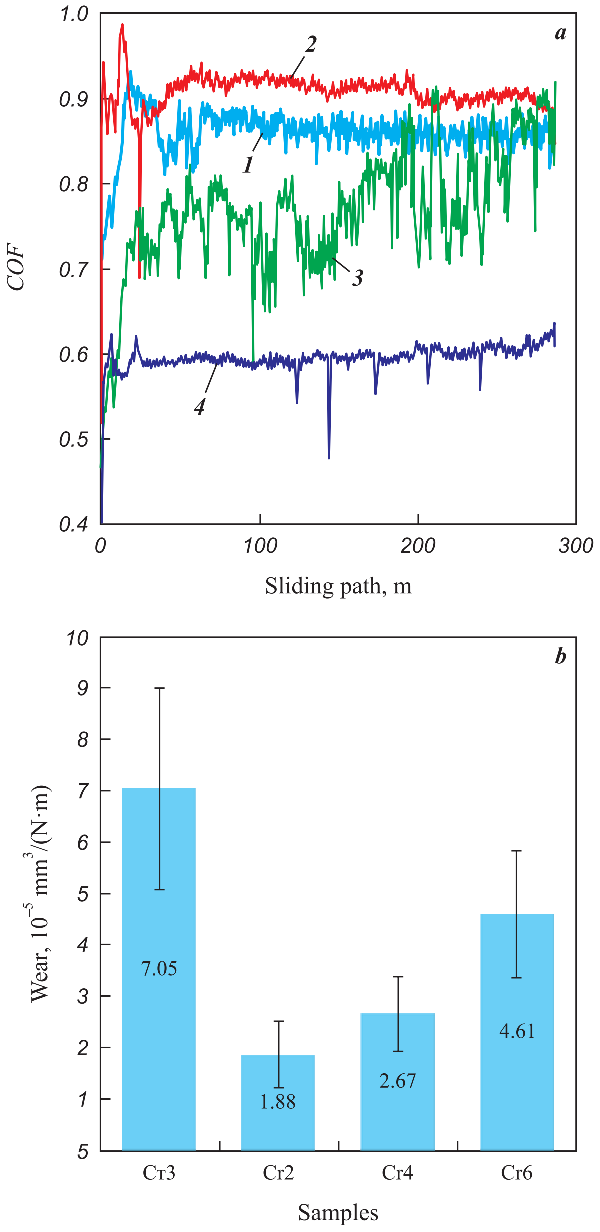

Fig. 5. The coefficient of friction (***a***) and wear (***b***) of coatings in comparison with St3 steel at a load of 25 N
1 – Cr2, ***2*** – Cr4, ***3*** – Cr6, ***4*** – steel St3

Рис. 5. Коэффициент трения (***а***) и износ (***b***) покрытий по сравнению со сталью Ст3 при нагрузке 25 Н
1 – Cr2, ***2*** – Cr4, ***3*** – Cr6, ***4*** – сталь Ст3

Conclusions

The method for depositing Fe–Cr–Cu coatings on St3 steel through electrospark treatment with a non-localized electrode in an anode mixture has been proposed. The anode mixture, consisting of copper and titanium granules supplemented with chromium powder ranging from 4.85 to 13.26 wt. %, allows for the production of coatings with chromium concentrations between 55 and 83 at. %. The coating with the highest chromium content was obtained when 13 wt. % of chromium was added to the anode mixture. The average copper content in the coatings varied from 5 to 16 at. %. Polarization tests revealed that applying Fe–Cr–Cu coatings to St3 steel can increase its corrosion potential by 12 to 19 % and reduce the corrosion current by 1.5 to 3.4 times. The microhardness of the coating surface ranged from 3.08 to 4.37 GPa, while the coefficient of friction fell within the range of 0.75 to 0.91. The highest hardness and the lowest coefficient of friction were observed in the coating with the highest chromium content. It's worth noting that wear of the coatings increased with the addition of chromium powder to the anode mixture.

References / Список литературы

1. Lazorenko G., Kasprzhitskii A., Nazdracheva T. Anticorrosion coatings for protection of steel railway structures exposed to atmospheric environments: A review. *Construction and Building Materials*. 2021;288:123115. https://doi.org/10.1016/j.conbuildmat.2021.123115
2. Kirchgeorg T., Weinberg I., Hörnig M., Baier R., Schmid M.J., Brockmeyer B. Emissions from corrosion protection systems of offshore wind farms: Evaluation of the potential impact on the marine environment. *Marine Pollution Bulletin*. 2018;136:257–268. https://doi.org/10.1016/j.marpolbul.2018.08.058
3. Hou B., Li X., Ma X., Cuiwei D., Zhang D., Zheng M., Xu W., Lu D., Ma F. The cost of corrosion in China. *npj Materials Degradation*. 2017;1(1):1–10. https://doi.org/10.1038/s41529-017-0005-2
4. Semenova I.V., Florianovich G.M., Khoroshilov A.V. Corrosion and corrosion protection. Moscow: Fizmatlit, 2002. 336 p. (In Russ.).

   Семенова И.В., Флорианович Г.М., Хорошилов А.В. Коррозия и защита от коррозии. М.: Физматлит, 2002. 336 с.
5. Elizar'ev A.N., Aksenov S.G., Sarvarov T.M., Mikhailov S.A., Sinagatullin F.K., Elizar'eva E.N., Epimakhov N.L. Ensuring environmental and industrial safety at tank farms of oil refining enterprises. *International Research Journal*. 2022;117(3):32–37. (In Russ.).

   Елизарьев А.Н., Аксенов С.Г., Сарваров Т.М., Михайлов С.А., Синагатуллин Ф.К., Елизарьева Е.Н., Эпимахов Н.Л. Обеспечение экологической и промышленной безопасности на резервуарных парках нефтеперерабатывающих предприятий. *Международный научно-исследовательский журнал*. 2022;117(3-1):32–37. https://doi.org/10.23670/IRJ.2022.117.3.005
6. Knyazeva Zh.V., Yudin P.E., Petrov S.S., Maksimuk A.V. Application of metallization coatings for protection of submersible electric motors of pumping equipment from influence of complicating factors in oil wells. *Powder Metallurgy and Functional Coatings*. 2020;(1):75–86. (In Russ.). https://doi.org/10.17073/1997-308X-2020-75-86

   Князева Ж.В., Юдин П.Е., Петров С.С., Максимук А.В. Применение металлизационных покрытий для защиты погружных электродвигателей насосного оборудования от воздействия осложняющих факторов в нефтяных скважинах. *Известия вузов. Порошковая металлургия и функциональные покрытия*. 2020;(1):75–86. https://doi.org/10.17073/1997-308X-2020-75-86
7. Li H., Chen G., Zhang G., Zhang K., Luo G. Characteristics of the interface of a laser-quenched steel substrate and chromium electroplate. *Surface and Coatings Technology*. 2006;201:902–907. https://doi.org/10.1016/j.surfcoat.2006.01.011
8. Babu B.R., Bhanu S.U., Meera K.S. Waste minimization in electroplating industries: A review. *Journal of Environmental Science and Health. Part C*. 2009;27(3):155–177. https://doi.org/10.1080/10590500903124158
9. Malyshev V.V., Shakhnin D.B. Titanium coating on carbon steel: direct-current and impulsive electrodeposition. Physicomechanical and chemical properties. *Materials Science*. 2014;50(1):80–91. https://doi.org/10.1007/s11003-014-9694-7
10. Ramezani-Varzaneh H.A., Allahkaram S.R., Isakhani-Zakaria M. Effects of phosphorus content on corrosion behavior of trivalent chromium coatings in 3.5 wt.% NaCl solution. *Surface and Coatings Technology*. 2014; 244:158–165. https://doi.org/10.3390/coatings9090531
11. Bahrami A., Delgado A., Onofre C., Muhl S., Rodil S.E. Structure, mechanical properties and corrosion resistance of amorphous Ti–Cr–O coatings. *Surface and Coatings Technology*. 2019;374:690–699. https://doi.org/10.1016/j.surfcoat.2019.06.061
12. Trigodet F., Larché N., Morrison H.G., Maignien L., Thierry D. Influence of dissolved oxygen content on the bacteria-induced ennoblement of stainless steels in seawater and its consequence on the localized corrosion risk. *Materials and Corrosion*. 2019;70(12):2238–2246. https://doi.org/10.1002/maco.201911225
13. Zhang E., Li.S., Ren J., Zhang L., Han Y. Effect of extrusion processing on the microstructure, mechanical properties, biocorrosion properties and antibacterial properties of Ti–Cu sintered alloys. *Materials Science and Engineering: C*. 2016; 69:760–768. https://doi.org/10.1016/j.msec.2016.07.051
14. Burkov A.A., Chigrin P.G. Effect of tungsten, molybdenum, nickel and cobalt on the corrosion and wear performance of Fe-based metallic glass coatings. *Surface and Coatings Technology*. 2018;351:68–77. https://doi.org/10.1016/j.surfcoat.2018.07.078
15. Burkov A.A., Krutikova V.O. Deposition of amorphous hardening coatings by electrospark treatment in a crystalline granule mixture. *Powder Metallurgy and Functional Coatings*. 2019;(2):57–67. (In Russ.). https://doi.org/10.17073/1997-308X-2019-2-57-67

    Бурков А.А., Крутикова В.О. Осаждение аморфных упрочняющих покрытий электроискровой обработкой в смеси кристаллических гранул. *Известия вузов. Порошковая металлургия и функциональные покрытия*. 2019;(2):57–67. https://doi.org/10.17073/1997-308X-2019-2-57-67
16. Burkov A.A., Kulik M.A. Wear-resistant and anticorrosive coatings based on chrome carbide Cr_7C_3 obtained by electric spark deposition. *Protection of Metals and Physical Chemistry of Surfaces*. 2020;56(6):1217–1221. https://doi.org/10.1134/S2070205120060064

17. Cao G., Zhang X., Tang G., Ma X. Microstructure and corrosion behavior of Cr coating on M50 steel fabricated by electrospark deposition. *Journal of Materials Engineering and Performance*. 2019;28(7):4086–4094.
https://doi.org/10.1007/s11665-019-04148-2

18. Li Y.C., Zhang W.W., Wang Y., Zhang X.Y., Sun L.L. Effect of spray powder particle size on the bionic hydrophobic structures and corrosion performance of Fe-based amorphous metallic coatings. *Surface and Coatings Technology*. 2022;437:128377.
https://doi.org/10.1016/j.surfcoat.2022.128377

19. Wang Q.Y., Xi Y.C., Zxao Y.H., Liu S., Bai S.L., Liu Z.D. Effects of laser re-melting and annealing on microstructure, mechanical property and corrosion resistance of Fe-based amorphous/crystalline composite coating. *Materials Characterization*. 2017;127:239–247.
https://doi.org/10.1016/j.matchar.2017.03.011

20. Shafyei H., Salehi M., Bahrami A. Fabrication, microstructural characterization and mechanical properties evaluation of Ti/TiB/TiB_2 composite coatings deposited on Ti6Al4V alloy by electro-spark deposition method. *Ceramics International*. 2020;46(10): 15276–15284.
https://doi.org/10.1016/j.ceramint.2020.03.068

21. Yu J., Liu Y., Song B., Wang J. Microstructure and properties of Fe-based alloy coating on gray cast iron fabricated using induction cladding. *Coatings*. 2020; 10(9):801.
https://doi.org/10.3390/coatings10090801

Information about the Authors

Aleksandr A. Burkov – Cand. Sci. (Phys.-Math.), Senior Researcher, Head of the Laboratory of Physical and Chemical Fundamentals of Materials and Technology, Institute of Materials Science of the Khabarovsk Federal Research Center of the Far Eastern Branch of the Russian Academy of Sciences
ORCID: 0000-0002-5636-4669
E-mail: burkovalex@mail.ru

Mariya A. Kulik – Junior Researcher of the Laboratory of Physical and Chemical Fundamentals of Materials and Technology, Institute of Materials Science of the Khabarovsk Federal Research Center of the Far Eastern Branch of the Russian Academy of Sciences
ORCID: 0000-0002-4857-1887
E-mail: marijka80@mail.ru

Сведения об авторах

Александр Анатольевич Бурков – к.ф.-м.н., ст. науч. сотрудник, заведующий лабораторией физико-химических основ технологии материалов, Институт материаловедения Хабаровского федерального исследовательского центра Дальневосточного отделения РАН
ORCID: 0000-0002-5636-4669
E-mail: burkovalex@mail.ru

Мария Андреевна Кулик – мл. науч. сотрудник лаборатории физико-химических основ технологии материалов, Институт материаловедения Хабаровского федерального исследовательского центра Дальневосточного отделения РАН
ORCID: 0000-0002-4857-1887
E-mail: marijka80@mail.ru

Contribution of the Authors

A. A. Burkov – formulated the concept of the article, reviewed publications, conducted experiments, processed and analyzed data, wrote the manuscript, and edited the text.
M. A. Kulik – studied the microhardness and structure of samples, searched for and analyzed published data, and contributed to manuscript design.

Вклад авторов

А. А. Бурков – идея статьи, литературный обзор, проведение экспериментов, обработка и анализ данных, подготовка текста.
М. А. Кулик – исследование микротвердости и структуры образцов, поиск и анализ литературных данных, редактирование текста, оформление статьи.

Received 21.12.2022
Revised 30.12.2022
Accepted 13.01.2023

Статья поступила 21.12.2022 г.
Доработана 30.12.2022 г.
Принята к публикации 13.01.2023 г.

Nanostructured Materials and Functional Coatings
Наноструктурированные материалы и функциональные покрытия

UDC 621.791.927.5 : 669.017.165

https://doi.org/10.17073/1997-308X-2023-4-59-70

Research article
Научная статья

Transformation of the nickel aluminide alloy structure through the application of a heat-resistant coating using oscillation electrode surfacing

I. V. Zorin ✉, V. I. Lysak, V. O. Kharlamov, S. A. Fastov

Volgograd State Technical University
28 Lenin Prosp., Volgograd 400005, Russia

✉ kewa991@yandex.ru

Abstract. This study considers the formation of an alloyed nickel aluminide structure through automatic electric arc surfacing employing an oscillating electrode composed of composite wire. The arc transversely traverses the weld pool surface at a frequency denoted as f. In comparison to conventional surfacing techniques, this process either displaces the crystallization front alongside the weld pool (at $f = 1.3$ Hz) or stabilizes it (at $f \geq 2$ Hz) throughout the cross-sectional area of the coating layer. We have conducted an investigation into the evolution of alloy structures resulting from surfacing. Notably, we have observed that the regions with concentrations of eutectic nickel-aluminum are particularly susceptible to structural alterations. The formation of particle clusters, which is contingent upon heat dissipation conditions near the crystallization front, leads to the development of layered texture regions. Our findings reveal that following 50 thermal cycles (heating to 1100 °C, cooling to 25 °C), the alloy's hardness becomes independent of subsequent thermal cycles, consistently maintaining a level 34–35 HRC. The highest resistance of the surfaced metal to thermal fatigue cracks is achieved when its structure exhibits an optimal γ-solid solution (relatively ductile) to nickel-aluminum cooling martensite ratio, corresponding to the Ni_2Al phase. The thermal conditions necessary for producing such a structure are elucidated by the gradual cooling of the crystallized metal from elevated temperatures when $f \geq 2.8$ Hz. An analysis of changes in oxidative wear, estimated by mass loss, during thermal fatigue tests conducted at a metal heating temperature of 1100 °C revealed the superiority of the studied alloy over industrial alloys based on nickel and cobalt.

Keywords: electric arc surfacing, oscillating electrode, nickel aluminide, thermal cycle, metal structure, thermal fatigue, oxidation resistance

Acknowledgements: This research received support from the Russian Science Foundation, Grant No. 23-13-00354 (https://rscf.ru/project/23-13-00354/).

For citation: Zorin I.V., Lysak V.I., Kharlamov V.O., Fastov S.A. Transformation of the nickel aluminide alloy structure through the application of a heat-resistant coating using oscillation electrode surfacing. *Powder Metallurgy and Functional Coatings*. 2023;17(4):59–70. https://doi.org/10.17073/1997-308X-2023-4-59-70

Трансформация структуры сплава на основе алюминида никеля в процессе наплавки колеблющимся электродом термостойкого покрытия

И. В. Зорин, В. И. Лысак, В. О. Харламов, С. А. Фастов

Волгоградский государственный технический университет
Россия, 400005, г. Волгоград, пр. им. В.И. Ленина, 28

kewa991@yandex.ru

Аннотация. Работа посвящена исследованию формирования структуры легированного алюминида никеля в процессе автоматизированной электродуговой наплавки колеблющимся электродом (плавящейся композиционной проволокой), при котором дуга совершает поперечные перемещения с частотой *f* по поверхности расплава сварочной ванны. Использование такого приема в сравнении с традиционной технологией наплавки позволяет перемещать вместе с расплавом сварочной ванны фронт кристаллизации (при *f* = 1,3 Гц) или стабилизировать его (при *f* ≥ 2 Гц) в поперечном сечении наплавляемого металла. Изучена эволюция структуры наплавленных сплавов. Установлено, что наиболее структурно чувствительной фазой являются участки сосредоточения никель-алюминиевой эвтектики, скопления частиц которой, в зависимости от условий теплоотвода вблизи фронта кристаллизации, образуют участки слоистой текстуры. Показано, что после 50 теплосмен (нагрев до 1100 °С, охлаждение до 25 °С) твердость исследуемого сплава перестает зависеть от последующего термического циклирования и сохраняется неизменной на уровне 34–35 HRC. Наибольшая стойкость наплавленного металла к появлению трещин термической усталости обеспечивается при формировании в его структуре близкого к оптимальному соотношения относительно вязкого, легированного железом и другими элементами γ-твердого раствора и никель-алюминиевого мартенсита, состав которого соответствует Ni_2Al-фазе. Термические условия получения такой структуры обусловлены замедленным охлаждением закристаллизовавшегося металла с высоких температур при достижении *f* ≥ 2,8 Гц. Анализ изменения сопутствующего термоусталостным испытаниям окислительного изнашивания (оцениваемого потерей массы) при температуре нагрева металла 1100 °С показал преимущества исследуемого сплава над промышленными сплавами на основе никеля и кобальта.

Ключевые слова: электродуговая наплавка, колеблющийся электрод, алюминид никеля, термический цикл, структура, термическая усталость, стойкость к окислению

Благодарности: Исследование выполнено за счет гранта Российского научного фонда № 23-13-00354 (https://rscf.ru/project/23-13-00354/).

Для цитирования: Зорин И.В., Лысак В.И., Харламов В.О., Фастов С.А. Трансформация структуры сплава на основе алюминида никеля в процессе наплавки колеблющимся электродом термостойкого покрытия. *Известия вузов. Порошковая металлургия и функциональные покрытия*. 2023;17(4):59–70. https://doi.org/10.17073/1997-308X-2023-4-59-70

Introduction

Developed during the mid-20th century, weld overlay represents an efficient technique for extending the operational lifespan of products exposed to temperatures as high as 1000 °C. To enhance the resistance of the cladding layer against high-temperature wear, iron, nickel, and cobalt alloys are commonly employed [1–3]. These alloys have undergone extensive research. Conversely, nickel aluminide-based heat-resistant alloys for surfacing have garnered substantial practical interest. Among these, Ni_3Al and NiAl intermetallics are particularly promising [4; 5].

Both domestic and international nickel aluminide casting alloys exhibit improved thermal stability [4; 6], elevated high-temperature and fatigue strength [7; 8], and resistance to high-temperature oxidation [4; 9]. Despite the significant potential of these alloys, their application in cladding is constrained due to the high sensitivity of nickel aluminide to heating and cooling rates, primarily owing to the elevated γ'-Ni_3Al phase content, which diminishes plasticity and hinders stress relief during welding [10]. Consequently, it is imperative to maintain a low-temperature gradient at the crystallization front in the weld pool. Meng Zhang et al. [11] have reported achieving a similar outcome by constructing a vertical “wall” of Ni_3Al alloy via a multilayer weld overlay technique under argon shielding, incorporating multiple reheating cycles by subsequent layers, and controlling the cooling rate (1–2 °C/s).

In contrast to the “gentle” thermal deformation cycle of argon arc surfacing using a non-consumable electrode, semi- or fully automated weld overlay employing a consumable electrode significantly enhances both productivity and the quality of the surfacing layer. However, as highlighted by Sorokin L. et al. [12], the conditions for metal structure formation become more complex due to the higher heat input and the larger melt pool volume, resulting in increased weld stress [12].

Various methods are currently employed to control heat input during welding processes. These methods encompass the use of pulse [13] and modulated [14] weld current, high-frequency oscillations of the electrode [15], or, as the most common and cost-effective approach, adjusting the specific welding energy. The control of specific energy can influence the size and shape of the weld pool and, consequently, the properties of the surfacing metal in the clad alloy. However, this control is effective only within specific ranges of welding arc power and weld deposit rates [16], which are contingent on the particular alloying system [17; 18]. For Ni–Cr cladding, a relatively wide range of weld overlay rates can be applied to manage phase composition and structure size while ensuring a defect-free surfacing layer. Nevertheless, for high-carbon and boron-containing wear-resistant alloys, the applicable range of rates is considerably narrower.

Several strategies have been devised to minimize the conversion of weld energy into heat input at the crystallization front. Wu Dongting et al. [19] suggested excluding the workpiece from the welding circuit. Another method involves employing transverse oscillations of the weld arc across the weld pool surface. This latter approach to heat input control offers greater flexibility and was originally investigated by G.G. Chernyshev, B.N. Kushnirenko, and M.M. Shtrikman in the 1960s and 1970s. Today, it finds application in multilayer wear-resistant surfacing [20]. Pre-eutectic and eutectic wear-resistant alloys with high chromium and carbon content exhibit more favorable responses to transverse electrode oscillations with specific frequencies and amplitudes [17; 21; 22]. In certain instances, repeated thermal effects are applied to the crystallizing metal as the weld arc moves, potentially altering the carbide phase morphology and grain size [23]. It has been postulated that utilizing an oscillating electrode for cladding an alloy containing eutectic phases of nickel aluminide is a preferred approach for controlling the thermal conditions of structure formation, thereby enhancing the thermal resistance of the surfacing layer.

The primary objective of this study is to characterize the structure of the nickel aluminide alloy formed during surfacing under the influence of repeated thermal effects on the cladding layer.

Materials and Methods

We employed electrodes crafted from composite wire (CW) with a diameter of 3 mm. This wire was manufactured through a 6-pass drawing process using a carbide die. The wire sheath consists of a nickel strip, while the wire filler comprises aluminum, tungsten, molybdenum, powdered tantalum, and chromium. This composite wire design (Fig. 1) ensures a uniform distribution of filler components along the length of the wire. In the case of powder wires, achieving such uniformity typically requires a layer-by-layer arrangement of filler components possessing similar physical and mechanical properties. The inherent inhomogeneity in thermophysical properties across the cross-section is a common characteristic of composite structures, yet this is mitigated by effective electrical contact between the surfaces of the composite wire components, facilitating rapid heating. Taking into account the loss of filler elements due to oxidation within the weld pool, the theoretical composition of the composite wire corresponds to a stoichiometric nickel-to-aluminum mass ratio ~6.5. The inclusion of refractory alloying elements such as tungsten, molybdenum, and tantalum

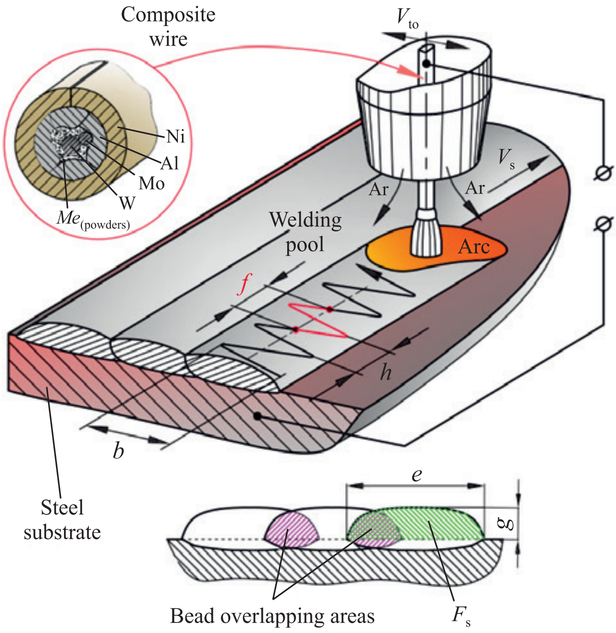

Fig. 1. Cladding process
f – frequency of the transverse arc oscillations over the weld pool; V_{to} – electrode transverse oscillation velocity; V_s – surfacing rate; h – surfacing increment; b – electrode amplitude; e – weld bead width; g – weld bead height; F_s – area of the surfaced part of the bead

Рис. 1. Схема формирования наплавленного покрытия
f – частота поперечных перемещений дуги по поверхности сварочной ванны; V_{to} – скорость колебаний электрода; V_s – скорость наплавки; h – шаг наплавки; b – размах колебаний электрода; e – ширина валика; g – высота валика; F_s – площадь наплавленной части валика

in the filler material strengthens the γ'-solid solid solution and enhances the stability of the γ'-phase at temperatures up to 1100 °C. Additionally, the surfacing layer contains a minimum of 4 wt. % chromium, which, when combined with aluminum, imparts robust resistance to high-temperature oxidation. As a substrate, we utilized plates measuring 12×80×170 mm, composed of the 5CrNiMn steel grade.

The resulting chemical composition (wt. %) of the nickel aluminide alloy is as follows:

Ni	Base metal	W	3.3–3.6
C	0.2–0.3	Mo	2.6–3.1
Al	8.2–8.5	Ta	2.3–2.5
Cr	4.0–4.2	Fe	12–15

Equally spaced VP 5/20 tungsten alloy thermocouples were installed within the steel substrate at depth of 1.5 mm below the surface. These thermocouples are designed to gauge the temperature at the base of the weld pool and in close proximity to the crystallization front as the base metal undergoes melting. The thermocouples were constructed using 0.6 mm diameter wire. In order to process the thermocouple signals, we utilized an LA-20USB multichannel ADC converter from Rudnev–Shilyaev, Moscow, and subsequently transferred the data to a PC. The PowerGraph™ software was employed to record the signals and generate temperature vs. time curves.

The melting point of the alloy, as determined by differential scanning calorimetry, is ~1386 °C. In order to further investigate the structure and elemental composition of the alloy, we employed an electron-ion microscope (FEI Versa 3D, USA).

In order to assess the cladding layer's resistance to thermal fatigue cracking, we conducted cyclic heating tests and monitored the number of heating-cooling cycles until the first fatigue cracks became evident. The samples, measuring 15×15×4 mm, consisted of single-layer cladding metal. Additionally, we fabricated test samples using Stoodite 6 and Hastelloy C clad alloys. These samples were then positioned within a furnace that was heated to a temperature of $t = 1100$ °C, held at this temperature for 6 min, and subsequently cooled down to $t = 25$ °C in 7–9 s. This testing protocol encompassed a total of 240 thermal cycles. In order to evaluate the oxidation resistance of the samples, we measured the mass loss of each sample after every 30 thermal cycles. These measurements were carried out using a VIBRA HT-124RCE analytical balance (Shinko Denshi Co. LTD, Japan) with a readability of 0.1 mg.

Surfacing Process

We employed an A2 Mini Master welding machine (ESAB, Sweden), which includes an electrode oscillation drive. The electrode oscillates transversely to the direction of the cladding. The oscillation drive converts the rotation of the gearmotor shaft into a reciprocating rectilinear motion of the lever connected to the electrode wire feeder. The velocity of the transverse oscillations of the electrode V_{to} spans from 16 to 50 mm/s. This velocity decreases to approximately 0.1 times V_{to} at the extremities of the electrode's oscillation amplitude (b).

The transverse oscillation velocity is synchronized with the linear surfacing velocity (V_s). Consequently, the surfacing increment (h) is automatically chosen by the welding machine to maintain the specified V_s value. An increase in V_{to} to ~50 mm/s results in a decrease in surfacing increment, causing the arc to reach the end of its transverse path within 1 s, and the oscillation frequency (f) approaches 3 Hz. Conversely, when V_{to} is reduced to 16 mm/s, the surfacing increment increases, and f shifts to its minimum value of ~1 Hz (see Fig. 1).

We introduced the weld bead shape factor (μ_b), defined as the ratio of the cross-sectional area of the bead to the area of a rectangle with dimensions equal to the bead width (e) and bead height (g) (see Fig. 1). For single-layer coatings, the bead-to-bead overlap varied in the range of 30–50 %, depending on μb. The steel substrate comprises 16–20 % of the surfacing layer.

In order to ensure superior weld bead quality, the surfacing velocity was set at 19 cm/min. Exceeding this value adversely affects the weld beads, resulting in inconsistencies in their shape, length, and width. As the surfacing velocity decreases (<10 m/h), the retraction of molten material into the tail of the weld pool is significantly reduced, leading to an expansion of the weld pool volume beneath the arc. This results in a shorter arc and disrupts the wire melting process. Arc stability (preventing short circuits in the arc gap with the refractory wire filler) is achieved at $U_{arc} = 27$ V. A welding current of $I_{weld} = 280 \pm 15$ A was selected to provide the arc thermal power sufficient to melt the refractory filler in the wire while preventing overheating of the drop at the wire end. Initially, the heat needed to keep the filler components in a molten state is supplied by the anode spot at the end of the refractory tungsten-molybdenum filler. When the melt entirely covers the refractory filler, the anode spot shifts to the end surface of the resulting drop. The drop separates as it descends along the surface of the partially molten filler. Following this, a new molten filler drop begins to form around it [24].

The welding current source (DC, reversed polarity) utilized was an LAF 1001 thyristor rectifier (ESAB, Sweden). The primary surfacing process variables include:

Welding current (*I*), A	280 ± 15
Arc voltage (*U*), V	27 ± 1
Oscillation amplitude (*b*), mm	10
Frequency of arc transverse oscillations (*f*), Hz	1.3; 2.0; 2.8
Surfacing velocity (V_s), cm/min	19 ± 1
Shielding gas (argon) flow rate, l/min	25–30

Results and discussion

The analysis of the metal's heating and cooling profile during arc cladding without transverse composite wire oscillations reveals a thermal cycle with a single peak (Fig. 2, *a*). This peak corresponds to the maximum temperature reached when the melt contacts the thermocouple junction. During the cooling stage near the crystallization temperature, the cooling rate is relatively high (~100 °C/s). Subsequently, starting from 1300 °C, the temperature decrease gradually slows down to ~20 °C/s. The resulting structure of the cladding layer, formed under such non-equilibrium conditions (Fig. 3, *a*), comprises two regions with roughly equal volume fractions. One of these regions consists of the alloyed γ-solid solution, characterized by primary crystallizable dendrites. The other region contains dispersed lamellar particles of the γ′-phase. As per the established concept of the Ni_3Al alloy structure and phase state, based on the work of Kolobov Yu. et al. [4], these particles are formed through the $L \leftrightarrow \gamma + \gamma'$ eutectic reaction.

Further analysis of the eutectic concentration areas reveals significant non-uniformity in the distribution of iron and aluminum between the two primary phases. The eutectic nickel-aluminum areas exhibit the highest concentrations of aluminum and nickel (Fig. 4, *a*, *b*). Given that iron can form a continuous solid solution with nickel, it is primarily dissolved in the γ-phase. The presence of iron in the γ′-phase can be attributed to its ability to substitute for both nickel and aluminum in Ni_3Al.

The transverse oscillations of the electrode (at a frequency of $f = 1.3$ Hz) lead to the appearance of multiple peaks on the cooling curve (see Fig. 2, *b*). These peaks correspond to short-term temperature fluctuations caused by reheating of the cooled metal by the arc. The pattern of the peaks for *1*, *2* and *3*

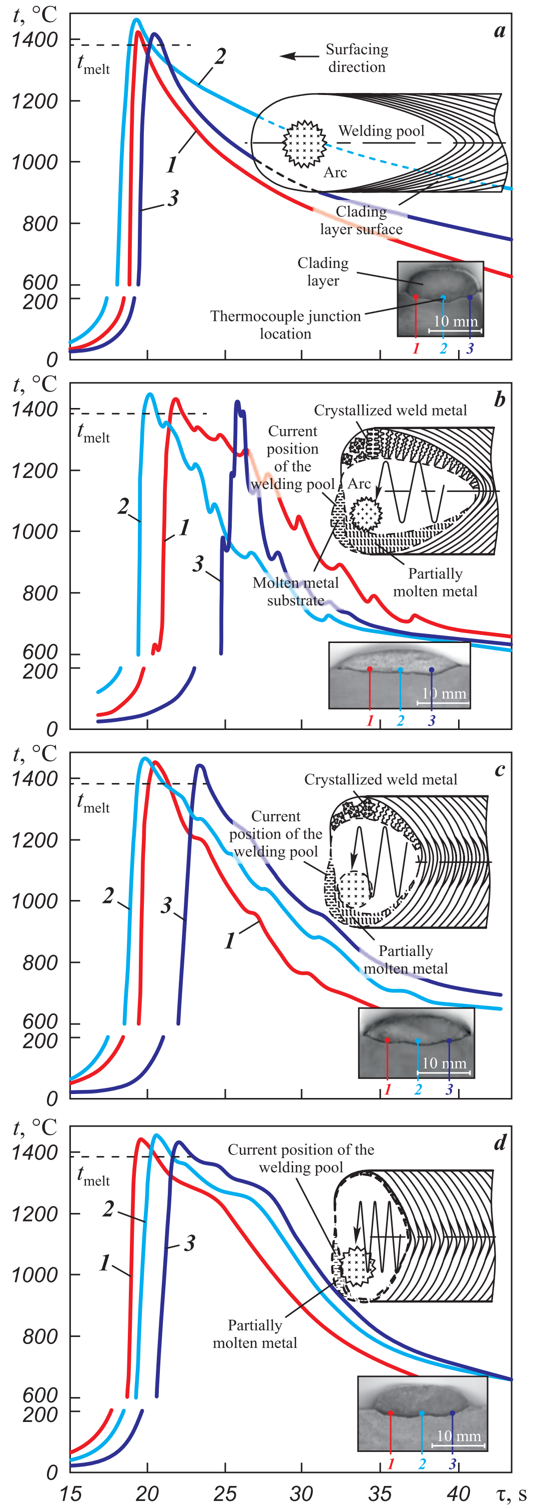

Fig. 2. Thermal cycles of the surfacing process without (***a***) and with electrode oscillations (***b***–***d***) at *f* = 1.3 Hz (***b***), 2 Hz (***c***), and 2.8 Hz (***d***)
1, ***2***, ***3*** are the temperature curves as recorded by the thermocouple junctions within the base metal

Рис. 2. Термические циклы процесса наплавки без колебаний электрода (***а***) и с перемещениями дуги по поверхности сварочной ванны (***b***–***d***) с частотой *f* = 1,3 Гц (***b***), 2 Гц (***c***), 2,8 Гц (***d***)
1, ***2***, ***3*** – кривые изменения температуры, соответствующие местам расположения спаев термопар в основном металле

thermal cycles indicate that the crystallizing metal experiences elevated temperatures for a limited duration. This phenomenon arises due to the cyclic redistribution of hot and cold areas within the weld pool as the pool moves in response to the transverse oscillations of the weld arc. However, when the weld pool tracks the heat source (the arc), it remelts the previously cooled metal, and crystallization recommences. This cyclic process results in a chaotic orientation of crystallite growth and the interweaving of crystallites, as observed in the lower and partially middle sections of the beads. The structure of the upper (working) bead (Fig. 3, *b*) displays a high degree of dispersion within the regions containing the eutectic γ′-phase. The size of such regions does not exceed 20 μm. The γ-solid solution areas contain small fractions of segregations, likely consisting of topologically close-packed (TCP) phases.

The morphological alterations within the γ′-phase induce a transformation from lamellar and sharply-angular particle clusters (typically found in alloys produced without electrode oscillations, Figs. 3, *a* and 4, *a*) into layered texture regions when oscillations occur at $f = 1.3$ Hz. Each layer within these regions exhibits a distinct crystallographic orientation. The weld bead created with an oscillating electrode is notably wider, ranging from 150 % to 170 % wider (as shown in Fig. 2, *b*), yet its μ_b value ($0.72 < 0.88$) is lower in comparison to the bead produced without oscillations.

Increasing frequency f to 2 Hz results in the anticipated reduction of both the weld pool and crystallization front lengths. This is corroborated by more similar heating and cooling curves observed at the thermocouple locations. The cooling rate decelerates, and the temperature peaks resulting from repeated heating due to arc oscillations become less pronounced (Fig. 2, c). These changes lead to the predominance of the γ-solid solution in the structure, with these regions interspersed by areas containing fragmented eutectic nickel-aluminum (Fig. 3, *c* and Fig. 4, *c*). The nickel-to-aluminum ratio in these regions falls below the stoichiometric ratio required for the formation of the γ′-Ni_3Al-phase (Fig. 4, *c*). The weld bead formed at $f = 2$ Hz exhibits a slightly higher weld bead shape factor (0.75) while maintaining a comparable width.

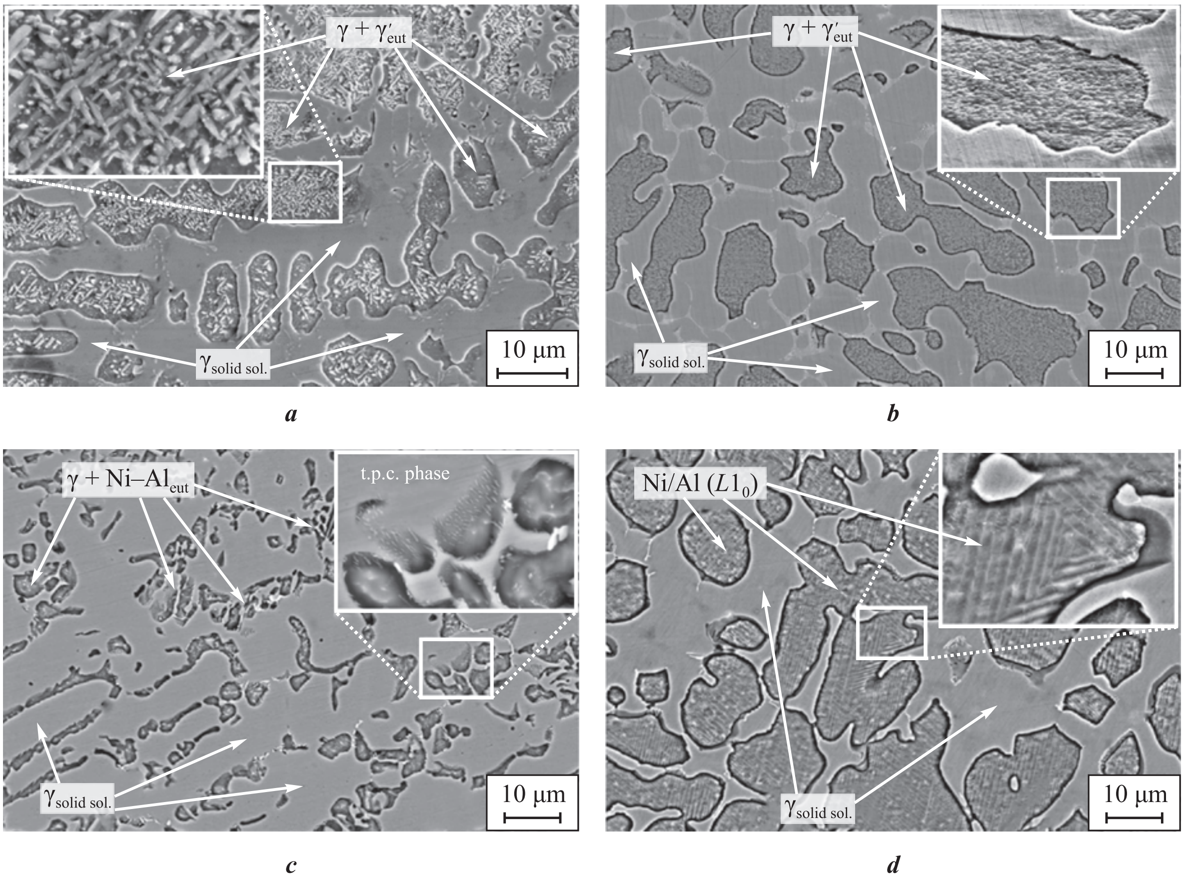

a ***b***

c ***d***

Fig. 3. Structures of the alloys surfaced without (***a***) and with electrode oscillations (***b–d***) at $f = 1.3$ Hz (***b***), 2 Hz (***c***), and 2.8 Hz (***d***)

Рис. 3. Структуры сплавов, наплавленных без колебаний электрода (***a***) и с перемещениями дуги по поверхности сварочной ванны (***b–d***) с частотой $f = 1{,}3$ Гц (***b***), 2 Гц (***c***), 2,8 Гц (***d***)

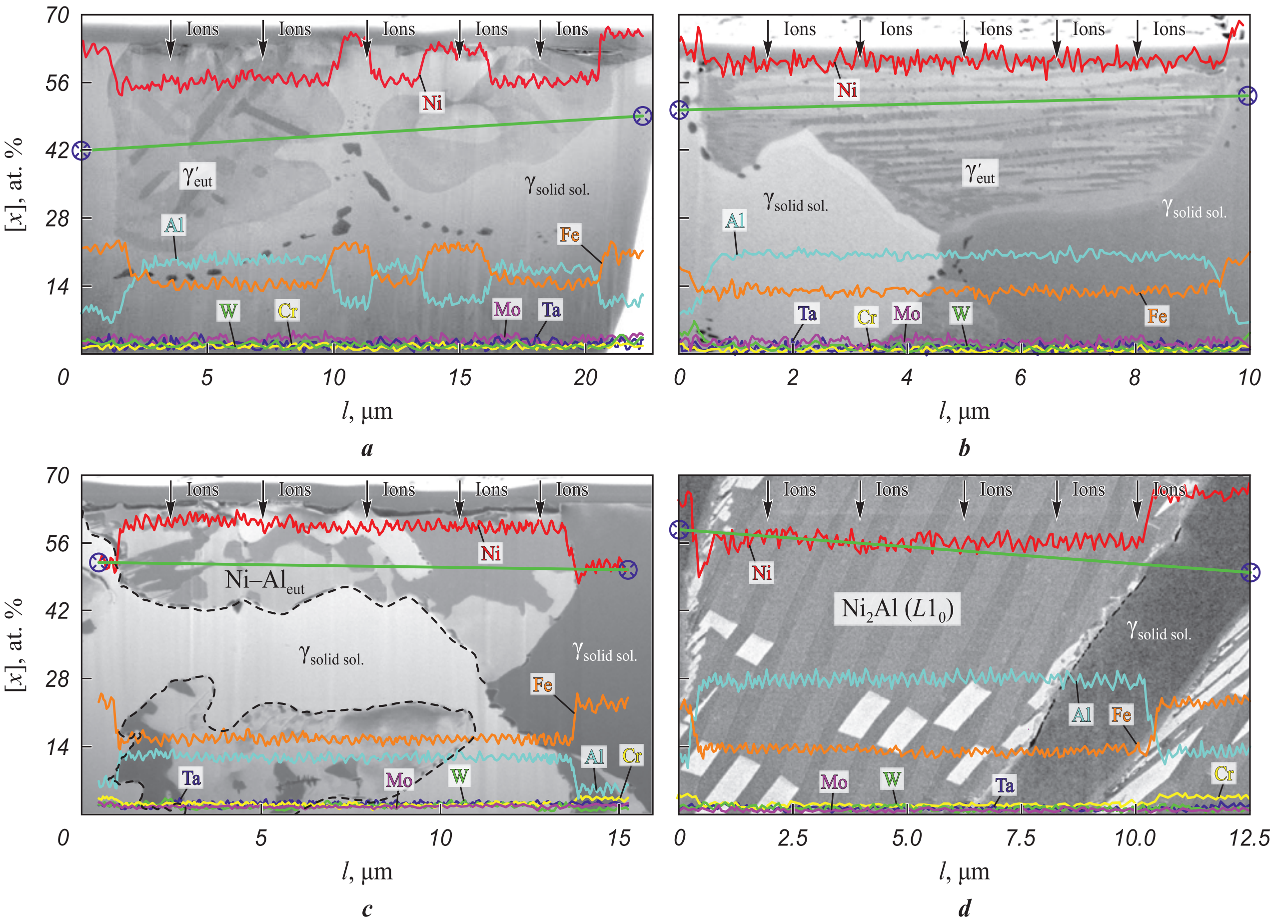

Fig. 4. Structure and elemental composition of the eutectic concentration areas after ion “etching” in the alloys surfaced without (***a***) and with electrode oscillations (***b–d***) at *f* = 1.3 Hz (***b***), 2 Hz (***c***), and 2.8 Hz (***d***)

Рис. 4. Строение и элементный анализ участков сосредоточения эвтектики после ионного «травления» в сплавах, наплавленных без колебаний электрода (***а***) и с перемещениями дуги по поверхности сварочной ванны (***b–d***) с частотой *f* = 1,3 Гц (***б***), 2 Гц (***c***), 2,8 Гц (***d***)

Further increase of the arc oscillation frequency to *f* = 2.8 Hz results in the smoothing of the temperature peaks caused by reheating in the cooling curves (as observed in Fig. 2, *d*) and shortens the time intervals between these peak temperatures. This phenomenon suggests a more uniform temperature gradient across the width of the weld pool. Simultaneously, the weld pool length decreases, while its volume increases due to the rapid transverse oscillations of the arc at approximately ~44 mm/s. Consequently, the weld bead becomes even wider ($\mu_b = 0.82$) (Fig. 2, *d*), in comparison to beads produced at at lower *f*.

At an oscillation frequency of *f* = 2.8 Hz, the conditions governing heat input to the crystallization front change, resulting in an extended period during which the crystallizing metal is at the nickel aluminide melting point (Fig. 3, *d*). In such conditions, the formation of the structure initiates with the emergence of alloyed γ-solid solution dendrites and concludes with the appearance of nickel-aluminum martensite ($L1_0$ lattice) in the phase diagram region situated between the γ′-phase and the β-(NiAl)-phase. The primary reason for this martensite formation is the relatively slow cooling rate of the nickel-aluminum alloy from temperatures below 1200 °C, in contrast to the cooling rate typical of lower frequencies in non-oscillatory surfacing. A similar hypothesis was put forth by Kositsyn S. et al. [25]. Prolonged exposure of the metal to elevated temperatures results in annealing. Prior to the formation of cooling martensite, the alloy’s composition undergoes modification: it becomes enriched with aluminum atoms, which, as indicated by Kablov D. et al. [26], exhibit the highest diffusion coefficient in nickel (in the context of the alloying system under consideration) at temperatures exceeding 900 °C. This shift in composition moves the alloy towards the region where the β-phase is stable. Examination of the martensitic region following surface ion etching reveals the presence of relatively thin plates (measuring 300–600 nm) with twinning orientation relative to each other (as depicted in Fig. 4, *d*). The atomic mass ratio of nickel to aluminum corresponds to that of the Ni_2Al phase.

The alteration in the metal's structure due to transverse weld arc oscillations has an impact on its hardness, which varies within the range of 27 to 35 HRC depending on the oscillation frequency. It's worth noting that after ~50 thermal cycles (Fig. 5), the hardness of the alloy deposited at $f = 2.8$ Hz no longer depends on subsequent thermal cycles. It remains constant, which can be attributed to the overall high thermal stability of the alloy structure.

The alloy surfaced at $f = 2.8$ Hz exhibits the highest hardness value (~35 HRC), whereas the lowest hardness (27 HRC) is observed in the surfacing conducted without transverse arc oscillations (see Fig. 5). Under identical test conditions, the hardness of the commercially available Ni alloy Hastelloy C steadily decreases due to its progressive softening and loss of thermal stability.

The cobalt-based alloy Stoodite 6, characterized by a slightly higher initial hardness of 42 HRC, demonstrates robust resistance to softening. It retains its hardness almost consistently for up to 100 thermal cycles. With a further increase in the number of thermal cycles, the hardness gradually decreases and approaches the level of approximately 35 HRC, which is similar to the hardness of the alloy manufactured at $f = 2.8$ Hz.

The results of thermal fatigue tests indicate that the alloy produced at 2.8 Hz exhibits the highest durability, enduring for up to 200 cycles (Fig. 5). This durability can be attributed to the attainment of an optimal ratio between the γ-solid solution and nickel-aluminum cooling martensite within the structure of a relatively ductile metal. This metal is highly alloyed, containing up to 18 wt. % of iron and other elements. Au Y. et al. [27] reported that such an alloy is susceptible to thermoelastic transformations. During the tests, reheating of the martensite restored the reversibility of the martensite transformation. However, subsequent multiple thermal cycles lead to the dispersive decomposition of the metastable Ni_2Al-phase into Ni_5Al_3-phase particles and a decrease in the critical temperatures of the martensitic transformation. The tungsten and tantalum contents in the examined alloy do not significantly differ, whereas chromium and molybdenum are primarily dissolved in the γ-solid solution.

The assessment of oxidative wear resulting from thermal fatigue tests indicates that the studied alloy, manufactured at $f = 2.8$ Hz, exhibits superior properties compared to other available heat-resistant materials after 125 thermal cycles (Fig. 6). This difference is particularly pronounced when compared to Hastelloy C, which displays lower oxidation resistance. The diminished oxidation resistance of Hastelloy C can be attributed to the increased diffusion of oxygen from the oxidizing atmosphere through the Cr_2O_3 oxide layer. In contrast, the elevated chromium content in the alloy forms a barrier that initially hinders oxygen diffusion during the test. This barrier thickens over the course of 100–110 thermal cycles (Fig. 6). Subsequently, the protective layer experiences partial degradation.

The mass loss due to oxidation (Δm) consistently decreases in the alloy surfaced without arc oscillations. However, in the case of the alloy surfaced with arc oscillations, the mass loss remains relatively stable after 120 thermal cycles. This stability is attributed to the formation of an oxide layer on the substrate, cons-

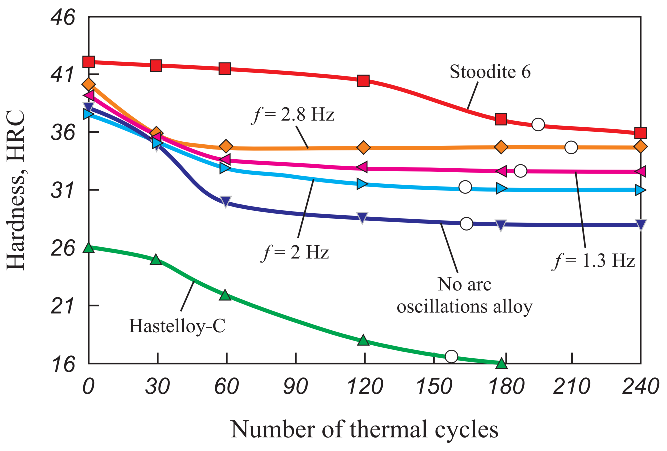

Fig. 5. Alloy hardness vs. number of thermal cycles
○ – indicates the formation of the first thermal fatigue cracks

Рис. 5. Зависимость твердости исследуемых сплавов от количества теплосмен
○ – обозначение момента, соответствующего образованию первых трещин термической усталости

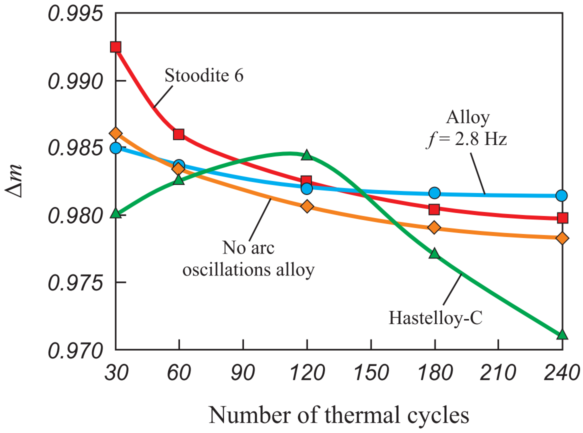

Fig. 6. Weld metal oxidation resistance vs. the number of thermal cycles

Рис. 6. Зависимость стойкости наплавленного металла к окислительному износу от количества теплосмен

tituting not less than 70 vol. % Al_2O_3, along with traces of Cr_2O_3 and 5 vol. % NiO. The cobalt alloy Stoodite 6 demonstrates reasonably high oxidation resistance due to the formation of the $CoCr_2O_4$ oxide. It only becomes less effective than the studied alloy after 125 thermal cycles when oxidation microcracks intensively develop in the regions susceptible to oxidation of Cr_7C_3 [28]. Within the margin of measurement error, it can be inferred that the oxidation resistance of the studied alloy is comparable to that of Stoodite 6.

The surfacing process involving weld arc oscillation effectively regulates the heat input to the crystallization front, thereby establishing favorable conditions for the development of coatings with exceptional resistance to thermal fatigue cracks.

Conclusion

1. Transverse arc oscillations applied to the weld pool surface change the configuration of the crystallization front and the thermal conditions governing the formation of the alloyed nickel aluminide structure. At a low electrode oscillation frequency (f = 1.3 Hz), a structure is generated in which the clusters of γ'-Ni_3Al-phase lamellar and sharp-angular particles transform into layered regions. This transformation enhances the resistance to thermal fatigue cracking compared to the alloy surfaced without electrode oscillations.

2. In order to achieve the utmost resistance to thermal fatigue cracking, the thermal conditions (at 2.8 Hz) should promote gradual cooling of the nickel-aluminum alloy and the developement of a balanced structure comprising the γ'-solid solution, heavily alloyed (up to 18 wt. %) with iron and other elements, as well as nickel-aluminum martensite. The composition of this martensite corresponds to the metastable Ni_2Al phase, and reheating it does not render the alloy more brittle.

3. The weld pool temperature gradient stabilizes at f = 2.8 Hz, concurrently leading to a reduction in the length of the weld pool and the attainment of the highest weld bead shape factor ($\mu_b = 0.83$). Consequently, the extent of bead-to-bead overlap can be decreased to 20–30 %, thereby reducing the consumption of relatively expensive surfacing material.

References / Список литературы

1. Sokolov G.N., Lysak V.I. Surfacing of wear-resistant alloys on press dies and tools for hot deformation of steels. Volgograd, Politekhnik, 2005. 284 p. (In Russ.).

   Соколов Г.Н., Лысак В.И. Наплавка износостойких сплавов на прессовые штампы и инструмент для горячего деформирования сталей. Волгоград: Политехник, 2005. 284 с.
2. Mendez P.F., Barnes N., Bell K., Borle S.D., Gajapathi S.S., Guest S.D., Izadi H., Gol A.K., Wood G. Welding processes for wear resistant overlays. *Journal of Manufacturing Processes*. 2014;16(1):4–25. https://doi.org/10.1016/j.jmapro.2013.06.011
3. Rosert R. Cobalt-based alloys for surfacing. *The Paton Welding Journal*. 2015;(5–6):101–106. https://doi.org/10.15407/tpwj2015.06.23

   Росерт Р. Сплавы на кобальтовой основе для наплавки. *Автоматическая сварка*. 2015;(5–6):108–113.
4. Kolobov Yu.R., Kablov E.N., Kozlov E.V., Koneva N.A., Povarova K.B., Grabovetskaya G.P., Buntushkin V.P., Bazyleva O.A., Muboyadzhyan S.A., Budinovskii S.A. Structure and properties of intermetallic materials with nanophase hardening. Moscow: MISIS, 2008. 328 p. (In Russ.).

   Колобов Ю.Р., Каблов Е.Н., Козлов Э.В., Конева Н.А., Поварова К.Б., Грабовецкая Г.П., Бунтушкин В.П., Базылева О.А., Мубояджян С.А., Будиновский С.А. Структура и свойства интерметаллидных материалов с нанофазным упрочнением. М.: МИСиС, 2008. 328 с.
5. Bondarenko Yu.A., Kuzmina N.A., Bazyleva O.A., Raevskikh A.N. On structure and phase composi-

tion of NiAl–Ni_3Al-based intermetallic alloys obtained by high-gradient directional crystallization. *Voprosy Materialovedeniya*. 2018; 2(94):52–60. (In Russ.).
https://doi.org/10.22349/1994-6716-2018-94-2-52-60

Бондаренко Ю.А., Кузьмина Н.А., Базылева О.А., Раевских А.Н. Исследование структуры и фазового состава интерметаллидного сплава системы NiAl–Ni_3Al, полученного методом высокоградиентной направленной кристаллизации. *Вопросы материаловедения*. 2018;2(94):52–60.
https://doi.org/10.22349/1994-6716-2018-94-2-52-60

6. Tsao Te-Kang, Yeh An-Chou. The thermal stability and strength of highly alloyed Ni_3Al. *Materials Transactions*. 2015;56(11):1905–1910.
https://doi.org/10.2320/matertrans.M2015298

7. Lei Wang, Chengli Yao, Jun Shen, Yunpeng Zhang, Tao Wang, Hengxin Xu, Luhan Gao, Guojun Zhang. Microstructures and compressive properties of NiAl–Cr(Mo) and NiAl–Cr eutectic alloys with different Fe contents. *Materials Science and Engineering: A*. 2019;744:593–603.
https://doi.org/10.1016/j.msea.2018.12.085

8. Povarova K.B., Bazyleva O.A., Drozdov A.A., Alad'ev N.A., Samsonova M.A. Low-cycle fatigue of an Ni_3Al-based VKNA-25 alloy at room temperature. *Russian Metallurgy (Metally)*. 2012;2012:975–984.
https://doi.org/10.1134/S0036029512110134

Поварова К.Б., Базылева О.А., Дроздов А.А., Аладьев Н.А., Самсонова М.А. Исследование малоцикловой усталости при комнатной температуре сплава на основе интерметаллида Ni_3Al типа ВКНА-25. *Металлы*. 2012;(6):70–82.

9. Shang-ping Li, Di Feng, He-li Luo, Xi-e Zhang, Xu Cao. Development of new wear-resistant surface coating at elevated temperature. *Journal of Iron and Steel Research*. 2006;13:37–40.
https://doi.org/10.1016/S1006-706X(06)60092-7

10. Lukin V.I., Bazyleva O.A., Kovalchuk V., Golev E.V., Khodakova E.A. Investigation of the properties of castings of VKNA-1VR intermetallic alloy after repairing defects by welding. *Welding International*. 2015;29(10):795–800.
https://doi.org/10.1080/09507116.2014.986883

Лукин В.И., Базылева О.А., Ковальчук В.Г., Голев Е.В., Ходакова Е.А. Исследование свойств отливок из интерметаллидного сплава ВКНА-1ВР после исправления дефектов методом сварки. *Сварочное производство*. 2014;(10):5–12.

11. Meng Zhang, Ying Wang, Zhenwen Yang, Zongqing Ma, Zhijiang Wang, Dongpo Wang. Microstructure and mechanical properties of twin wire and arc additive manufactured Ni_3Al-based alloy. *Journal of Materials Processing Technology*. 2022;303:117529.
https://doi.org/10.1016/j.jmatprotec.2022.117529

12. Sorokin L.I. Stresses and cracks in welding and heat treatment of creep-resisting nickel alloys. *Welding International*. 2000;14(6):478–484.
https://doi.org/10.1080/09507110009549215

Сорокин Л.И. Напряжения и трещины при сварке и термической обработке жаропрочных никелевых сплавов. *Сварочное производство*. 1999;(12):11–17.

13. Saraev Yu.N., Poletika I.M., Kozlov A.V., Khomchenko E.G. Formation of the structure and properties of welded joints under conditions of controlled heat input in pulsed arc welding. *Fizicheskaya mezomekhanika*. 2005;8(S):137–140. (In Russ.).

Сараев Ю.Н., Полетика И.М., Козлов А.В., Хомченко Е.Г. Формирование структуры и свойств сварных соединений в условиях регулируемого тепловложения при импульсно-дуговой сварке. *Физическая мезомеханика*. 2005;8(S):137–140.

14. Dushina A.Yu., Olshanskaya T.V., Neulybin S.D., Shchitsyn Yu.D., Nikulin R.G. Influence of the current frequency in the process of pulsed layer-by-layer plasma surfacing on the structure and properties of high-alloy steel during additive forming of products. *Vestnik Permskogo natsional'nogo issledovatel'skogo politekhnicheskogo universiteta. Mashinostroenie, materialovedenie*. 2021;23(2):20–26. (In Russ.).
https://doi.org/10.15593/2224-9877/2021.2.03

Душина А.Ю., Ольшанская Т.В., Неулыбин С.Д., Щицын Ю.Д., Никулин Р.Г. Влияние частоты тока в процессе импульсной послойной плазменной наплавки на структуру и свойства высоколегированной стали при аддитивном формировании изделий. *Вестник Пермского национального исследовательского политехнического университета. Машиностроение, материаловедение*. 2021;23(2):20–26.
https://doi.org/10.15593/2224-9877/2021.2.03

15. Lebedev V.A., Dragan S.V., Simutenkov I.V. Influence of high-frequency oscillations of the electrode wire during automatic submerged arc surfacing on the properties of the deposited layer. *Uprochnyayushchie tekhnologii i pokrytiya*. 2016;(5):17–21. (In Russ.).

Лебедев В.А., Драган С.В., Симутенков И.В. Влияние высокочастотных колебаний электродной проволоки при автоматической наплавке под флюсом на свойства наплавленного слоя. *Упрочняющие технологии и покрытия*. 2016;(5):17–21.

16. Gualco A., Svoboda H.G., Surian E.S. Effect of heat input on the Fe-based nanostructured weld overlay. *Soldagem & Inspecao*. 2013;18(4):329–338.
https://doi.org/10.1590/S0104-92242013000400005

17. Degterev A.S., Sovetchenko B.F., Trushchenko E.A., Gnyusov S.V. Influence of technological parameters of plasma powder surfacing on the formed structure of coatings of the Fe–Cr–V–Mo–C system. *Svarka i diagnostika*. 2011;(4):14–20. (In Russ.).

Дегтерев А.С., Советченко Б.Ф., Трущенко Е.А., Гнюсов С.В. Влияние технологических параметров плазменной порошковой наплавки на формируемую структуру покрытий системы Fe–Cr–V–Mo–C. *Сварка и диагностика*. 2011;(4):14–20.

18. Luchtenberg P., Campos P.T., Soares P., Laurindo C.A., Maranho O., Torres R.D. Effect of welding energy on the corrosion and tribological properties of duplex stainless steel weld overlay deposited by GMAW/CMT process. *Surface and Coatings Technology*. 2019;375:688–693.
https://doi.org/10.1016/j.surfcoat.2019.07.072

19. Wu Dongting, An Qi, Matsuda Kenji, Zhang Yongang, Yu Baojun, Zou Yong Characteristics of bypass coupling twin-wire indirect arc welding with high-speed welding. *Journal of Materials Processing Technology*. 2021;291:116995.
https://doi.org/10.1016/j.jmatprotec.2020.116995

20. Leitnera M., Pichlera P., Steinwendera F., Gusterb C. Wear and fatigue resistance of mild steel components reinforced by arc welded hard layers. *Surface & Coatings Technology*. 2017;330:140–148.
http://dx.doi.org/10.1016/j.surfcoat.2017.09.046

21. Gnyusov S.F., Degterev A.S., Tarasov S. Yu. The effect of plasma torch weaving on microstructural evolution in multiplepass plasma-transferred arc Fe–Cr–V–Mo–C coating. *Surface & Coatings Technology*. 2018;344:75–84.
https://doi.org/10.1016/j.surfcoat.2018.03.002

22. Chieh Fan, Ming-Che Chen, Chia-Ming Chang, Weite Wu. Microstructure change caused by $(Cr,Fe)_{23}C_6$ carbides in high chromium Fe–Cr–C hardfacing alloys. *Surface & Coatings Technology*. 2006;201(3-4):908–912.
https://doi.org/10.1016/j.surfcoat.2006.01.010

23. Lai Hsuan-Han, Hsieh Chih-Chun, Lin Chi-Ming, Wu Weite. Effect of oscillating traverse welding on microstructure evolution and characteristic of hypoeutectic hardfacing alloy. *Surface & Coatings Technology*. 2014;239:233–239.
http://dx.doi.org/10.1016/j.surfcoat.2013.11.048

24. Zorin I.V., Sokolov G.N., Dubczov Yu.N., Lysak V.I., Bobkov An.S. Surfacing of pipe-piercing mandrels with Ni_3Al-based alloy using composite wire. 2016;(2):20–23. *Svarka i diagnostika*. (In Russ.).

Зорин И.В., Соколов Г.Н., Дубцов Ю.Н., Лысак В.И., Бобков А.С. Наплавка трубопрошивных оправок сплавом на основе Ni_3Al с использованием композиционной проволоки. *Сварка и диагностика*. 2016;(2):20–23.

25. Kositsyn S.V., Valiullin A.I., Kataeva N.V. Kositsyna I.I. Investigation of microcrystalline NiAl-based alloys with high-temperature thermoelastic martensitic transformation: I. Resistometry of the Ni–Al and Ni–Al–X (X = Co, Si, or Cr) alloys. *The Physics of Metals and Metallography*. 2006;102(4):391–405.
https://doi.org/10.1134/S0031918X06100073

Косицын С.В., Валиуллин А.И., Катаева Н.В., Косицына И.И. Исследование микрокристаллических сплавов на основе моноалюминида никеля с высокотемпературным термоупругим мартенситным превращением. I. Резистометрия сплавов Ni–Al и Ni–Al–X (X = Co, Si, Cr). *Физика металлов и металловедение*. 2006;102(4):418–432.

26. Kablov D.E., Sidorov V.V., Puchkov Y.A. Diffusion behavior features of impurities and microalloying additives in nickel and single crystal superalloys. *Aviation Materials and Technologies*. 2016;1(40):24–31. (In Russ.).
https://doi.org/10.18577/2071-9140-2016-0-1-24-31

Каблов Д.Е., Сидоров В.В., Пучков Ю.А. Особенности диффузионного поведения примесей и рафинирующих добавок в никеле и монокристаллических жаропрочных сплавах. *Авиационные материалы и технологии*. 2016;1(40):24–31.
https://doi.org/10.18577/2071-9140-2016-0-1-24-31

27. Au Y.K., Wayman C.M. Thermoelastic behavior of the martensitic transformation in ß′ NiAl alloys. *Scripta Metallurgica*. 1972;6(12):1209–1214.
https://doi.org/10.1016/0036-9748(72)90233-5

28. Cao R., Zhang H.Y., Liu G.H., Che H.Y., Chen J.H. Effect of thermal cycle shocking on microstructure and mechanical properties of Stellite 12 (Co–29Cr–2.3C–3W) cobalt based alloy. *Materials Science & Engineering A*. 2018;714:68–74.
https://doi.org/10.1016/j.msea.2017.12.057

Information about the Authors

Ilya V. Zorin – Dr. Sci. (Eng.), Prof., Department of Welding Equipment and Technology, Volgograd State Technical University (VolgSTU)
ORCID: 0000-0002-9912-2598
E-mail: zorin.iv@vstu.ru; kewa991@yandex.ru

Vladimir I. Lysak – Dr. Sci. (Eng.), Prof., Acad. of the Russian Academy of Sciences, Head of the Department of Welding Equipment and Technology, Scientific Adviser of the VolgSTU
ORCID: 0000-0003-3066-058X
E-mail: lysak@vstu.ru

Valentin O. Kharlamov – Cand. Sci. (Eng.), Assoc. Prof., Department of Welding Equipment and Technology, VolgSTU
ORCID: 0000-0002-5039-4592
E-mail: harlamov_vo@mail.ru

Sergey A. Fastov – Postgraduate Student of the Department of Welding Equipment and Technology, VolgSTU
ORCID: 0000-0002-3371-0434
E-mail: serheyfastov@yandex.ru

Сведения об авторах

Илья Васильевич Зорин – д.т.н., профессор кафедры «Оборудование и технология сварочного производства» Волгоградского государственного технического университета (ВолгГТУ)
ORCID: 0000-0002-9912-2598
E-mail: zorin.iv@vstu.ru; kewa991@yandex.ru

Владимир Ильич Лысак – д.т.н., профессор, академик РАН, заведующий кафедрой «Оборудование и технология сварочного производства», научный руководитель ВолгГТУ
ORCID: 0000-0003-3066-058X
E-mail: lysak@vstu.ru

Валентин Олегович Харламов – к.т.н., доцент кафедры «Оборудование и технология сварочного производства», ВолгГТУ
ORCID: 0000-0002-5039-4592
E-mail: harlamov_vo@mail.ru

Сергей Анатольевич Фастов – аспирант кафедры «Оборудование и технология сварочного производства», ВолгГТУ
ORCID: 0000-0002-3371-0434
E-mail: serheyfastov@yandex.ru

Contribution of the Authors

I. V. Zorin – problem statement, experimental tests, authorship of the article.
V. I. Lysak – text editing, discussions.

V. O. Kharlamov – electronic microscope studies, discussions.

S. A. Fastov – manufacturing of the composite wire, conducting surfacing experiments.

Вклад авторов

И. В. Зорин – определение цели работы, проведение экспериментов, написание статьи.
В. И. Лысак – научное редактирование, участие в обсуждении результатов.
В. О. Харламов – проведение электронно-микроскопических исследований, участие в обсуждении результатов.
С. А. Фастов – участие в изготовлении композиционной проволоки для наплавки и в экспериментах по ее наплавке.

Received 17.05.2023
Revised 14.07.2023
Accepted 18.07.2023

Статья поступила 17.05.2023 г.
Доработана 14.07.2023 г.
Принята к публикации 18.07.2023 г.

Зарегистрирован Федеральной службой по надзору
в сфере связи, информационных технологий
и массовых коммуникаций.
Свидетельство о регистрации **ПИ № ФС77-79230**

Журнал распространяется агентством «Урал-Пресс»
Подписной индекс: 80752 (печатная версия)
05108 (электронная версия)